THESIS FOR THE DEGREE OF DOCTOR OF PHILOSOPHY

There Is an Alloy at the End of the Rainbow: Structure and Optical Properties From Bulk to Nano

J. Magnus Rahm

Department of Physics
CHALMERS UNIVERSITY OF TECHNOLOGY
Göteborg, Sweden 2021

There Is an Alloy at the End of the Rainbow:
Structure and Optical Properties From Bulk to Nano
J. Magnus Rahm

ISBN 978-91-7905-485-4
Doktorsavhandlingar vid Chalmers tekniska högskola. Ny serie nr 4952
ISSN 0346-718X

Department of Physics
Chalmers University of Technology
SE-412 96 Göteborg, Sweden
Telephone +46 (0)31 772 10 00

Cover: The WULFFPACK wolf collects a truncated octahedral nanoparticle on its way to the Pd–Au alloy guarded by the ICET magpie.

Chalmers digitaltryck
Göteborg, Sweden 2021

There Is an Alloy at the End of the Rainbow: Structure and Optical Properties From Bulk to Nano

J. Magnus Rahm
Department of Physics
Chalmers University of Technology

Abstract

Mixing different chemical species and decreasing dimensions to the nanoscale are two powerful approaches for improving materials. In both cases new properties emerge, and structure, composition, and chemical ordering can be tuned to tailor materials for specific purposes. To exploit the potential of these materials, it is crucial that they are fundamentally understood, and to this end, computational methods have emerged as an important complement to experiment. This thesis presents the development and application of methods for modeling alloys, nanoparticles, and nanoalloys on the atomic scale, with the purpose of guiding the search for new materials, in particular those related to plasmonic sensing of hydrogen.

A software for creating and sampling alloy cluster expansion has been developed partially in connection to this thesis, and is applied to hydrogenation of Pd and Pd–Au. For Pd–Au, the impact of chemical order on hydrogen uptake is studied, and two kinds of phase diagrams are calculated; one in which the Pd/Au atoms are fixed, and one in which they rearrange in response to hydrogen. These phase diagrams are constructed under the assumption that phase separation occurs with incoherent interfaces. This is not always the case, in particular not during hydrogenation of small Pd nanoparticles. Coherent interfaces lead to strain, and a methodology for studying this significantly more complex case is developed and applied to Pd–H, showing that there are three temperature intervals with qualitatively distinct hydrogenation behaviors.

Moreover, a software for creating Wulff constructions for the prediction of equilibrium nanoparticle shapes has been developed as part of this thesis and is used to study the impact of halides on the shapes of Au and Pd nanoparticles. Furthermore, an algorithm for finding equilibrium shapes of nanoparticles on the atomic scale is detailed, and the results indicate that an ensemble of nanoparticles in thermodynamic equilibrium in general should be expected to contain multiple different shapes. Moreover, nanoalloys of Ag–Cu and Pd–Au are studied on the atomic scale with the aim to understand how chemical ordering is impacted on the nanoscale, which reveals an interplay between chemistry and strain that can give rise to a rather complex distribution of the components throughout a nanoalloy. Finally, the dielectric functions of ten metallic alloys are calculated with first-principles methods and benchmarked with experiment, providing a library of reference data to aid modeling of nanoplasmonic systems. The latter results have also been made available in the form of a web application.

Keywords: alloys, nanoalloys, thermodynamics, hydrides, alloy cluster expansions, optical properties, dielectric functions

LIST OF APPENDED PAPERS

This thesis is partly based on the author's licentiate thesis (J. M. Rahm, *Structure and chemical ordering in metallic nanoparticles from atomic scale modeling* (2019)). It consists of seven introductory chapters and the following papers:

I **ICET – A Python library for constructing and sampling alloy cluster expansions**
Mattias Ångqvist, William A. Muñoz, J. Magnus Rahm, Erik Fransson, Céline Durniak, Piotr Rozyczko, Thomas Holm Rod, and Paul Erhart
Advanced Theory and Simulations **2**, 1900015 (2019)

II **A tale of two phase diagrams: Interplay of ordering and hydrogen uptake in Pd–Au–H**
J. Magnus Rahm, Joakim Löfgren, Erik Fransson, and Paul Erhart
Acta Materialia **211**, 116893 (2021)

III **Quantitative predictions of thermodynamic hysteresis: Temperature-dependent character of the phase transition in Pd–H**
J. Magnus Rahm, Joakim Löfgren, and Paul Erhart
In manuscript

IV **WulffPack: A Python package for Wulff constructions**
J. Magnus Rahm and Paul Erhart
Journal of Open Source Software **5**, 1944 (2020)

V **Beyond magic numbers: Atomic scale equilibrium nanoparticle shapes for any size**
J. Magnus Rahm and Paul Erhart
Nano Letters **17**, 5775–5781 (2017)

VI **Understanding chemical ordering in bimetallic nanoparticles from atomic-scale simulations: The competition between bulk, surface, and strain**
J. Magnus Rahm and Paul Erhart
The Journal of Physical Chemistry C **122**, 28439 (2018)

VII **Computational assessment of the efficacy of halides as shape-directing agents in nanoparticle growth**
Joakim Löfgren, J. Magnus Rahm, Joakim Brorsson, and Paul Erhart
Physical Review Materials **4**, 096001 (2020)

VIII **A library of late transition metal alloy dielectric functions for nanophotonic applications**
J. Magnus Rahm, Christopher Tiburski, Tuomas P. Rossi, Ferry Anggoro Ardy Nugroho, Sara Nilsson, Christoph Langhammer, and Paul Erhart
Advanced Functional Materials **30**, 2002122 (2020)

The author's contribution to the papers:

I I participated in the development of the software, ran the Ag–Pd simulations, analyzed the corresponding results, and wrote parts of the paper together with my co-authors.

II I ran parts of the density-functional theory calculations, fitted the cluster expansions, ran the Monte Carlo simulations, analyzed all results, and wrote the paper with assistance from my co-authors.

III I ran parts of the density-functional theory calculations, implemented the constituent strain formalism, fitted the cluster expansion, ran the Monte Carlo simulations, developed the analysis approach, analyzed all results, and wrote the paper with assistance from my co-authors.

IV I developed the software and wrote the paper with assistance from my co-author.

V I refined the algorithm, carried out the simulations, analyzed the results, and wrote the paper with assistance from my co-author.

VI I carried out the majority of the simulations, analyzed the results, and wrote the paper with assistance from my co-author.

VII I developed the software for Wulff constructions and assisted in the writing of the paper.

VIII I generated the special quasirandom structures, ran the time-dependent density-functional theory calculations, analyzed the results, developed the associated web application, and wrote the first draft of the paper.

PUBLICATIONS NOT INCLUDED IN THIS THESIS

The following publications are outside the scope of this thesis:

Structurally driven asymmetric miscibility in the phase diagram of W–Ti
Mattias Ångqvist, J. Magnus Rahm, Leili Gharaee, and Paul Erhart
Physical Review Materials **3**, 073605 (2019)

Non-Bonded Radii of the Atoms Under Compression
Martin Rahm, Mattias Ångqvist, J. Magnus Rahm, Paul Erhart, and Roberto Cammi
ChemPhysChem **21**, 2441 (2020)

Contents

List of abbreviations

ARDR automatic relevance determination regression. 51

BCC body-centered cubic. 27

DFT density-functional theory. 25, 43–46, 48–52, 65

EAM embedded atom method. 46, 47, 54, 68, 69, 74

ECI effective cluster interaction. 48–51, 53, 73

FCC face-centered cubic. 25–27, 53, 64

LSPR localized surface plasmon resonance. 36, 37, 40, 41

MC Monte Carlo. 48, 54–61, 63–65, 67, 69

MD molecular dynamics. 54–56, 59–61, 69

OLS ordinary least squares. 50, 51

RTO regular truncated octahedron. 25, 27

SGC semi-grand canonical. 56, 57, 67

SQS special quasirandom structure. 54, 63, 73

TDDFT time-dependent density-functional theory. 44, 45, 54, 72, 73

VCSGC variance-constrained semi-grand canonical. 57, 58, 65, 67

1

Introduction

Adamantium, vibranium, unobtainium, and cryptonite—not only scientists recognize the importance of new materials for technological advancement. Unlike Black Panther and Superman, chemists and materials scientists are restricted to the periodic table when making new materials. But even these hundred or so chemical elements provide a toolbox that is almost unfathomable. The diversity derives primarily from two degrees of freedom: the combination of elements and the spatial arrangement of the atoms. The combination of two or more metals is an alloy, and an alloy often has the favorable properties of its components and sometimes qualities that are entirely unforeseen. Likewise, by making nanoparticles and other objects on the nanoscale, materials behave in ways unheard of on the macroscale. Solutions to many of the challenges related to the energy crisis are undoubtedly hidden in this realm of yet-to-be-realized materials [1, 2]. The pot of gold at the end of the rainbow is full of alloys too.

The first element of the periodic table, hydrogen, is expected to play an important role in the replacement of fossil fuels [3]. The H_2 molecule is an excellent energy carrier, which when consumed leaves only water behind. The Swedish (or German) word for a mixture of hydrogen and oxygen gas, *knallgas* ("bang gas"), indicates, however, that hydrogen is not necessarily the most easily maintainable source of energy. The dramatic footage of the tragic Hindenburg accident, in which an airship filled with hydrogen exploded, is imprinted in collective memory and reminds us that mishandling of hydrogen can have fatal consequences. Strategies for detecting hydrogen leakages are essential [4].

This thesis has emerged in relation to the development of palladium-based nanoalloys for hydrogen sensing. The idea is the following: palladium nanoparticles, possibly alloyed with gold and/or copper [5–7], easily absorb hydrogen upon exposure to hydrogen gas, and when doing so, their optical properties change [8, 9]. By placing the nanoparticles just outside the equipment where the hydrogen ought to be confined and by con-

tinuously tracking the optical response of the nanoparticles, a hydrogen leakage can be detected [10, 11]. These hydrogen detectors would not fit in Marvel comics. Their success is instead based on both a rational combination of chemical elements (for obtaining a favorable hydrogen uptake) and a tuning of the structure at the nanoscale (for obtaining a detectable optical response and faster kinetics [12, 13]). It is, however, in many respects a complex material and many questions are yet to be answered. How are the palladium and gold atoms arranged relative to each other in the material and how does this affect the sensing properties? What happens on the atomic scale when the nanoparticles are loaded with hydrogen? What is the optimal shape of the nanoparticles? How can we understand the change in optical properties at the electronic level? This thesis attempts to provide answers to some of these questions and to serve as a springboard for further investigation of others.

The work in this thesis can be loosely divided into three categories: the thermodynamics of palladium-based hydrides (Papers I–III), the atomic structure and shapes of nanoparticles (Papers IV–VII), and the optical properties of alloys (Paper VIII). While palladium-based, optical hydrogen sensing is the application in mind for much of this content, the thesis is also part of the general effort to further our knowledge of materials through computer simulations. The tremendous improvements of computational power as well as computational techniques and algorithms over the last decades has made computation an important complement to experiment. Yet, the development of user-friendly software that incorporates these algorithms while lending flexibility for the users remains a challenge in many parts of physics and materials science [14]. This thesis has contributed to two open-source software packages: ICET (for modeling of alloys with alloy cluster expansions) and WULFFPACK (for constructing equilibrium nanoparticle shapes via Wulff constructions). These software have been important tools in much of the work presented here, and will hopefully be useful for many scientific studies to come.

This thesis is structured as follows. Chapter 2 discusses the thermodynamics of alloys and hydrides with focus on phase diagrams in bulk. The nanoscale is introduced in Chapter 3, with an emphasis on the atomic structure of metallic nanoparticles. The optical properties of metals in general and metallic nanoparticles in particular are discussed in Chapter 4. An overview of the computational methods used within the scope of this thesis is given in Chapter 5, highlighting the most central aspects. The appended papers are summarized in Chapter 6. Finally, possible future extensions of the present work are discussed in Chapter 7.

2

Thermodynamics of alloys and hydrides

The properties of alloys, or any material consisting of more than one chemical element, depend on the way in which the atoms are organized. This chemical ordering of the atoms is to a large extent governed by the laws of thermodynamics. Materials are often found in their thermodynamic equilibrium state, and even when they are not, thermodynamics provides the driving force that governs how the material will evolve over time. This chapter gives an introduction to the thermodynamics of alloys and metallic hydrides, which are both highly relevant for nanoplasmonic hydrogen sensors.

2.1 Phase diagrams

Information about equilibrium states under various conditions can be visualized in a phase diagram. While this section focuses on the special case of a binary alloy considering equilibria as a function of composition and temperature, the principles are general and are readily extended to more than two components. A particular pressure, typically 1 atm for solid systems, is implicit but it is in principle possible to extend the diagram with a pressure axis.

Under these circumstances, the equilibrium state of a system is characterized by a minimum in the Gibbs free energy G. The phase diagram can be constructed if the free energy as a function of composition and temperature is known. The situation becomes interesting when the free energy curve contains one or more concave regions. The system can then phase separate in two or more phases, the sum of which has a lower free energy than the non-phase separated (single-phase) system.

Consider an alloy with a free energy curve $G(c)$ such as the red one in Fig. 2.1a. If the system is homogeneous (the concentration is the same in all parts of the sample) with concentration c_{av}, it has a free energy $G(c_{\text{av}})$. We can compare this free energy to the free energy of a system with the same average concentration c_{av} but where the concentration is not homogeneous. Specifically, if the system has phase separated in two phases 1 and 2 with concentrations c_1 and c_2 in proportions α_1 and α_2, the new free energy is

$$G_{1+2}(c_{\text{av}}) = \alpha_1 G(c_1) + \alpha_2 G(c_2) \tag{2.1}$$

but the mass of either element needs to be conserved, so we require

$$\alpha_1 c_1 + \alpha_2 c_2 = c_{\text{av}} \quad \text{and} \quad \alpha_1 + \alpha_2 = 1. \tag{2.2}$$

Combining the equations we find

$$\alpha_1 = \frac{c_2 - c_{\text{av}}}{c_2 - c_1} \quad \text{and} \quad \alpha_2 = \frac{c_{\text{av}} - c_1}{c_2 - c_1} \tag{2.3}$$

and the new free energy is

$$G_{1+2}(c_{\text{av}}) = \frac{c_2 - c_{\text{av}}}{c_2 - c_1} G(c_1) + \frac{c_{\text{av}} - c_1}{c_2 - c_1} G(c_2). \tag{2.4}$$

The question is then whether such a phase separation lowers the free energy (compared to the single-phase free energy $G(c_{\text{av}})$) and if so, which values of c_1 and c_2 minimize $G_{1+2}(c_{\text{av}})$. It is a simple matter of differentiation and algebra to show that an extremum in $G_{1+2}(c_{\text{av}})$ is reached for c_1 and c_2 chosen such that

$$\left.\frac{\partial G}{\partial c}\right|_{c=c_1} = \left.\frac{\partial G}{\partial c}\right|_{c=c_2} = \frac{G(c_2) - G(c_1)}{c_2 - c_1}, \tag{2.5}$$

which implies that the tangents at $G(c_1)$ and $G(c_2)$ coincide (dashed lines in Fig. 2.1a). This extremum is a minimum only if this tangent lies below $G(c)$. The family of such tangents that lie below $G(c)$ is referred to as the convex hull. The system phase separates into multiple phases only in regions where the convex hull deviates from $G(c)$. Such regions are referred to as multi-phase regions (two-phase regions in binary alloys) and an alloy phase diagram is a map where the boundaries for these regions are drawn as a function of temperature or other thermodynamic variables (Fig. 2.1b). Due to the lowering of the free energy by phase separation, some elements do not dissolve in each other, and in such materials the two-phase region is often referred to as a miscibility gap.

2.1.1 Mean-field treatment of the Ising model

The previous section discussed two-phase regions for a material with a given free energy $G(c)$ but nothing was said about how this function emerges physically. The free energy

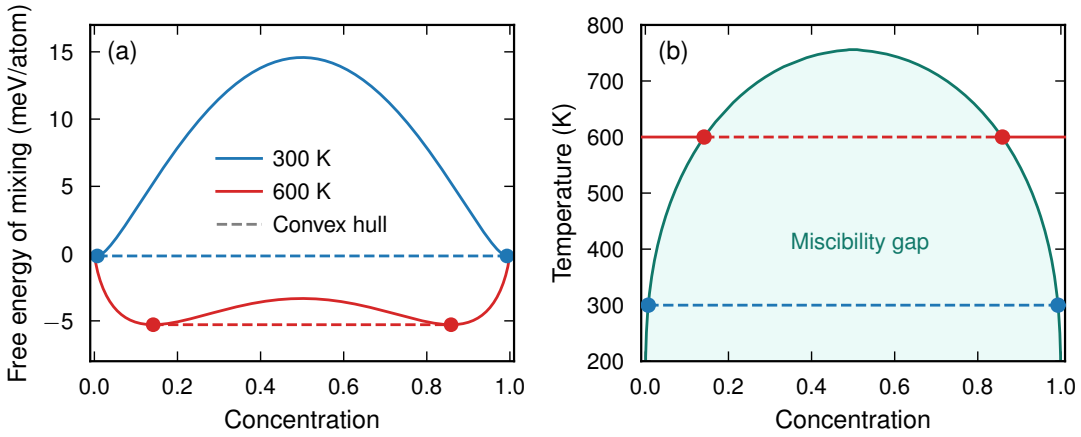

Figure 2.1: Construction of phase diagram from free energy curves in the mean-field approximation of the Ising model (Eq. (2.9)) with $\omega = 0.13$ eV/atom. (a) The free energy curves have two minima that move towards $c = 0.5$ as temperature is increased, and above the critical temperature there is only one minimum. (b) The phase diagram tracks the position of the two minima as a function of temperature.

(in this case the Gibbs free energy[1]) is defined as

$$G = H - TS \tag{2.6}$$

where H is enthalpy, T temperature and S entropy. The enthalpy H depends on the binding energies between the atoms in the material. The largest contribution to the entropy S, on the other hand, is oblivious to the chemistry of the components; it is only a function of how the atoms of type A and B are ordered in the lattice (vibrational and other forms of entropy are neglected here).

The arguably simplest model of a binary alloy is the Ising model, in which the enthalpy is written as a sum of interactions between nearest neighbors. This interaction may take one of two different values, u_0 if the nearest neighbors are alike or $u_{\text{A–B}}$ if they are unlike. In an infinite crystal with completely random order (referred to as an ideal substitutional solid solution), each atom will on average have nc neighbors of type A and $n(1-c)$ neighbors of type B, where n is the number of nearest neighbors for each atom and c the overall concentration of A atoms. It is a simple algebraic exercise to show that the enthalpy of mixing[2] for the system can then be written

$$H_{\text{mix}}(c) = H(c) - cH(1) - (1-c)H(0) = N\omega c(1-c), \tag{2.7}$$

[1]Here we will use energy and enthalpy interchangeably as the the difference between the two, the pressure–volume term, is typically small for solids near ambient conditions.

[2]Mixing energies are tilted such that the energy at $c = 0$ and $c = 1$ is zero by definition. They are often more convenient than total energies when constructing phase diagrams for the sake of visualization, but the physics is the same.

where N is the total number of atoms and $\omega = n(u_{\text{A-B}} - u_0)$. Furthermore, the configurational entropy in the completely random state is

$$S(c) = -Nk_{\text{B}} \sum_i p_i \ln p_i = -Nk_{\text{B}} \left[c \ln c + (1-c)\ln(1-c)\right] \tag{2.8}$$

because each site is occupied by an A or B atom with probability $p_A = c$ and $p_B = 1 - c$, respectively. Putting it together, we have a free energy of mixing per atom

$$G_{\text{mix}}(c) = \omega c(1-c) + k_{\text{B}}T \left[c \ln c + (1-c)\ln(1-c)\right]. \tag{2.9}$$

If the bond between unlike atoms is stronger than the bond between identical atoms, such that $\omega < 0$, then $G_{\text{mix}}(c)$ is negative and convex for all temperatures. If like atoms bind stronger than unlike, however, then the function will have a concave region at sufficiently low temperatures. As derived in the previous section, the system will then phase separate; in other words, it has a miscibility gap. This situation is illustrated in Fig. 2.1 for two values of T along with the resulting phase diagram. The phase boundary for the miscibility gap (the *solvus* line) maps the maximum concentration at which B can dissolve in A or vice versa as a function of temperature. This limit is referred to as the solubility of either element in the other.

2.1.2 Order and disorder in real systems

In the mean-field treatment of the Ising model we assumed random order and arrived at an expression with only one material-dependent parameter, ω. This is of course an oversimplification of a real material. In general, minimization of G leads to a competition between H and TS. If the interaction between unlike atoms is favorable enough, the material will be ordered such that the number of such bonds is larger than in the completely disordered state. An ordered phase has a lower entropy than a random one and will thus only be stable at low enough temperatures. Furthermore, the character of this order will depend on the details of the atomic interaction, for which the Ising model does not in general provide a sufficient description. Nevertheless, by generalizing the Ising model to include interaction between more distant neighbors, as well as clusters of three or more atoms, an accurate model can often be constructed. Such models are known as alloy cluster expansions, and are described in detail in Sect. 5.4, implemented in Paper I and utilized in Paper II and III.

Atomic interaction more complex than the Ising model opens the possibility for more complex phase diagrams. Three examples from the literature are shown in Fig. 2.2 together with schematic free energy curves. The Ag–Cu phase diagram is fairly similar to the Ising model with an unfavorable interaction between the two species, and melting occurs before a solid solution is formed (Fig. 2.2a). The Au–Pd alloy is also reasonably well described by the Ising model but with a favorable interaction between the

two species. Consequently, a solid solution is formed at all compositions at moderately high temperatures (Fig. 2.2b). For Au–Cu, however, the mean-field treatment of the Ising model cannot give a satisfactory description, because in this case the interaction between the two elements is particularly favorable in some configurations such that ordered phases (also called intermetallic compounds) appear in the phase diagram (Fig. 2.2c). These are always surrounded by two-phase regions in accordance with Gibbs' phase rule [15, Chapter 9]. Phase separation can thus occur as a result of unfavorable interaction between the two species, as in Ag–Cu, but also as a result of particularly favorable interaction at some compositions, as in Au–Cu.

It should be noted that also in mixing systems such as Au–Pd, ordered phases are expected to form at sufficiently low temperatures, although these phases may be unreachable in practice since the diffusivity plummets as the temperature is lowered. In fact, in the case of Au–Pd there is no consensus on the exact from of the phase diagram as some authors report ordered phases [20, 21] while others do not [22]. It seems likely that the critical temperatures of these ordered phases are close to room temperature and difficult to reach in practice, but they may be stabilized by strain or other mechanisms and thereby form at higher temperatures in some experiments.

It is in general difficult to predict the mixing behavior of two elements without sophisticated methods. A number of simple rules according to Hume-Rothery [23] do, however, attempt a prediction of whether two elements form a substitutional solid solution:

- the atomic radii should differ by no more than 15 %,
- the crystal structures of the two elements should be similar,
- the two elements should have the same valency, and
- the two elements should have similar electronegativity (if they differ too much, an intermetallic compound is likely to form).

The predictive power of these rules is limited if applied blindly, but they identify a number of parameters that have influence. It is thus reasonable to attribute the low solubility of Ag in Cu and vice versa to their 13 % difference in size [24], and the tendency of Au–Cu to form intermetallic compounds to their 34 % difference in electronegativity [25, 26].

2.1.3 Vacancies as a component

A number of techniques for computational modeling of alloys have been developed over the last 50 years or so (some are described in Chapter 5). In one way or the other, these often rely on a lattice with sites that can assume two or more chemical identities. It is

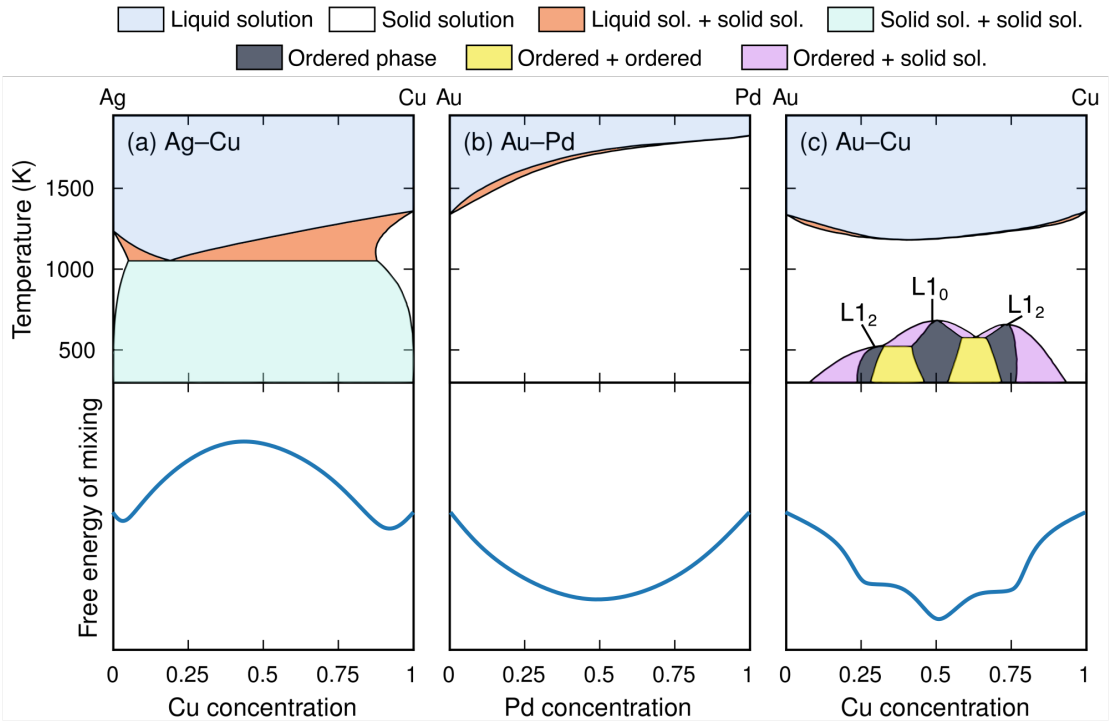

Figure 2.2: Phase diagrams reproduced from the literature together with schematic free energy curves at low temperature (well below the *solidus* lines where melting starts). (a) Ag–Cu [16] is immiscible at all temperatures below the *solidus* line. The free energy of mixing is positive except very close to $c = 0$ and 1. (b) Au–Pd [17] forms a solid solution in the full concentration range (tentative ordered phase have been excluded here). The corresponding free energy of mixing is negative and convex. (c) Au–Cu [18] forms ordered phases at $c = 0.25$ $c = 0.5$ and $c = 0.75$ [19]. These are surrounded by two-phase regions as required by Gibbs' phase rule. The corresponding free energy curve at temperatures where ordering occurs is negative in the full concentration range, but concave regions emerge because the ordered phases have particularly low energy. $L1_0$ and $L1_2$ denote the specific ordering of the intermetallic compounds. $L1_0$ consists of monoelemental atomic planes in the [100] direction, and $L1_2$ is identical except every second atom is substituted for the majority species in the atomic planes of the minority species.

sometimes useful to apply this approach to a system in which one of the chemical identities is a vacancy, i.e., the absence of an atom. The system of a metal species and vacancies can be regarded as an extreme case of an immiscible system. Vacancy-formation energies are usually on the order of an electronvolt or more in transition metals [27], which in the language of binary alloys means that the solubility of vacancies in the metal is very low. Likewise, given the very high boiling temperatures of metals, it is clear that the solubility of metal atoms among vacancies at moderate temperatures is very low too. Simulating the metal–vacancy system is thus mainly relevant for studying the interface between the two phases, i.e., the surface of the metal, primarily in nanoparticles.

This technique was employed in Paper V. The system of vacancies and another chemical species is, however, not always immiscible. Interstitial hydrides, which are discussed in Paper II, Paper III, and the following section, is one such example.

2.2 Hydrogen in palladium and its alloys

We now turn our attention to interstitial solutions of hydrogen in metals. When exposed to H_2 gas, many metals absorb hydrogen. Specifically, H_2 molecules are split on the surface of the metal and subsequently absorbed in atomic form into interstitial sites in the lattice, where, in the language of the preceding section, they form a more or less miscible system with interstitial vacancies. In some metals, the volumetric density of hydrogen can become very high, and they can therefore be used to store hydrogen [28, 29]. Furthermore, as the content of hydrogen increases in the material, its properties are changed. By detecting these changes, hydrogen leakages can be caught. The anticipated need for fast, accurate, and reliable hydrogen sensors in the emerging hydrogen economy has led to a growing research interest in this field [4], and particularly promising for sensing are Pd-based nanoparticles, whose optical properties change upon absorption of hydrogen [11]. This section discusses the thermodynamics of hydrogen in Pd and Pd-based alloys, as the thermodynamics underpin the behavior of the system and by extension the response of optical sensors.

2.2.1 Why palladium?

Pd is sometimes described as a hydrogen sponge, since it readily absorbs large quantities when exposed to a H_2 gas. Just as important is the fact that the hydrogen is also easily desorbed when the H_2 pressure is lowered. In the dilute limit (i.e., low hydrogen concentration in the material), this can be quantified with Sieverts' law [30]. This law states that the solubility of a diatomic gas (such as H_2) is proportional to the square root of the partial pressure of said gas, $c_H = k\sqrt{p_{H_2}}$, where the constant of proportionality can be expressed as

$$k \propto \exp\left[-\frac{\Delta H_0 - T\Delta S_0}{k_B T}\right]. \tag{2.10}$$

Here, ΔS_0 is the change in non-configurational entropy per H atom upon absorption, whereas ΔH_0 is the change in enthalpy at infinite dilution. The change in entropy differs only slightly between different metals since its primary contribution is from the entropy decrease in the gas [31, Chapter 2]. The change in enthalpy is thus the primary measure that determines whether the material will absorb and desorb hydrogen to a sufficient extent in the H_2 pressure interval of interest. For Pd, the experimental value [32] of the enthalpy change is $\Delta H_0 \approx 0.1\,\mathrm{eV/atom}$, which is small enough to partially explain its sponge-like behavior. This can be compared to for example Au ($\Delta H_0 \approx 0.4\,\mathrm{eV/atom}$),

which absorbs very little hydrogen, or Hf ($\Delta H_0 \approx -0.4\,\mathrm{eV/atom}$), for which the hydride will be stable even close to vacuum (in which case Sieverts' law essentially breaks down, as the hydride becomes non-dilute even at infinitesimally small pressures). The Hf hydride may still be useful for hydrogen sensing as the hydrogen content varies with pressure but in a different regime [33], but it is unlikely to be useful for hydrogen storage as full hydrogen desorption is infeasible at ambient temperatures.

2.2.2 The phase transition

It is important to note that Sieverts' law holds only in the dilute limit, where the hydrogen atoms in the material do not interact with each other. At higher concentrations, hydrogen–hydrogen interaction makes the situation more complex. In the case of Pd, the enthalpy curve turns out concave between the dilute limit and $c_\mathrm{H} \approx 2/3$ (Fig. 2.3a). As a consequence, the system phase separates into a dilute phase, usually labeled α, and a dense hydride, β (Fig. 2.3b–c). These phases are both solid solutions of hydrogen, with the difference being the density of hydrogen.

Here, it should be noted that the (Pd–)H–vacancy system and a regular binary alloy are quite different from an experimental standpoint. Although we may view the interstitial sites as a sublattice containing two species, hydrogen and vacancies, which adheres to the same principles as any binary alloy, in experiment it is almost always the chemical potential of hydrogen that is controlled (via the partial H_2 pressure), and not its conjugate thermodynamic variable (the concentration). It follows that the phase-separated system, with α and β coexisting, is seen at most temporarily while the phase transition from α to β or β to α occurs.

Experimentally, the phase transition can be observed by fixing the temperature and tracking the hydrogen content in the material as the partial pressure of H_2 in the surroundings is slowly increased. The phase transition manifests itself as a discontinuity in the corresponding isotherm (Fig. 2.3d); at a specific pressure, called the plateau pressure, the hydrogen content increases abruptly. If the H_2 pressure is then lowered, hydrogen will desorb from the material. The phase transition from β to α will, however, occur at a lower H_2 pressure; the system exhibits hysteresis. Thermodynamically, hysteresis is the result of an energy barrier between the two phases. In many systems, this energy barrier can be well described by assuming that a sufficiently large nucleus of the new phase has to form before the free energy can be lowered, and that this is an event driven by fluctuations that can essentially be waited out, meaning the hysteresis will decrease if the experiment is run more slowly. An important exception, however, are coherent phase transitions, which are relevant for the hydrogenation of Pd nanoparticles and are discussed in Sect. 2.3.

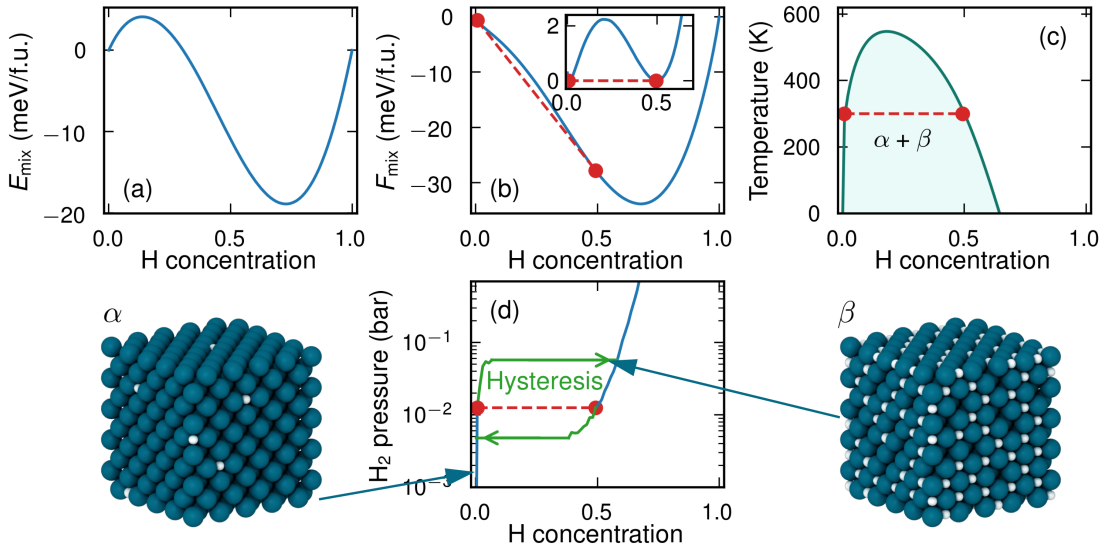

Figure 2.3: Thermodynamics of the Pd–H system. (a) The energy of mixing at 300 K is positive at dilute concentrations but negative otherwise, creating a wide concave region from approximately $c = 0$ to $c = 2/3$. The enthalpy at infinite dilution (ΔH_0) is directly related to the slope at $c \to 0$. (b) In the free energy of mixing at 300 K, the concave region is barely discernible. Yet by tilting the free energy curve (inset figure), it becomes apparent that the concavity persists, and the convex hull (red, dashed line) consequently lies below the free energy curve. (c) The limits of the concave interval define the two-phase ($\alpha + \beta$) region when plotted as a function of temperature in a phase diagram. (d) The most commonly reported experimental quantity is the isotherm, i.e., content of hydrogen as H_2 pressure is increased at constant temperature (here 300 K). The concentration changes discontinuously at the plateau pressure (red, dashed curve), but this phase transition is associated with hysteresis (green curves), which means the system transitions at a higher (lower) pressure upon loading (unloading). The two phases have the same (lack of) symmetry and differ only in the concentration of hydrogen on the interstitial lattice (inset figures). The data presented here were generated with the cluster expansion developed in Paper III. Energies are plotted per formula unit (1 f.u. = 1 Pd atom + 1 interstitial site) and concentrations are defined as number of H atoms per Pd atoms.

2.2.3 Hydrogen in palladium-based alloys

If we want to use Pd as a hydrogen sensor, the phase transition is undesirable, because it renders the relationship between H_2 pressure and hydrogen content (and by extension sensor readout) non-linear, and with hysteresis the correspondence between hydrogen content and H_2 pressure is not one-to-one. By studying the enthalpy curve in Fig. 2.3a, we can devise a plan to suppress the two-phase region in order to make a better sensor. The agent responsible for the two-phase region is the increase in enthalpy in the dilute limit, compared to the lower enthalpy in the dense hydride. If the enthalpy of infinite dilution (ΔH_0) is lowered, while simultaneously the enthalpy in the dense hy-

dride is increased, the two-phase region can be expected to disappear. The difference between the enthalpy of dilute and dense solution in Pd–H is usually attributed to the energetic penalty of elastic dilation of the lattice. Inserting one hydrogen atom is associated with a significant elastic energy penalty, because the lattice needs to expand in the vicinity of the interstitial. But when the next hydrogen atom is absorbed, the lattice is already slightly expanded by the presence of the first, and the elastic energy penalty is thus lower for the second atom. One could thus imagine that by pre-straining the lattice by alloying with a chemical species larger than Pd, the elastic energy penalty would decrease also at infinite dilution of hydrogen. By studying the enthalpy at infinite dilution (ΔH_0) in Pd-based alloys, a clear correlation between the size of the alloying element and the enthalpy is found, with elements larger than Pd lowering ΔH_0 [31, 34]. At the same time, if the chemical interaction between the alloying element and hydrogen is unfavorable compared to Pd, the enthalpy becomes relatively higher when the hydride becomes dense, which should further suppress the concavity in the enthalpy curve. To summarize, alloying with a chemical species that is larger and has a less favorable hydrogen interaction than Pd, should shrink the two-phase region.

An example of such an element is Au, which has a lattice parameter that is 4.9% larger than Pd [24] and an enthalpy at infinite dilution $\Delta H_0 \approx 0.4\,\mathrm{eV/atom}$, compared to 0.1 eV/atom for Pd [32]. Indeed, with with a sufficiently large fraction of Au in Pd, the two-phase region is completely suppressed (Fig. 2.4). A similar behavior is found for Ag, which is 5.1% larger than Pd [24] and has $\Delta H_0 \approx 0.7\,\mathrm{eV/atom}$ [32]. In what follows, the focus will be the Pd–Au alloy.

2.2.4 Equilibrium in alloy hydrides

By introducing another chemical species, it becomes significantly more complex to predict and understand the properties of the material. In addition to the compositional degree of freedom, the chemical ordering of the chemical species can be expected to play a role. It is important to note that the two sublattices, Pd–Au and hydrogen–vacancy, are very different from a kinetic perspective. Hydrogen, being a small and light atom, diffuses easily on the interstitial lattice, meaning equilibrium will usually be reached very quickly [37]. The Pd and Au atoms, on the other hand, diffuse very slowly and will typically require both high temperatures and long times to reach equilibrium. For many practical purposes it is therefore reasonable to assume that the Pd–Au sublattice is frozen—the atoms do not change places with one another—while equilibrium forms on the H–vacancy sublattice. This situation is referred to as para-equilibrium [38, 39].

We may further distinguish different para-equilibria depending on how the Pd–Au sublattice is frozen in. Experimentally, the Pd–Au alloy is usually formed through an annealing process, during which the system is held at an elevated temperature for an extended period of time, and then cooled. If the annealing time is long enough and the material is cooled rapidly, we can expect that the Pd–Au sublattice has been frozen in

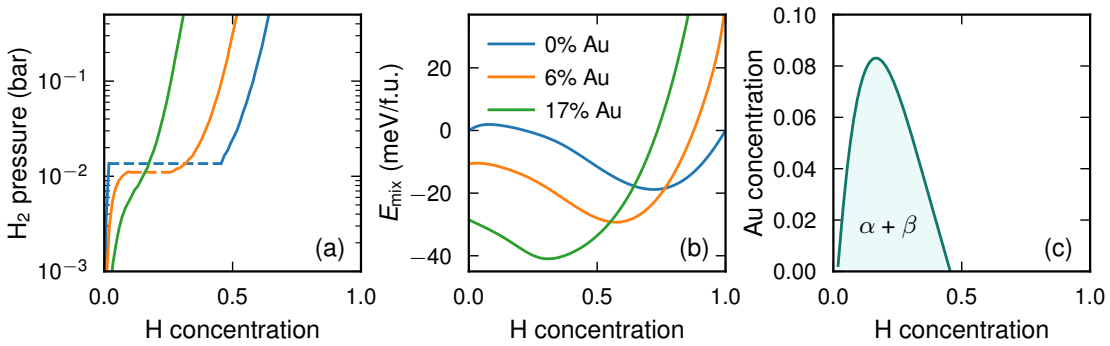

Figure 2.4: Thermodynamics of the Pd–Au–H system in para-equilibrium (see Sect. 2.2.4). (a) Isotherms at 300 K reveal that below the plateau pressure, the content of hydrogen at a fixed H_2 pressure increases by addition of Au, whereas the opposite holds above the plateau pressure. The plateau pressure does not change much with Au content, but it disappears if a sufficiently large Au concentration is reached. (b) The corresponding energy of mixing reveals that the slope at $c = 0$ (corresponding to ΔH_0) decreases and becomes negative with an increased amount of Au. Meanwhile, the minimum in the mixing energy shifts to lower concentrations. (c) These effects jointly act to suppress the two phase region in the phase diagram at 300 K. The data presented here were generated with the cluster expansion developed in Paper II. The critical Au concentration at which the two-phase region is suppressed is lower in this model than in most experiments [35, 36].

the equilibrium chemical ordering at the annealing temperature. On the other hand, if the material is cooled slowly, we may assume that the system is approximately in equilibrium at the final temperature (often room temperature). The chemical ordering on the Pd–Au sublattice will be at least slightly different in the two cases. When the material is then exposed to hydrogen, it may behave differently depending on what chemical order was formed during annealing. In Paper II, we identified two extremes; infinitely slow cooling to 300 K, and rapid cooling from infinite temperature (disregarding melting). We reserved the term para-equilibrium for the former and used random equilibrium to denote the latter, since the chemical order will be fully random if it is annealed at infinite temperature.

A different situation arises if full (sometimes called complete) equilibrium is allowed to form. This would be the case if the Pd–Au sublattice is allowed to rearrange in response to the presence of hydrogen. The low diffusivity of the Pd–Au sublattice at moderate temperatures makes it time-consuming to reach this equilibrium experimentally, but it is by no means impossible as has been shown in studies on Pd–Au [22] and Pd–Mn [40], and even in the absence of full equilibrium, it provides the driving force for the changes that occur on a Pd–Au sublattice not yet in equilibrium. In Paper II, we constructed the phase diagram in full equilibrium as well, showing that it is significantly more complex than in para-equilibrium due to formation of an ordered phase at ap-

proximately 25% Au. Under most conditions, this ordered phase absorbs significantly more hydrogen than the disordered phase, and knowledge of the equilibrium situation is thus important when comparing hydrogen absorption isotherms.

2.3 Coherent phase transitions

The phase diagram construction described in Sect. 2.1 relies on the assumption that the free energy of the phase separated system is the sum of the free energies of its constituent phases. This assumption is violated by the energy associated with the interface between the phases, but since the interface energy contribution scales with area while the free energies of the phases scale with volume, it can be ignored for sufficiently large samples. If the two phases have different equilibrium lattice parameters, however, more complicated situations can emerge. In many materials, dislocations form at the interface between the two phases to accommodate the differing lattice parameters (lower inset in Fig. 2.5a). Such defects typically contribute to a higher interface energy, but can be energetically favorable since stresses far from the interface are relieved. In some materials, however, no such defects tend to form. The interface instead remains fully coherent, i.e., the atomic planes line up (upper inset in Fig. 2.5a). In this case, the interface energy may be lower than in the incoherent case, but the constituent phases are strained. This strain contributes an energy that scales with volume, and thereby violates the assumptions underpinning the phase diagram construction described in Sect. 2.1. This leads to a behavior distinct from conventional, stress-free thermodynamics [41–44].

Experiments have shown that the α/β interfaces formed during hydrogenation of single-crystalline Pd nanoparticles less than about 300 nm in diameter are predominantly coherent [45–47]. Since there is a significant size-mismatch between the α and the β phase, hydrogenation of Pd nanoparticles is subject to the distinct characteristics of coherent interfaces.

To better understand the consequences of coherent interfaces, we can write the free energy of the coherently phase-separated system as a minimization problem,

$$G_{1+2}^{\text{coherent}}(c_{\text{av}}) = \min_{c_1,\, c_2} \Big\{ \underbrace{\alpha_1 G(c_1) + \alpha_2 G(c_2)}_{\text{bulk free energy}} + \underbrace{V e_{\text{strain}}(c_{\text{av}}, c_1, c_2)}_{\text{strain}} \Big\}. \tag{2.11}$$

Here, c_{av} is the overall concentration of the full sample, which is phase separated into phases 1 and 2 with respective concentrations c_1 and c_2 in proportions α_1 and α_2. The bulk free energy term is the same as Eq. (2.4), while the average strain energy density e_{strain} associated with the coherent interface contributes a new term that scales with volume V. Here, we have once again ignored the interface energy since it scales with area, and we have not written out explicitly that the strain energy e_{strain} depends on the orientation

of the interface. Moreover, Eq. (2.11) is approximate since the (chemical) free energy of the constituent phases can be expected to be at least weakly dependent on the degree of strain in the system.

Equation (2.11) is a minimization problem in the concentrations of the two phases, c_1 and c_2. In the absence of strain, this is exactly the problem that is solved by the convex hull construction discussed in Sect. 2.1. With strain, however, Eq. (2.11) will not be minimized by the convex hull construction. In general, a small difference between c_1 and c_2 leads to a smaller strain energy, because the difference in equilibrium lattice parameter between the two phases decreases when the difference between c_1 and c_2 decreases. The minimum in Eq. (2.11) is thus typically found for c_1 and c_2 inside the convex hull construction, i.e., coherency strain shrinks the two-phase region.

It is instructive to depict the energetics of the incoherent and the coherent case graphically (Fig. 2.5). The difference in chemical potential $\Delta\mu$ between the two species maps to multiple concentrations c inside a two-phase region (black line in Fig. 2.5a). This form of $\Delta\mu$ is equivalent to a barrier in the free energy (Fig. 2.5b), which is obtained by integration of $\Delta\mu$. At this point, it is worth noting that the black lines in Fig. 2.5 are somewhat artificial constructions inside the two-phase region. They should be understood as the equilibrium states *under the constraint* that the system has a spatially homogeneous concentration, i.e., no phase separation is allowed. As we saw in Sect. 2.1, these are *not* the lowest possible free energies for a given concentration, because incoherent phase separation can lower it. In the incoherent case, we know from Sect. 2.1 that the convex hull yields the lowest free energy (green lines in Fig. 2.5). The convex hull construction defines the boundaries of the two-phase region in the incoherent case, here denoted c_1^{incoh} and c_2^{incoh} (also referred to as binodals). In the coherent case, Eq. (2.11) can be applied. The typical result is a sloping $\Delta\mu$–c isotherm that connects two concentrations c_1^{coh} and c_2^{coh}, which fulfill $c_1^{\text{coh}} > c_1^{\text{incoh}}$ and $c_2^{\text{coh}} < c_2^{\text{incoh}}$ [48, 49] (orange line in Fig. 2.5a). Such a sloping plateau is associated with a free energy barrier (orange line in Fig. 2.5a).

In open systems (such as Pd subject to a certain partial pressure of H_2) it is particularly important to note that the free energy barrier in the coherent case is a macroscopic barrier, because it scales with the total number of sites and thereby the macroscopic volume of the sample. This distinguishes the coherent energy barrier from the barrier associated with incoherent interface energy, which scales with area and thereby is microscopic, i.e. it is comparable to $k_B T$ and can be overcome with nucleation and growth. With an energy landscape like the one in Fig. 2.5, the macroscopic energy barrier can only be overcome by increasing the partial pressure (or equivalently $\Delta\mu$) until the concentration has reached the coherent phase boundary (c_1^{coh} during absorption, c_2^{coh} during desorption). Since the plateau is sloping in the coherent case, the $\Delta\mu$ required to transition from left to right is higher than the $\Delta\mu$ required to transition from right to left. The system will thus exhibit hysteresis. This hysteresis, which was first discussed by Schwarz and Khachaturyan [48, 49], is entirely thermodynamic in origin and cannot

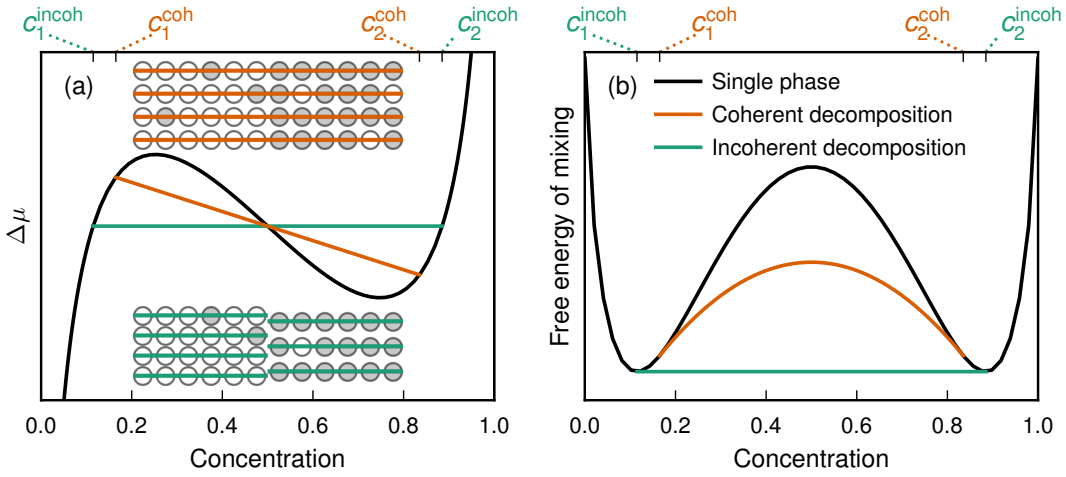

Figure 2.5: Schematic energy landscape for a binary alloy with a miscibility gap. (a) The difference in chemical potential $\Delta\mu$ between the two species as a function of concentration. If the system is forced to stay in a single-phase configuration with a spatially homogeneous concentration, a miscibility gap can be recognized as, for example, the presence of a maximum and a minimum in $\Delta\mu$ (black line). If incoherent phase separation is allowed (lower inset), the system transforms from c_1^{incoh} and c_2^{incoh} along a straight line (green line). If the interface is coherent (upper inset), the $\Delta\mu$–c curve will instead have a negative slope inside the miscibility gap, which connects the coherent phase boundaries c_1^{coh} and c_2^{coh}. (b) The free energy of mixing is obtained by integration of $\Delta\mu$. The incoherent phase transition (green line) is entirely free from energy barriers (as long as interface energies can be ignored). The coherent phase transition, on the other hand, needs to pass a free energy barrier, but in the present case this barrier is lower than in the single-phase case, where the concentration changes homogeneously throughout the sample.

be avoided as long as the interface is coherent.

Compared to the strain-free case, the phase diagram is more complicated when coherent phase transitions occur. To better understand the temperature-dependent behavior, we can study a prototypical system as a function of temperature (Fig. 2.6). The situation depicted in Fig. 2.5 corresponds to low temperatures (Fig. 2.6a). Incoherent phase separation can occur for $c_1^{\text{incoh}} < c < c_2^{\text{incoh}}$ (green dots), while coherent phase separation can only occur for $c_1^{\text{coh}} < c < c_2^{\text{coh}}$ (orange diamonds). When the temperature is increased (Fig. 2.6b), the system reaches a regime where the coherent phase boundaries are inside the (incoherent) spinodals, i.e., the maximum and the minimum in $\Delta\mu$ (purple squares). At this temperature, the phase transition in the open system will start to occur spontaneously before there is phase coexistence between the two phases. With an even higher temperature (Fig. 2.6c), the coherent phase transition will occur without any coexistence between the two phases; the sample will remain spatially homogeneous throughout the whole phase transition. For a sufficiently high temperature (Fig. 2.6d),

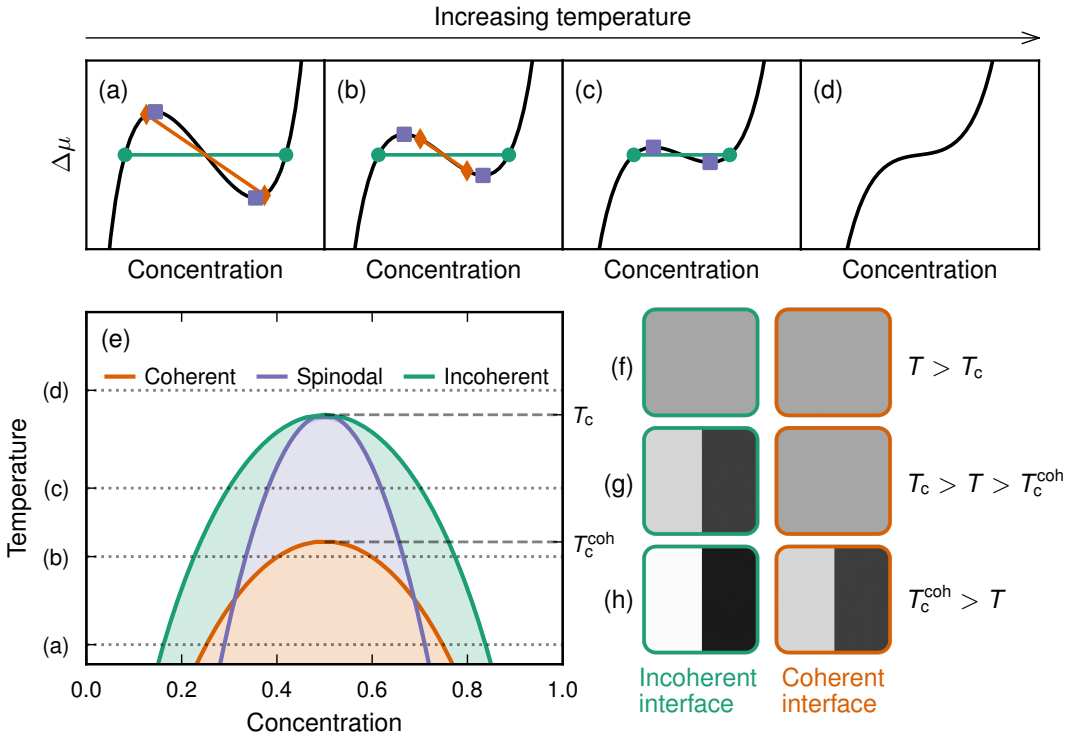

Figure 2.6: Schematic phase diagram construction for a system with incoherent or coherent interfaces. (a–d) $\Delta\mu$–c isotherms at increasing temperatures. The coherent phase boundaries (orange diamonds) are always inside the incoherent phase boundaries (green circles). In (b) the coherent phase boundaries are inside the spinodals (purple squares) as well, in (c) there is no coherent phase coexistence at all and in (d), incoherent phase coexistence disappears as well. (e) The two critical temperatures T_c and T_c^{coh} can be read from the phase diagram. Above T_c, there is no phase transition and thus no phase coexistence (f). Below T_c but above T_c^{coh}, the two phases will coexist during the phase transition if it is incoherent, but if it is coherent, the system will maintain a homogeneous concentration distribution throughout the full phase transition (g). Below T_c^{coh}, the two phases will coexist during the phase transition regardless of whether it is incoherent or coherent (h).

there is no miscibility gap and there is no need to distinguish coherent systems from incoherent ones.

The (incoherent[3]) spinodals are significant also in the coherent, open system, because they mark the concentrations where all free energy barriers are gone and the phase transition can occur spontaneously. To demonstrate this, it is advantageous to consider the

[3]Incoherent spinodals are defined by $\partial^2 G/\partial c^2 = 0$ and are important for incoherently phase separating systems, because such systems are unstable with respect to formation of concentration waves when $\partial^2 G/\partial c^2 < 0$. Coherent spinodals, where the system is unstable with respect to coherent phase separation, exist too but are not relevant for our analysis of the open system.

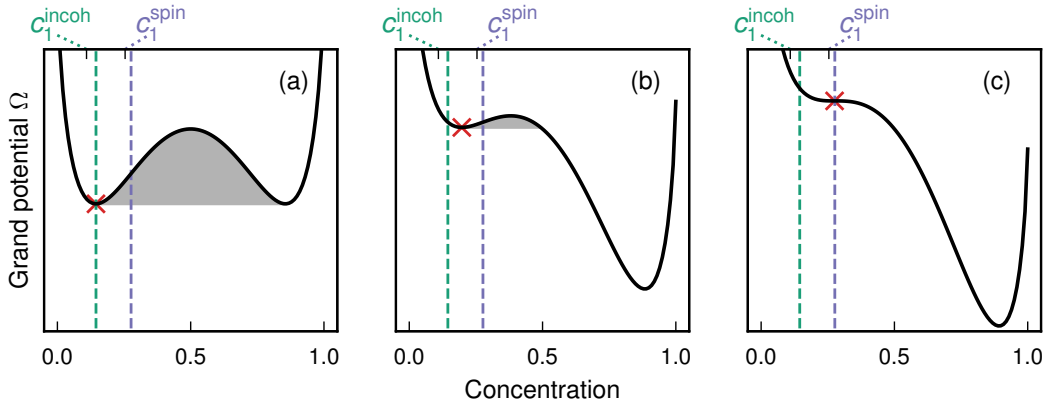

Figure 2.7: Significance of the incoherent spinodal in an open system that does *not* transition incoherently. (a) Even if the chemical potential μ is such that the grand potential Ω is the same in phase 1 and phase 2, the *coherent* phase transition from 1 to 2 (or vice versa) cannot occur, because there is a macroscopic energy barrier (shaded grey) that prevents it. (b) If μ is increased, phase 2 will be lower in energy than phase 1. Yet, the free energy barrier still prevents the phase transition, and the system will remain in a metastable state with only slightly higher concentration than c_1^{incoh} (red cross). (c) When μ has been increased such that the metastable state coincides with the incoherent spinodal (dashed, purple line), the free energy barrier is gone, and the system can transition to phase 2 spontaneously. If the coherent phase boundary lies outside the spinodal ($c_1^{\text{coh}} < c_1^{\text{spin}}$), the phase transition may occur already at c_1^{coh} (because the remaining barrier is only microscopic), but if it lies inside ($c_1^{\text{coh}} > c_1^{\text{spin}}$), the spinodal marks the concentration where the phase transition starts.

grand potential $\Omega = H - TS - \mu c N_{\text{tot}}$, which is minimized in equilibrium in open systems (here μ is the chemical potential of the species being absorbed, c is the fraction of sites occupied, and N_{tot} is the total number of sites). Let us further (without loss of generality) assume that $\partial G/\partial c = 0$ at the incoherent phase boundaries c_1^{incoh} and c_2^{incoh} (Fig. 2.7a). When $\mu = 0$, the grand potential of phase 1 and phase 2 are then equal. As soon as $\mu > 0$, the grand potential is minimized by phase 2 only. During an absorption cycle, the phase transition will, however, not occur immediately, because there is still a macroscopic free energy barrier (caused by the volumetric strain energy contribution) to pass from phase 1 to phase 2, and the system will stay in the metastable state on the phase 1-side where $\partial G/\partial c = \mu$ (Fig. 2.7b). It is not until μ is increased to the point where $\partial^2 G/\partial c^2 = 0$ (the spinodal) that the barrier is completely gone, and the phase transition can proceed spontaneously (Fig. 2.7c).

We can now summarize the temperature-dependent behavior in a phase diagram (Fig. 2.6e). It is clear that two critical temperatures need to be distinguished; the usual one where the incoherent two-phase region closes (T_c), and the coherent critical temperature (T_c^{coh}) above which there can be incoherent phase coexistence during the phase

transition, but no coherent phase coexistence. It should be stressed that also in the interval between T_c^{coh} and T_c, there is always a phase transition from phase 1 to phase 2 (and vice versa) that is associated with a jump in the isotherm as well as hysteresis, but the pathway of the phase transition is different from below T_c^{coh}.

In Paper III, we develop and apply a methodology for calculating the most important thermodynamic quantities, including the phase diagram, of the Pd–H system under the assumption that interfaces remains coherent. Our results predict a critical temperature of $T_c = 540$ K and a coherent critical temperature of $T_c^{coh} = 400$ K. While T_c is within 20 K of the experimental value [50], the coherent critical temperature T_c^{coh} has to the best of our knowledge previously only been approximated with simple continuum models [51] (and its existence may well be unknown to many in the field). It is important to emphasize that while the exact experimental value of T_c^{coh} might differ from our simulations, its principle existence is dictated by thermodynamics.

The hydrogenation process of Pd nanoparticles has been intensely and very successfully studied experimentally during the last decade using advanced imaging techniques, but these experiments have for technical reasons primarily been performed at temperatures well below T_c^{coh}, where there is an unmistakable $\alpha + \beta$ phase coexistence [47, 52]. The conclusions from these experiments may need careful reexamination before they are generalized to higher temperatures, since as discussed above the phase transition occurs without $\alpha + \beta$ phase coexistence above T_c^{coh}; a structurally completely different behavior.

3

Shapes and structures of nanoparticles

They say no two snowflakes are alike, but the same statement would not be true for metallic nanoparticles. Being made of materials that are crystalline at room temperature, they tend to form highly regular structures that usually can be categorized as shapes well-known from fundamental geometry. This chapter explains the emergence of these particle shapes from a continuum perspective and discusses when the continuum approach needs to be replaced by a model with atomistic resolution. Nanoalloys (nanoparticles consisting of two or more metals) and ensembles of nanoparticles are also treated briefly.

3.1 A simple model for the energy

The equilibrium shapes of nanoparticles are governed by the energetics of the materials of which they are made. The total energy of a nanoparticle may, as a first model, be written as a polynomial in the particle volume V,

$$E_{\text{nanoparticle}} = aV + bV^{2/3} + cV^{1/3} + d. \tag{3.1}$$

The first term incorporates all contributions that scale with the volume of the particle, including cohesive energy and strain. The second term, $bV^{2/3}$, includes the energy of the surface and any other contributions that scale with area. The third term, $cV^{1/3}$, accounts for linear defects such as edges. The fourth term, d, is made up of any zero-dimensional contribution, including corners and point defects. The coefficients are themselves functions of the shape of the particle. A cube, for example, has edges and corners whereas

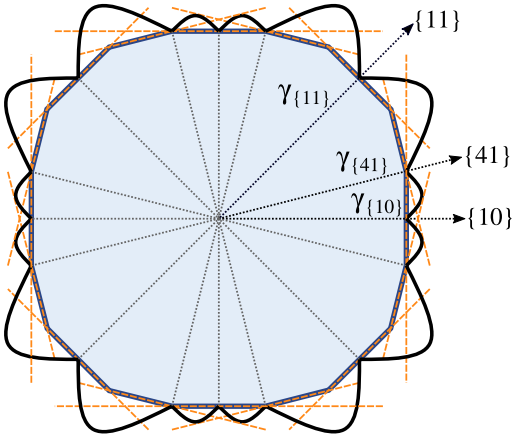

Figure 3.1: Wulff construction in two dimensions. The distance from the origin to the thick black line is proportional to the surface energy for a surface with that crystal orientation, i.e., the thick black line denotes $\gamma(\hat{\boldsymbol{n}})$. In this hypothetical example, three inequivalent facets are exposed in the optimal shape (filled with blue), namely {10}, {11} and {41}.

a sphere does not, and hence we expect c and d to be much larger for the cube than the sphere.

To find the equilibrium nanoparticle shape we need to find the shape whose coefficients minimize Eq. (3.1) for a given volume. For water or any other liquid, this problem is trivial; the lowest energy shape is always a sphere because a sphere has the smallest possible surface area for a given volume (and any contribution from edges or corners is always positive). For crystals, however, the problem is non-trivial, because the surface energy of a crystal is facet-dependent, i.e., it depends on the orientation of the surface. Also, a crystal may be strained and incorporate defects that will contribute to any of the coefficients a, b, c or d depending on their dimensionality. This gives rise to a rich variety of particle structures, which are stable at specific sizes in specific materials. The situation calls for refined models in which the effects of crystallinity are accounted for.

3.2 The Wulff construction

The Wulff construction [53, 54] solves the problem of finding the optimal particle shape given a set of facet-dependent surface energies. Wulff constructions are based on polar plots of surface energy, $\gamma(\hat{\boldsymbol{n}})$, where the distance from the origin to the surface in a certain direction $\hat{\boldsymbol{n}}$ is proportional to the surface energy of a facet with that orientation. Planes are drawn perpendicular to each $\hat{\boldsymbol{n}}$, and the optimal shape is finally obtained as the inner envelope of such planes. The procedure is outlined graphically in Fig. 3.1 for a two-dimensional case.

While a rigorous proof of the Wulff construction can be daunting, a motivation for its validity can be given in simple terms [55]. Consider a set of surface energies $\gamma(\hat{\boldsymbol{n}}_i)$. With distances h_i from the origin to each facet, and with corresponding facet areas A_i, we can write the total surface energy as

$$E_{\text{surface}} = \sum_i \gamma(\hat{\boldsymbol{n}}_i) A_i \tag{3.2}$$

and the volume of the particle as

$$V = \sum_i \frac{1}{3} h_i A_i. \tag{3.3}$$

We want to minimize the total surface energy for a fixed volume V_0. The latter condition can be handled with a Lagrange multiplier,

$$\delta \left[E_{\text{surface}} - \lambda (V - V_0) \right] = \sum_i \delta \left(\gamma(\hat{\boldsymbol{n}}_i) A_i - \lambda \frac{1}{3} h_i A_i \right) = 0 \tag{3.4}$$

where the variation vanishes for the minimum energy shape. The method of Lagrange multipliers asserts that the terms vanish independently, so that

$$h_i \propto \gamma(\hat{\boldsymbol{n}}_i) \tag{3.5}$$

with the same constant of proportionality for all facets i. This is the condition required by the Wulff construction. Mathematically, we can thus write the Wulff shape as the set $\mathbb{W}$ of points $\boldsymbol{x}$ that fulfill

$$\mathbb{W} = \{ \boldsymbol{x} \,:\, \boldsymbol{x} \cdot \hat{\boldsymbol{n}} \leq k\gamma(\hat{\boldsymbol{n}}) \text{ for all } \hat{\boldsymbol{n}} \}, \tag{3.6}$$

where k is a constant of proportionality that can be varied to obtain a specific volume.

3.2.1 Implementation of the Wulff construction

From a computational perspective, it is possible to solve the Wulff construction by brute force. With $\gamma(\hat{\boldsymbol{n}}_i)$ as input, we can construct planes with unit normal $\hat{\boldsymbol{n}}_i$ at a distance $\gamma(\hat{\boldsymbol{n}}_i)$ from the origin. We then find all intersections between these planes, and discard those that do not fulfill Eq. (3.6). The remaining intersections constitute the vertices of the Wulff shape. Unfortunately, this method scales poorly with the number of planes ($\mathcal{O}(N^4)$, where N is the number of planes) and thus becomes very slow when the surface energy is specified for many orientations.

A much faster method can be conceived [56] by making use of the concept of dual polyhedra [57, Chapter 3]. The vertices of a polyhedron correspond to the faces of its dual,

and vice versa, and the dual of the dual is the original polyhedron. Consider a vertex $\boldsymbol{v} \in \mathbb{W}$. By the definition of dual shapes, this vertex corresponds to a plane with unit normal $\hat{\boldsymbol{n}}_{\text{dual}} = \boldsymbol{v}/|\boldsymbol{v}|$ on a distance $1/|\boldsymbol{v}|$ from the origin. A plane in the original shape, on the other hand, with unit normal $\hat{\boldsymbol{n}}$ on a distance $k\gamma$ from the origin corresponds to a vertex $\boldsymbol{v}_{\text{dual}} = \hat{\boldsymbol{n}}/k\gamma$. The vertex $\boldsymbol{v}_{\text{dual}}$ lies inside the plane with unit normal $\hat{\boldsymbol{n}}_{\text{dual}}$ because

$$\boldsymbol{v}_{\text{dual}} \cdot \hat{\boldsymbol{n}}_{\text{dual}} = \frac{\hat{\boldsymbol{n}} \cdot \boldsymbol{v}}{k\gamma|\boldsymbol{v}|} \leq \frac{k\gamma}{k\gamma|\boldsymbol{v}|} = \frac{1}{|\boldsymbol{v}|}, \tag{3.7}$$

where we used the condition that $\boldsymbol{v}$ fulfills the Wulff criterion (Eq. (3.6)) to obtain the inequality. Conversely, any plane that lies inside the vertex $\boldsymbol{v}_{\text{dual}}$, corresponds to a vertex in the original shape that is outside the Wulff shape. Finding the Wulff shape is thus equivalent to finding the smallest, convex polyhedron that exactly contains all dual vertices $\boldsymbol{v}_{\text{dual}}$, i.e., the convex hull. Fortunately, this is a well-studied problem and algorithms that reduce the complexity to $\mathcal{O}(N^2)$ or less exist [58]. Since the dual of the dual is the original shape, we can calculate the Wulff shape by (1) calculating the dual shape by converting each tentative face to its dual vertex, (2) discarding all vertices not on the convex hull, and (3) converting the thus obtained shape to its dual. The result is the Wulff shape. This was implemented in Paper IV with the aid of the QUICKHULL algorithm [58] as interfaced in SCIPY [59].

3.2.2 Symmetries and twinned particles

The facet-dependent surface energy $\gamma(\hat{\boldsymbol{n}})$ must of course have the same symmetry as the crystal structure from which it is derived. This means that it is sufficient to specify surface energies for Miller indices in the irreducible Brillouin zone and then apply the symmetry operations of the point group of the crystal to obtain the remaining surface energies.

In light of this, constructing the Wulff shape for systems with broken symmetry does not pose any significant additional difficulties. This applies, for example, to particles in contact with a flat surface. The contact breaks the symmetry; the energy is different for the facet in contact with the surface and crystallographically equivalent facets that are in contact with the environment. As long as the normal to the interface as well as the interface energy can be provided (in addition to $\gamma(\hat{\boldsymbol{n}})$), the Wulff construction, in this case often referred to as a Winterbottom construction [60], can proceed as normal. Another important case of broken symmetry are twinned particles [61] such as decahedra (Sect. 3.3.2) and icosahedra (Sect. 3.3.3), which are polycrystalline particles with identical grains that share twin boundaries. After specifying the twin boundary energy and acknowledging the broken symmetry, the Wulff construction can be carried out as normal, and the full particle can eventually be constructed by patching together the grains.

3.3 Nanoparticle shapes

Equipped with the Wulff construction, the only task remaining is to find the facet-dependent surface energies. This is almost impossible experimentally, but tractable computationally. It should be stressed that surface energies are strongly dependent on environment. The equilibrium shape of nanoparticles in vacuum are thus not necessarily the same as nanoparticles of the same material in solution. This issue is addressed in Paper VII.

Fig. 3.2 (right) shows surface energies for Au as calculated with density-functional theory (DFT) in Paper VII. The results are representative for face-centered cubic (FCC) metals and can be rationalized by a simple bond-counting model; facets that minimize the number of broken bonds also have the lowest energies, which typically means that the close-packed {111} surface is the lowest energy facet in FCC metals. This section introduces some shapes that are primarily relevant for materials with cubic symmetry and for which the {111} facet has the lowest energy.

3.3.1 Truncated octahedra

The Wulff shape resulting from the surface energies of Au can be described as a truncated octahedron (Fig. 3.2a). The lowest energy facet, {111}, does indeed have the largest area, followed by {100} and {110}. Note that a complete (not truncated) octahedron has only {111} facets, but according to the Wulff construction, it is still not the lowest energy structure because of its high surface-to-volume ratio. In this thesis, octahedra that are truncated such that the hexagonal {111} facets are equilateral (disregarding {110}) are referred to as regular truncated octahedra (RTOs). In the Wulff construction they emerge when

$$\frac{\gamma_{100}}{\gamma_{111}} = \frac{2}{\sqrt{3}} \approx 1.15, \tag{3.8}$$

i.e., when the surface energy of the {100} surface is approximately 15 % larger than the surface energy of {111} (all other surfaces disregarded).

3.3.2 Truncated decahedra

The original Wulff construction assumes a single crystalline particle. If this requirement is relaxed, it is possible to construct particles with lower surface energy than the Wulff shape. Stacking five truncated tetrahedra such that they share an edge (Fig. 3.2b) produces one such example, a truncated decahedron [62]. This shape was first observed in experiments on nanoparticles more than 50 years ago [63, 64] and has a large fraction of {111} facets but contains twin boundaries at the interface between each pair of tetrahedra, as well as a line defect where the five tetrahedra meet. In the context of Eq. (3.1), the twin boundaries and line defect will effectively increase the values of b and

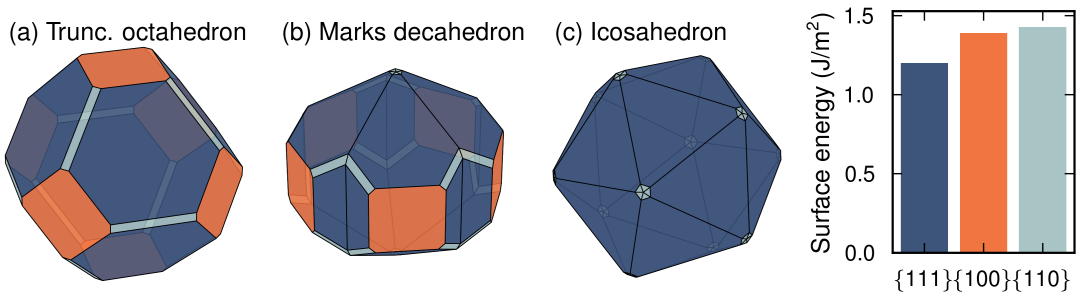

Figure 3.2: Nanoparticle shapes commonly adopted by FCC metals: (a) truncated octahedron, (b) Marks decahedron, and (c) icosahedron. The shapes are Wulff constructions that were created and visualized with WULFFPACK (Paper IV) based on surface energies of low-index facets of Au as calculated in Paper VII and plotted to the right.

c, respectively. Furthermore, a decahedron is always strained, because five equilateral tetrahedra do not completely fill space. It is worth noting that the generalized Wulff construction pictured in Fig. 3.2b is not convex; there are notches where the tetrahedra meet. Structures with such notches are commonly referred to as Marks decahedra [65].

3.3.3 Icosahedra

If twenty tetrahedra are stacked such that they meet in the center, they form an icosahedron (Fig. 3.2c), which, just as the decahedron, has more than 50 years of history in experiment [63, 64]. An icosahedron is quite spherical[1] but contains more twin boundaries and is even more strained than the decahedron. Just as for a decahedron, twenty equilateral tetrahedra do not fill space entirely, which causes strain. Geometry does, however, not require the strain to be uniform. In Paper V, icosahedral particles were observed to be compressed in the center but essentially free from strain close to the surface. It seems likely that this is simply the most energetically favorable way to fulfill the geometrical requirements. The tetrahedra have their tip in the center, and the number of atoms per shell increases in proportion to the distance from the center. If the height of the tetrahedron, i.e., the distance from its tip in the center to its face at the surface, is commensurate with the equilibrium lattice parameter, the lattice needs to be stretched about 5.1 % in the direction parallel to the surface. This would imply an approximately uniform strain in the particle. If, on the other hand, the length of the face of the tetrahedron is commensurate with the lattice parameter, then the particle must be compressed about 4.9 % in the radial direction. These 4.9 % may be unevenly distributed, and it should be favorable to compress the lattice primarily close to the center of the particle where the number of atoms per radial distance is the lowest.

[1]The classic football with hexagonal white and pentagonal black patches is in fact a truncated icosahedron (but it is recommended to inflate it properly to achieve an even more spherical shape).

3.3.4 Other shapes

In addition to the above described shapes, there are some structures that appear regularly. Particularly common among particles with less than a few hundred atoms are polyicosahedra, which are constructed by stacking smaller regular icosahedra [66, 67]. Another example is the rhombic dodecahedron, which emerges from a Wulff construction with a low {110} surface energy and thus is likely to occur among body-centered cubic (BCC) metals [54, 68]. Experimentalists also synthesize nanoparticles with a plethora of shapes and structures that are out of equilibrium, including rods, cages, stars and cubes [69–73]. Since this thesis focuses on equilibrium nanoparticles made of FCC metals with more than a hundred atoms, these shapes will not be discussed further.

3.3.5 Comparison of energetics

To compare the above mentioned shapes, we may construct a series of atomic structures with increasing number of atoms arranged in the target shape, calculate their energy, and fit Eq. (3.1) to each such series. We may then compare the fits and determine which shapes are stable in which size region (Fig. 3.3). Metals that adopt the FCC structure in the bulk generally exhibit the same trend; icosahedra are stable for the smallest sizes, Marks decahedra in an intermediate size regime, and truncated octahedra are stable for all sizes above a certain threshold. This trend is an immediate consequence of the scaling of the terms in Eq. (3.1). The first term dominates for large enough sizes, which destabilizes shapes that are strained, i.e., decahedra and icosahedra. For smaller sizes, the surface-to-volume ratio increases, making the second term increasingly important, favoring particles with a low overall surface energy. Since the icosahedron is more extreme than the decahedron in this sense, for small enough sizes the icosahedron will always be the most stable in this model. This trend is well-established and has been demonstrated by similar means in several publications [74–77].

3.4 Deficiencies of continuum models

Even though polynomial fits and Wulff constructions are powerful for making general predictions and explain trends, they are fundamentally continuum models and thus inherently unable to account for the finer details of the atomic scale. These include finite size effects pertaining to quantum mechanics, such as the distribution of charge around edges and corners, as well as volume-dependent strain fields caused by surface tension. Another important deficiency is a purely geometric one: a fixed number of atoms cannot form any shape. To create a RTO, for example, one needs 38, 201, 586 (etc.) atoms, and an icosahedron requires 55, 147, 309, 568 (etc.) atoms (marked with circles in Fig. 3.3). These atom counts are referred to as magic numbers. Any number of atoms that does

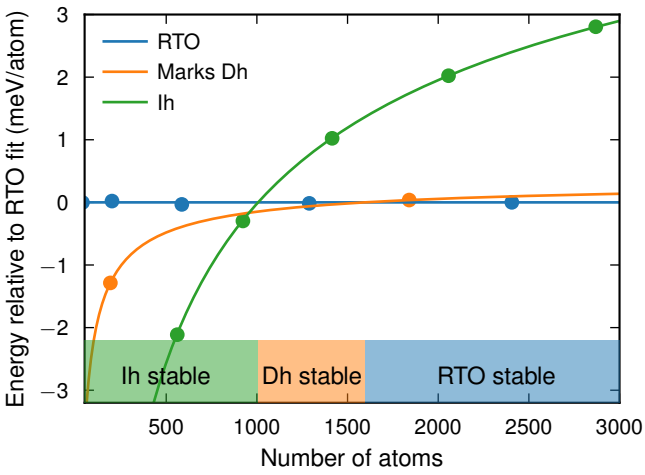

Figure 3.3: Energy per atom in magic number Cu nanoparticles fitted to a third degree polynomial in $N^{-1/3}$ where N is the number of atoms in the particle. The particles were relaxed in LAMMPS [78] with the EAM potential parametrized by Mishin *et al.* [79]. The color bars at the bottom indicate regions of stability, i.e., which shape has the lowest energy. Ih, Dh, and RTO denote icosahedron, decahedron and regular truncated octahedron, respectively.

not match a magic number will always form a shape that is not ideal, which could mean, for example, a non-equilateral hexagon, an elongated shape, a reconstructed surface, or any other defect. In any case, such a particle cannot be expected to be well described by a polynomial fit to magic number particles but will most likely have an energy higher than such a fit. This issue is addressed in Paper V. To improve the description of the energetics of nanoparticles, one is forced to abandon continuum models and calculate energies on the atomic scale. Atomic scale modeling is the subject of Chapter 5.

3.5 Chemical order in nanoalloys

By making nanoparticles with more than one chemical element—nanoalloys—the complexity increases significantly. All quantities become dependent on concentration, and even continuum models, such as the Wulff construction generalized to alloys [80], require great care because surface segregation may occur. In fact, an important difference between (ideal) bulk and nanoalloys is that while the former has at most a few crystallographically inequivalent sites, the latter has a wide range of sites with different local environments caused by surfaces and strain. Yet, the different possible chemical orderings in bulk alloys pervade nanoalloys as well; the mixing behavior in the bulk alloy is usually expected to be similar in the corresponding nanoalloy. The existence of a surface, a finite number of atoms, strain and possibly polycrystallinity as in a decahedron

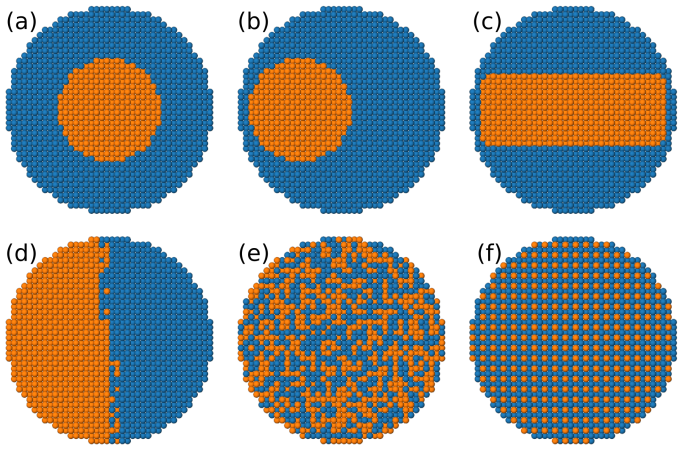

Figure 3.4: Nanoalloys with idealized chemical orderings: (a) core–shell, (b) off-center core–shell, (c) sandwich, (d) Janus, (e) random and (f) ordered.

or icosahedron do, however, allow for new behavior and modification of the ranges at which particular phases are stable. This has been demonstrated in computationally assessed phase diagrams for a wide range of nanoalloys, including Pt–Rh [81], Ag–Au [82], Ag–Cu [83], Au–Cu [84], and several Ni-based alloys [85]. It has also recently become possible to experimentally image the chemical order of nanoalloys atom by atom using atomic electron tomography [86]. Where models on the atomic scale would previously be compared indirectly to observations in the laboratory, there is now an exciting avenue to a level playground between theory and experiment.

Some nomenclature has emerged to systematize possible structures [87] (Fig. 3.4). The core–shell structure (Fig. 3.4a) is particularly ubiquitous, partly because it is possible to synthesize for a wide range of alloys, including alloys that would mix in thermodynamic equilibrium. A core–shell structure can for example be of economic interest for an application where the element at the surface of the particle is important but expensive and can be filled with a cheaper element in the core. Computational studies show that the core is often asymmetrically positioned in equilibrium [88] (Fig. 3.4b). The investigation of Ag–Cu in Paper VI further indicates that the notion of a core is in some structures merely a special case of a more complex segregation pattern, which at some compositions may lead to a ring-like sandwich pattern (Fig. 3.4c). The shape of the segregate is thus largely dictated by the underlying structure of the particle. So-called Janus particles, where the elements segregate at either side of the particle (Fig. 3.4d), are attractive for some applications primarily because they are inherently anisotropic [89]. Randomly mixed nanoalloys (Fig. 3.4e) and nanoalloys with long-range order (Fig. 3.4e) are often desirable for applications in catalysis, where there can be synergistic effects from the two elements [90]. There are of course many more possibilities than the highly idealized structures described here, and some of them are illustrated in Paper VI.

3.6 Ensembles of nanoparticles

Nanoparticles never walk alone; a laboratory making one nanoparticle at a time would hardly make a profitable business. It is useful to think of a solution of nanoparticles as an *ensemble* of nanoparticles. Such ensembles are directly related to ensembles as described by statistical mechanics, i.e., large sets of copies of the system in different states. Unlike the virtual copies of a statistical mechanics ensemble, the nanoparticles in such a system interact by heat exchange with the solvent, but if the solvent is voluminous enough to have an essentially infinite heat capacity, this interaction is merely indirect. A dilute solution of nanoparticles is then well approximated by a canonical ensemble for which the solvent is the heat reservoir. A seemingly trivial but important consequence is that if we calculate, say, that the probability in the canonical ensemble for a certain nanoparticle to be an icosahedron is 30 %, a solution with 100 such particles should have on average 30 icosahedra.

In a similar fashion, we can imagine a solution of nanoparticles that may exchange both energy and atoms with the solution. Even though atoms would be exchanged between particles, each particle may be considered an independent system interacting with a reservoir of heat and single atoms. The corresponding ensemble is referred to as grand canonical, and the probability for a particular state s for a single particle is calculated as

$$P(s) = \frac{e^{-(\epsilon_s - \mu N)/k_\mathrm{B}T}}{\mathcal{Z}}, \tag{3.9}$$

where μ is the chemical potential of the atoms that are being supplied from the solution, N is the number of atoms in the particle and $\mathcal{Z}$ is the partition function in the grand canonical ensemble (a sum over all states of terms such as the one in the numerator).

In practice, an equilibrium solution of metallic nanoparticles that exchange atoms with the solution may be difficult to realize in an experiment, because the atoms are generally much too strongly bound to be released to the solution. The experimental problem is rather the opposite, that nanoparticles tend to cluster into bigger entities, a phenomenon usually prevented by stabilizing organic molecules on the surface of the particles. The atom count for each particle is to a large extent established during growth, when the particles assemble atoms from a solution of a metal salt and a reducing agent. This process is predominantly kinetically driven and can usually only be understood partially from an equilibrium perspective. The result is always that the particle ensemble is more or less polydisperse, i.e., the particles have different numbers of atoms, but the size distribution is, as a manifestation of the central limit theorem, usually well described by a normal distribution regardless of synthesis route.

Given the impact of atomic-scale details and the existence of magic numbers (as discussed in Sect. 3.4), polydisperse and monodisperse ensembles may differ significantly. In other words, it may be important to consider the whole distribution of sizes in a polydisperse ensemble and not just the average size. In Paper V, we assumed a normal dis-

tribution $f(n, N)$ of atom counts n with average atom count N. For each atom count, we then assumed a Boltzmann distribution of shapes, such that the probability of a shape s_0 is

$$P_n(s_0) = \frac{\exp\left(-\epsilon_{n,s_0}/k_\mathrm{B}T\right)}{\sum_{s_i}\exp\left(-\epsilon_{n,s_i}/k_\mathrm{B}T\right)}, \tag{3.10}$$

where ϵ_{n,s_i} is the lowest energy of any particle with n atoms in structural motif s_i. The probability for a particular shape for an ensemble with average size N was then calculated as

$$P_N(s_0) = \frac{1}{M}\sum_n f(n, N)P_n(s_0) \tag{3.11}$$

where M ensures that the probabilities sum up to 1. Fed with the results from the algorithm of Paper V, this model indicates that there is a distribution of structural motifs in thermodynamic equilibrium. The model assumes that energetics does not affect the distribution of atom counts; it is not more probable to have a particle with 923 atoms just because it is an icosahedral magic number. This may or may not be a valid assumption, depending on the growth protocol. It is perhaps more questionable that only the ground states for three structural motifs were taken into account, and all with the same multiplicity. Whereas inclusion of more structural motifs with higher energy could only strengthen the conclusion that there is a distribution of shapes in thermodynamic equilibrium, it cannot be ruled out that an account for multiplicity could have the opposite effect. Furthermore, elevated temperatures, which are assumed in the Boltzmann factors of Eq. (3.10), may favor some structural motifs over the others, primarily due to vibrations. This has been demonstrated in the case of Au, for which decahedral particles were seen to be stabilized by temperature relative to the other structural motifs [76].

It should be stressed that the energy entering Eq. (3.10) should be the total energy of the nanoparticle, not the energy per atom as occasionally encountered in the literature. This is perhaps easiest realized if we let the nanoparticle grow towards the thermodynamic limit. We could still apply the same formula to, for example, predict the probability of finding the material in one of two crystal structures, but if we plug in energy per atom the conclusion would be that both crystal structures can be anticipated (unless the energy differs by a lot), contrary to our knowledge about equilibrium in the thermodynamic limit. If the energy per atom is erroneously used in the nanoparticle case, different structural motifs would appear more competitive than they actually are. The primary reason for our conclusion that there is a distribution of structural motifs in thermodynamic equilibrium, is that different structural motifs are the most stable at different atom counts. A perfectly monodisperse ensemble, with only one nanoparticle atom count, would in equilibrium typically *not* contain different structural motifs.

4

Optical properties of metals and nanoparticles

If we lived our lives in a nanoscale world, the word "golden" to describe color would have been quite confusing. When the length scale of objects are shrunk towards the wavelength of visible light, their optical properties are dramatically changed, and solutions of gold nanoparticles can appear red or blue. Even on the nanoscale, most optical properties can be predicted with the use of dielectric functions, which on a macroscopic scale describe the response of materials to an applied electric field (such as light). This chapter approaches dielectric functions from both a classical and a quantum mechanical perspective, and describes how their properties relate to the optical response of metallic nanoparticles.

4.1 The dielectric function from a classical perspective

Consider a free-electron bulk system (an approximation for metallic behavior) subject to an external electric field $\boldsymbol{E}_{\text{ext}}$. Since the electrons are free, they will rearrange so as to counteract the external electric field by producing an electric field $\boldsymbol{E}_1$ of their own. This field is usually expressed in terms of a polarization, $\boldsymbol{E}_1 = -\boldsymbol{P}/\epsilon_0$, where ϵ_0 is the permittivity of free space. If the electrons are truly free, the polarization $\boldsymbol{P}$ will be such that $\boldsymbol{E}_1$ completely cancels $\boldsymbol{E}_{\text{ext}}$ inside the material. This, however, is only possible if $\boldsymbol{E}_{\text{ext}}$ does not vary too quickly in time, in which case, simply put, damping and inertia of the electrons will lead to a lag in the response.

To better understand the dynamics, we can introduce a classical model by writing the equation of motion for the electrons,

$$m\ddot{\boldsymbol{x}} + \gamma m\dot{\boldsymbol{x}} = -e\boldsymbol{E}. \tag{4.1}$$

Here, $\boldsymbol{x}$ is the displacement of the electrons, m the mass of the electron, γ a damping factor, e the elementary charge and $\boldsymbol{E}$ the total electric field, i.e., $\boldsymbol{E} = \boldsymbol{E}_{\text{ext}} + \boldsymbol{E}_1$. This equation is easily solved by entering Fourier space,

$$\boldsymbol{x}(\omega) = \frac{e/m}{\omega^2 + i\gamma\omega}\boldsymbol{E}(\omega). \tag{4.2}$$

Polarization is given by the product of charge and displacement, so with a charge density n we obtain

$$\boldsymbol{P}(\omega) = -ne\boldsymbol{x} = -\frac{ne^2/m}{\omega^2 + i\gamma\omega}\boldsymbol{E}(\omega). \tag{4.3}$$

We have thus arrived at a relation between the polarization and the electric field. This relation is often expressed in terms of the dielectric function $\epsilon(\omega)$, which can be defined by

$$\boldsymbol{P}(\omega) = \epsilon_0(\epsilon(\omega) - 1)\boldsymbol{E}(\omega) \tag{4.4}$$

and by comparison to Eq. (4.3) we identify

$$\epsilon(\omega) = 1 - \frac{\omega_p^2}{\omega^2 + i\gamma\omega}, \tag{4.5}$$

where we have introduced the plasma frequency $\omega_p = \sqrt{ne^2/m\epsilon_0}$. Equation (4.5) is sometimes called the Drude dielectric function. Its real and imaginary parts are given by

$$\operatorname{Re}\epsilon(\omega) = 1 - \frac{\omega_p^2\omega^2}{\omega^4 + \gamma^2\omega^2} \quad \text{and} \quad \operatorname{Im}\epsilon(\omega) = \frac{\omega_p^2\omega\gamma}{\omega^4 + \gamma^2\omega^2}, \tag{4.6}$$

which are plotted in Fig. 4.1a.

From Eq. (4.4) it is clear that the dielectric function is an important quantity; it describes the response of a material to an electric field and thus governs the propagation of light in presence of this material. Let us now examine the general behavior of the Drude dielectric function. Both the real and the imaginary part diverge at $\omega = 0$. This is the expected behavior for a free-electron system, which is "infinitely flexible" in the static limit. For finite frequencies, the real part is monotonically increasing and negative for sufficiently small frequencies ω. If γ is small, $\operatorname{Re}\epsilon(\omega)$ becomes positive at $\omega > \omega_p$. In terms of wave propagation, this means the medium becomes transparent to electric fields with a frequency higher than the plasma frequency. The positive imaginary part indicates that energy is absorbed through damping of the waves, but since the imaginary part of $\epsilon(\omega)$ is monotonically decreasing, this absorption decreases with frequency as well.

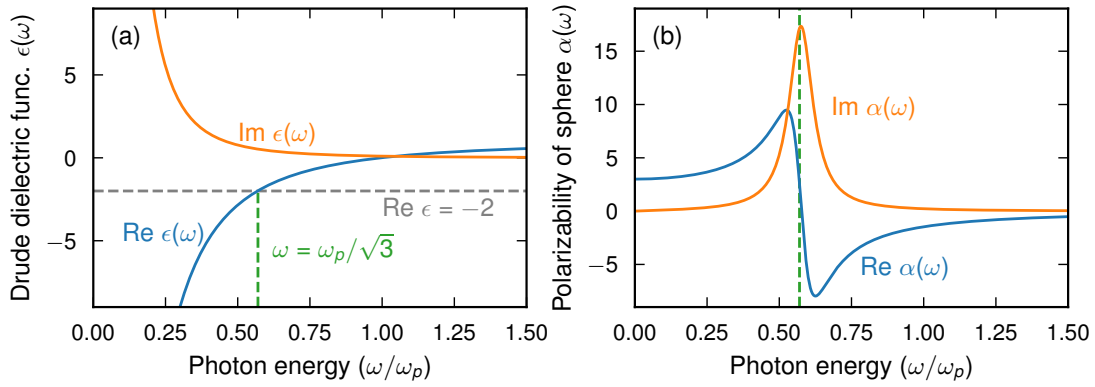

Figure 4.1: (a) Drude dielectric function with $\gamma = 0.1\omega_p$, with real part in blue and imaginary in orange. The Fröhlich condition ($\mathrm{Re}\,\epsilon(\omega) = -2$, grey line) is fulfilled at $\omega = \omega_p/\sqrt{3}$ (green line). (b) The corresponding polarizability of a small sphere exhibits a resonance at $\omega = \omega_p/\sqrt{3}$, manifested by a peak in the imaginary part.

4.2 Localized surface plasmon resonance

In the derivation in the preceding section we assumed that the electrons resided in bulk matter. What changes if we instead confine the electrons to a sphere? The equation of motion for the electrons will still be Eq. (4.1), but the difference is the induced field (depicted in Fig. 4.2a). The displacement $\boldsymbol{x}$ of the electrons will effectively create a surface charge of the form $\sigma = e\boldsymbol{x}\cdot\hat{\boldsymbol{n}}$, where $\hat{\boldsymbol{n}}$ is the direction of the applied field. Such a surface charge creates a uniform field inside the sphere [91, Chapter 4],

$$\boldsymbol{E}_1 = \frac{ne}{3\epsilon_0}\boldsymbol{x}, \tag{4.7}$$

while outside the sphere, the field will be identical to that from a dipole located at the center of the sphere with dipole moment

$$\boldsymbol{p} = -Vne\boldsymbol{x}. \tag{4.8}$$

We can now write an alternative version of Eq. (4.1) using our explicit expression for $\boldsymbol{E}_1$,

$$m\ddot{\boldsymbol{x}} + \gamma m\dot{\boldsymbol{x}} = -e\left(\boldsymbol{E}_{\text{ext}} + \frac{ne}{3\epsilon_0}\boldsymbol{x}\right), \tag{4.9}$$

which in Fourier space yields

$$\boldsymbol{x}(\omega) = \frac{e/m}{\omega^2 - \omega_p^2/3 + i\gamma\omega}\boldsymbol{E}_{\text{ext}}(\omega). \tag{4.10}$$

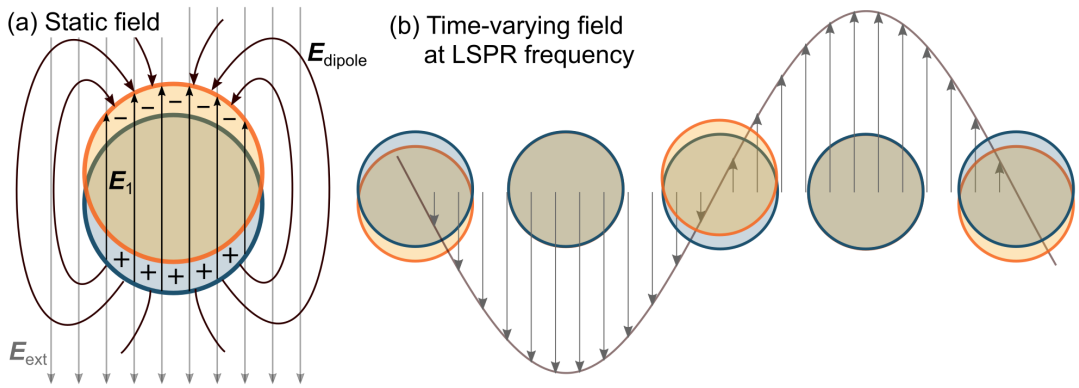

Figure 4.2: Schematic of the response from a conducting sphere to (a) a static and (b) a time-varying field. The electron cloud is depicted as an orange circle, the positive background as a blue circle. (a) The static external field $\boldsymbol{E}_{\text{ext}}$ induces a displacement of the electron cloud that creates a field $\boldsymbol{E}_1$, which cancels $\boldsymbol{E}_{\text{ext}}$ inside the sphere. Outside the sphere, the field is identical to the field from a dipole at the center of the sphere. (b) The electron cloud oscillates in response to a time-varying field, and at the LSPR frequency, there is a $\pi/2$ phase shift between the external field and the response.

Here, we have assumed that the electric field is homogeneous over the sphere at every instant, i.e., the particle is small compared to the wavelength (the so-called quasistatic limit). The proportionality coefficient between dipole moment and external field is called the polarizability, and by comparison with Eq. (4.8), we see that the polarizability is given by

$$\alpha(\omega) = \frac{\boldsymbol{p}(\omega)}{\boldsymbol{E}_{\text{ext}}(\omega)} = -V\epsilon_0 \frac{\omega_p^2}{\omega^2 - \omega_p^2/3 + i\gamma\omega}. \tag{4.11}$$

We can already at this point note that for small values of γ, there is a resonance at $\omega = \omega_p/\sqrt{3}$; a small electric field will trigger a large response (Fig. 4.1b and Fig. 4.2b). With a little bit of algebra, we can rewrite Eq. (4.11) in terms of the Drude dielectric function (Eq. (4.5)),

$$\alpha(\omega) = 3\epsilon_0 V \frac{\epsilon(\omega) - 1}{\epsilon(\omega) + 2}. \tag{4.12}$$

Unlike Eq. (4.11), this result is not specific for the simple derivation here but is general for spherical particles in vacuum in the quasistatic limit [92, Capter 5]. The polarizability has a resonance, referred to as localized surface plasmon resonance (LSPR), at the frequency ω that fulfills

$$\operatorname{Re}\epsilon(\omega) = -2, \tag{4.13}$$

provided $\operatorname{Im}\epsilon(\omega)$ is small or does not vary too quickly. This is referred to as the Fröhlich condition. Quantum mechanically, this resonance can be regarded as a collective oscillation of electrons that is quantized: a localized surface plasmon.

4.2.1 Absorption and scattering

The absorption and scattering by a nanoparticle is directly related to the polarizability. Specifically, the absorption cross section is proportional to the imaginary part [92],

$$\sigma_{\text{absorption}}(\omega) = \frac{\omega}{\epsilon_0 c} \operatorname{Im} \alpha(\omega), \tag{4.14}$$

(c is the speed of light) whereas the scattering cross section is proportional to the square of the polarizability,

$$\sigma_{\text{scattering}}(\omega) = \frac{1}{6\pi\epsilon_0^2} \left(\frac{\omega}{c}\right)^4 |\alpha(\omega)|^2. \tag{4.15}$$

Extinction is the sum of absorption and scattering. Since $\alpha(\omega)$ is proportional to the volume of the particle, absorption will also scale with volume, whereas scattering scales with volume squared. Extinction is therefore dominated by absorption for small particles and scattering for large particles.

4.2.2 Ellipsoidal particles

The extinction spectrum from a spherical nanoparticle is not guaranteed to contain a sharp peak where the Fröhlich condition (Eq. (4.13)) is met, because the resonance can be drowned by a large imaginary part. By making the particle non-spherical, however, the resonance condition can be tuned. It is, for example, possible to move the resonance to a frequency where the imaginary part of the dielectric function is small, and the LSPR peak in the extinction spectrum will then be much sharper. Using ellipsoidal coordinates, one can show [92, Chapter 5] that for an ellipsoid with principal axes a_i ($i = 1, 2, 3$) the polarizability in direction i is given by

$$\alpha_i(\omega) = 3\epsilon_0 V \frac{\epsilon(\omega) - 1}{L_i\left[\epsilon(\omega) - 1\right] + 3}, \tag{4.16}$$

meaning the condition for resonance reads

$$\operatorname{Re} \epsilon(\omega) = -3/L_i + 1, \tag{4.17}$$

where L_i is real and depends on geometry,

$$L_i = \frac{3}{2} a_1 a_2 a_3 \int_0^\infty \frac{\mathrm{d}q}{\left(q + a_i^2\right)\sqrt{\left(q + a_1^2\right)\left(q + a_2^2\right)\left(q + a_3^2\right)}}. \tag{4.18}$$

For a sphere, all axes are equal ($a_1 = a_2 = a_3$) and $L_1 = L_2 = L_3 = 1$, and we recover Eq. (4.11). For an ellipsoid, L_i is different in different directions, and in the direction

of the longest (shortest) semi-axis, L_i is smaller (greater) than 1. If the real part of the dielectric function is monotonically increasing (as in the Drude dielectric function), this means the resonance will be shifted to lower energies along the long axis and higher energies along the short axis. This is intuitively sound, since lower energies correspond to longer wavelengths.

4.3 Impact of bound electrons

The derivation of the Drude dielectric function in Sect. 4.1 assumed that the electrons of the material were free to move around at will. This assumption works well for some simple metals such as Na [93] but not necessarily for materials with a richer electronic structure, for which the free electron model is less well suited. To treat these electrons classically, we could write a similar equation of motion as Eq. (4.1) but include an additional restoring force, $-K\boldsymbol{x}$, that would cause a resonance at nonzero frequencies. The dielectric function of the material would then be the sum of a Drude-like function and functions with resonances at nonzero frequencies. In metals, these resonances are typically broadened and modified by the details of the electronic structure to such an extent that their effect on the dielectric function is indistinguishable from this classical model, but their most easily recognizable impact is an increase in the imaginary part of the dielectric function at frequencies where bound electrons can be excited. We will return to these aspects in Sect. 4.4.1.

4.4 The dielectric function from linear-response theory

To go beyond the classical description of an electron moving in an electric field, we need to approach the dielectric function from a more fundamental direction. The most important results from linear-response theory combined with quantum mechanics will be stated here. Let us view the incoming light as an external time-dependent potential, $v_{\text{ext}}(\boldsymbol{r}, t)$. This perturbation induces a response in the electron density, $n_1(\boldsymbol{r}, t)$. If we assume that v_{ext} is small, it suffices to study the first-order effects. We can then write the following connection between the first-order density response and the perturbation:

$$n_1(\boldsymbol{r}, t) = \int \mathrm{d}t' \int \mathrm{d}^3 r' \, \chi(\boldsymbol{r}, \boldsymbol{r}', t - t') v_{\text{ext}}(\boldsymbol{r}', t'). \tag{4.19}$$

Here, χ is the density–density response function, which is given by the Kubo formula as

$$\chi(\boldsymbol{r}, \boldsymbol{r}', t - t') = -i\theta(t - t') \, \langle \Psi_0 | [\hat{n}(\boldsymbol{r}, t - t'), \hat{n}(\boldsymbol{r}')] | \Psi_0 \rangle \,, \tag{4.20}$$

where $\theta(t-t')$ is the Heaviside step function, $|\Psi_0\rangle$ the ground state wave function, and $\hat{n}$ the density operator. Equation (4.19) suggests that these expressions are simpler in Fourier space,

$$n_1(\boldsymbol{r},\omega) = \int \mathrm{d}^3 r' \chi(\boldsymbol{r},\boldsymbol{r}',\omega) v_{\mathrm{ext}}(\boldsymbol{r}',\omega) \tag{4.21}$$

and the response function, with the use of the completeness relation for $|\Psi_n\rangle$ and the integral representation of $\theta(t-t')$, can be written in the so-called Lehmann representation [94, Chapter 7],

$$\chi(\boldsymbol{r},\boldsymbol{r}',\omega) = \sum_{n=1}^{\infty} \left(\frac{\langle\Psi_0|\hat{n}(\boldsymbol{r})|\Psi_n\rangle\langle\Psi_n|\hat{n}(\boldsymbol{r}')|\Psi_0\rangle}{\omega-\Omega_n+i\eta} - \frac{\langle\Psi_0|\hat{n}(\boldsymbol{r}')|\Psi_n\rangle\langle\Psi_n|\hat{n}(\boldsymbol{r})|\Psi_0\rangle}{\omega+\Omega_n+i\eta} \right), \tag{4.22}$$

where $\Omega_n = \omega_n - \omega_0$, i.e., the excitation energy of the n-th excited state (we are using $\hbar = 1$ here). This form is in itself of little use to calculate the response, because it requires knowledge of the many-body eigenstates $|\Psi_n\rangle$ to the Hamiltonian. Nevertheless, it highlights that the response is the strongest when the frequency of the light matches the excitation energies Ω_n.

For periodic systems, it is advantageous to enter reciprocal space by Fourier transform,

$$\chi(\boldsymbol{r},\boldsymbol{r}',\omega) = \frac{1}{V} \sum_{\boldsymbol{k}\in 1\mathrm{BZ}} \sum_{\boldsymbol{G},\boldsymbol{G}'} e^{-i(\boldsymbol{k}+\boldsymbol{G})\cdot\boldsymbol{r}} e^{i(\boldsymbol{k}+\boldsymbol{G}')\cdot\boldsymbol{r}'} \chi_{\boldsymbol{G}\boldsymbol{G}'}(\boldsymbol{k},\omega), \tag{4.23}$$

where V is the crystal volume, and the first sum runs over all points in the first Brillouin zone (BZ) and the second over all pairs of reciprocal lattice vectors $\boldsymbol{G}$ (the notation $\chi_{\boldsymbol{G}\boldsymbol{G}'}(\boldsymbol{k},\omega)$ is shorthand for $\chi(\boldsymbol{k}+\boldsymbol{G},\boldsymbol{k}+\boldsymbol{G}',\omega)$). It can be shown that the macroscopic dielectric function in the optical limit is given by [94, Chapter 12]

$$\epsilon(\omega) = \lim_{\boldsymbol{k}\to 0} \left[1 + \frac{4\pi}{k^2} \chi_{00}(\boldsymbol{k},\omega) \right]^{-1}. \tag{4.24}$$

This quantity is calculated in Paper VIII, and Sect. 5.2 outlines a method for getting there without the arduous Eq. (4.22).

4.4.1 Connection to band structure

The connection between excitation energies and the response function as established in Eq. (4.22), makes a closer inspection of electronic band structures worthwhile, since they reveal which elementary excitations are possible. The dominant type of excitations are vertical (i.e., they involve no change in momentum $\boldsymbol{k}$) from below the Fermi level to above. Metals are characterized by the lack of a band gap; at least one band crosses the Fermi level. This means excitations with infinitesimally small energies are possible, which gives rise to the singularity at $\omega = 0$ seen also in the Drude dielectric function

and often referred to as the Drude peak. Such excitations that occur within a band are referred to as intraband transitions. At higher energies, bands below the Fermi level start to play a role. For late transition metals, such as Pd and Au, the d electrons are particularly important. In Pd (Fig. 4.3a), the d-electron bands lie just below the Fermi level, and even cross it in some parts of the Brillouin zone. This effectively makes the Drude peak very wide (Fig. 4.3c). For Au (Fig. 4.3b), on the other hand, the d states lie approximately 2 eV below the Fermi level. Consequently, the Drude peak dies off and the imaginary part of the dielectric function becomes very small, before it increases again due to the onset of interband transitions from the d band to the s and p bands (Fig. 4.3d).

The behavior of the dielectric function, and in particular the impact of interband transitions, has major consequences for optical absorption of nanoparticles. In both Pd and Au, the Fröhlich condition (Eq. (4.13)) is fulfilled at a frequency where the imaginary part of the dielectric function is substantial. The corresponding absorption spectrum of a Pd sphere in the quasistatic limit (Fig. 4.3e, green line) has a very wide peak located approximately 1 eV above the Fröhlich condition. In Au (Fig. 4.3f), there is hardly any peak at all. By using an oblate ellipsoid (two equally long axes and one short), however, a different picture emerges. For Pd, the change is primarily a shift to lower frequencies, but the peak is still wide. For Au, on the other hand, a very sharp LSPR forms, in sharp contrast to the featureless absorption spectrum of the sphere. The reason is that the resonance condition (Eq. (4.17)) is now fulfilled at a lower frequency, just below the onset of interband transitions from the d band to the s and p bands. At this frequency, the imaginary part of the dielectric function is very low, which allows for a sharp peak. It is worth noting that it is only in the case of the sharp Au peak that the absorption maximum coincides with the resonance condition. These observations demonstrate that the resonance conditions can be misleading when ignoring the underlying assumptions, namely that the imaginary part of the dielectric function should be small or very slowly varying (almost constant).

For late transition metal alloys, the band structure essentially turns out to be an interpolation of the band structures of the constituents (Fig. 4.4). This interpolation is, however, not necessarily linear. Fig. 4.4 indicates that upon addition of 25% Au to Pd, the d band is in almost the same position with respect to the Fermi level as in pure Pd. It is only when the concentration of Au reaches 50% that the distance between d band and Fermi level starts to increase quickly. To understand this non-linearity, we may approximate the band structure as unaffected by alloying (the rigid band model [95]), with the only change upon alloying being a shift of the Fermi level due to the additional valence electron in Au. This valence electron occupies the states closest to the Fermi level, which gradually pushes the Fermi level up. Since the density of states close to the Fermi level is very high in pure Pd, this shift in the Fermi level is first very slow, and it is only when these states are filled that the shift occurs more quickly. The shift is thus slow for low Au content and fast for high Au content, as observed in Fig. 4.4. This explanation is of course only schematic, given that the band structure is not entirely rigid. The non-

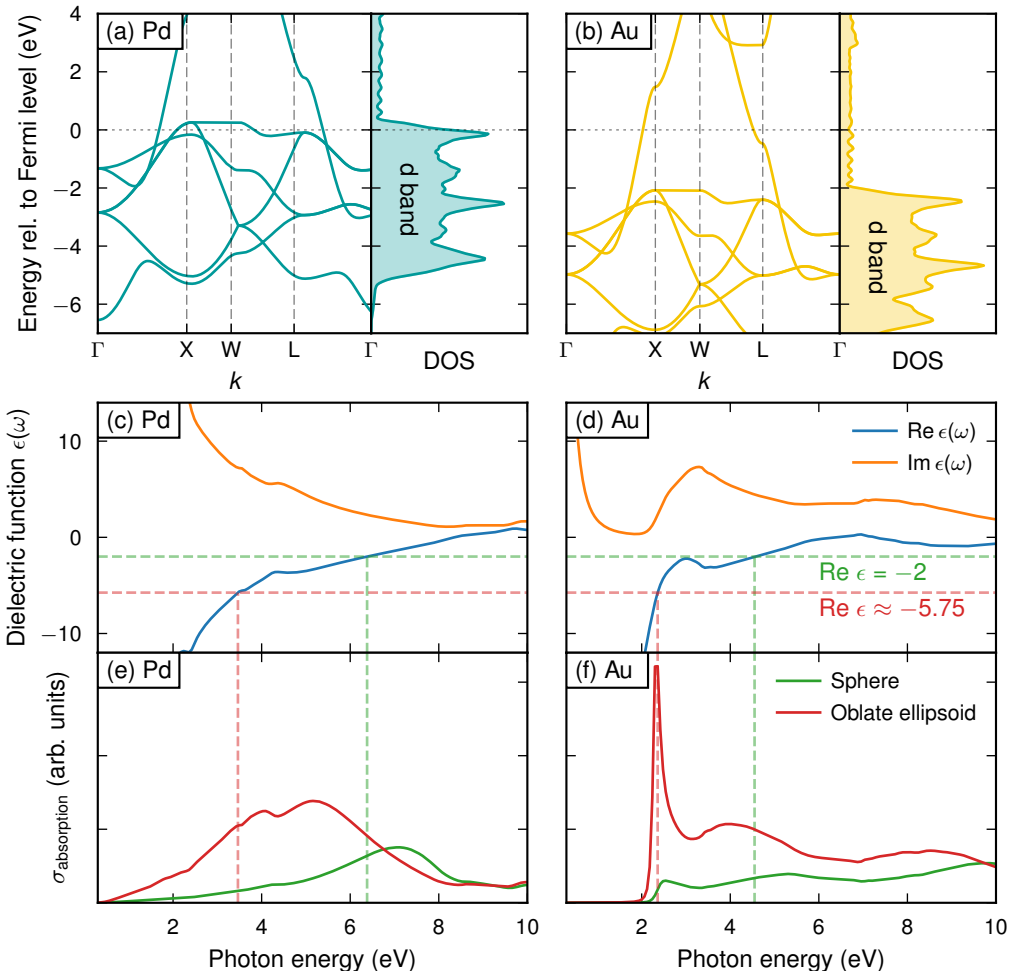

Figure 4.3: Electronic and optical properties of Pd (left) and Au (right), calculated within the scope of Paper VIII. (a–b) The band structures of Pd and Au are similar but the Fermi level is shifted such that the d band lies at the edge of the Fermi level in Pd but about 2 eV below it in Au. This is particularly clear in the density of states (right), where the d band is manifested by a high density. (c–d) The dielectric functions of Pd and Au differ significantly. While for Pd the imaginary part (orange line) is large and featureless, for Au it dips between roughly 1 and 2 eV before it increases again due to the onset of interband transitions. (e–f) The corresponding optical absorption of spherical nanoparticles (green) and along the long axis of oblate ellipsoids with aspect ratio 4 (red) in the quasistatic limit differ vastly. For Pd, the peaks are very wide, while for spherical Au, there is hardly any peak at all. A sharp LSPR peak forms only in the Au ellipsoid, because the resonance condition for the oblate shape (Eq. (4.17), horizontal, red line in (d)) has shifted the resonance frequency to a lower energy, just below the onset of interband transitions. Note that when the imaginary part is large (and not constant), the Fröhlich condition (Eq. (4.13), green, dashed lines) and its generalization (Eq. (4.17), red, dashed lines) do not give accurate estimates of where a peak forms.

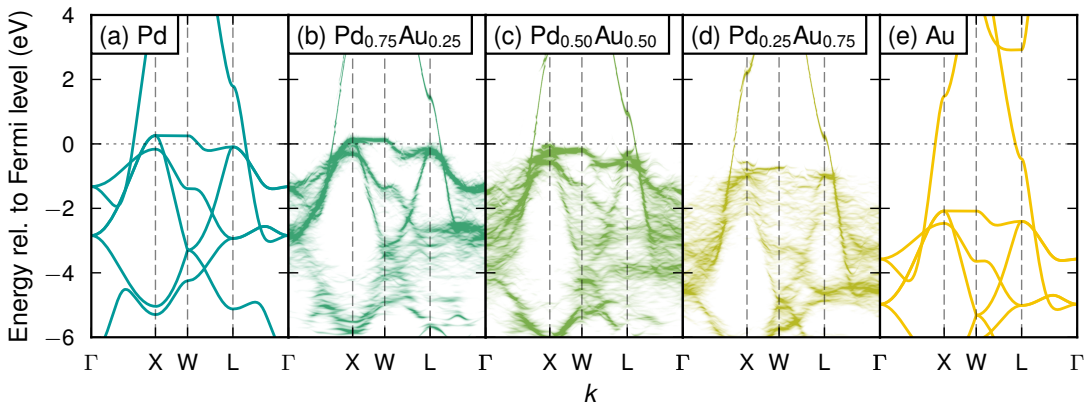

Figure 4.4: Electronic band structure of (a) Pd, (b) $Pd_{0.75}Au_{0.25}$, (c) $Pd_{0.5}Au_{0.5}$, (d) $Pd_{0.25}Au_{0.75}$, and (e) Au. The energy scale has been shifted to align the Fermi levels (dotted, grey line). For the alloys, the band structures are calculated by unfolding the band structures [98] of the reciprocal cell of 24 atoms large special quasirandom supercells (Sect. 5.5) as calculated using the GPAW software [99, 100] within the scope of Paper VIII. Note that the distance between the Fermi level and the d band monotonically but non-linearly increases when approaching pure Au.

linear trend does, however, hold in general for the non-isovalent systems discussed in Paper VIII. Non-linearities are of particular interest since they increase the probability of finding a material that is more than the sum of its parts [96].

Finally, a glaring difference between the band structures of pure and alloyed systems in Fig. 4.4 needs to be addressed. The sharp, well-defined bands of the pure systems result from an ideal crystal. In alloys, the bands are blurred unless there is perfect long-range order. In real systems, this difference is not as significant as Fig. 4.4 suggests, because the bands of a pure system are in practice more or less blurred too, due to vibrations and defects. Yet, the less well-defined bands of alloys may still have appreciable consequences on the macroscale, such as a higher resistivity compared to the pure systems [97, Chapter 22].

5 Computational methods

In a world of infinite computational power and memory, it would perhaps have been sufficient to state the Schrödinger equation here and then move on. Unfortunately (or luckily for us who enjoy the art of the method development), the complexity of many-body problems in physics requires sophisticated methods that are adapted to the time and length scales relevant to the problem at hand. This chapter describes the computational methods employed in this thesis, starting on the electronic scale and working its way to atomic scale modeling of systems with hundreds or thousands of atoms. The emphasis is on the most central aspects, and the reader is referred to the references stated for rigorous theory or details of implementation.

5.1 Density-functional theory

DFT is a framework for solving the Schrödinger equation

$$\hat{H}\Psi_J = E_J\Psi_J \tag{5.1}$$

for a system of interacting electrons. Specifically, the problem is cast in terms of the electron density instead of the wave function, which dramatically reduces the complexity. This is justified by the Hohenberg–Kohn theorems [101], which state that the external potential is a unique functional of the electron density, and that the electron density that minimizes the energy is the exact electron density, i.e., it can be obtained variationally. Since the external potential is a functional of the density, the full Hamiltonian is also given by the density, and thereby all properties of the system. These facts are exploited in the Kohn–Sham approach [102], which casts the many-body problem as a

system of non-interacting particles subject to an effective potential[1],

$$\left(-\frac{\nabla^2}{2} + v(\boldsymbol{r}) + \int \frac{n(\boldsymbol{r}')}{|\boldsymbol{r}-\boldsymbol{r}'|}\,\mathrm{d}\boldsymbol{r}' + v_{\mathrm{xc}}(\boldsymbol{r})\right)\varphi_j(\boldsymbol{r}) = \varepsilon_i\varphi_j(\boldsymbol{r}). \tag{5.2}$$

Here, the first term in the parenthesis represents the kinetic energy, the second the external potential (due to the ions), the third an effective Coulomb interaction between the electrons (the Hartree term), and the fourth is referred to as exchange–correlation and collects everything not captured by the other terms. The success of DFT hinges on a proper approximation of the exchange–correlation term, which is itself a functional of the electron density. With the exact exchange–correlation functional (which is unknown) the density of the interacting system is recovered as a sum over the occupied orbitals of the non-interacting system,

$$n(\boldsymbol{r}) = \sum_j |\varphi_j(\boldsymbol{r})|^2. \tag{5.3}$$

5.2 Linear-response time-dependent density-functional theory

The Hohenberg–Kohn theorems have a time-dependent equivalent, the Runge–Gross theorem [103], which states that a time-dependent external potential is a functional of the corresponding time-dependent electron density (up to a time-dependent but spatially homogeneous constant). This provides the fundamental basis for extending DFT to time-dependent phenomena and excited states. In particular, time-dependent density-functional theory (TDDFT) can be used to calculate dielectric functions using the linear-response formalism outlined in Sect. 4.4. To this end, the first step is to rewrite the induced density in terms of a non-interacting response function [104],

$$n_1(\boldsymbol{r},t) = \int \mathrm{d}t' \int \mathrm{d}^3r'\,\chi_s(\boldsymbol{r},\boldsymbol{r}',t-t')v_s(\boldsymbol{r}',t'). \tag{5.4}$$

Here, χ_s is the response function of the non-interacting system and v_s is the time-dependent equivalent of the potential terms in the left-hand side of Eq. (5.2). The Lehmann representation of the non-interacting response function, unlike the response function of the interacting system, can be readily evaluated and is given in terms of the single-particle orbitals as obtained in the Kohn–Sham approach of (ground-state) DFT [94, Chapter 7],

$$\chi_s(\boldsymbol{r},\boldsymbol{r}',\omega) = \sum_{i,j=1}^{\infty}(f_j - f_i)\frac{\varphi_i(\boldsymbol{r})\varphi_j^*(\boldsymbol{r})\varphi_i^*(\boldsymbol{r}')\varphi_j(\boldsymbol{r}')}{\omega - (\varepsilon_i - \varepsilon_j) + i\eta}, \tag{5.5}$$

[1] Atomic units will be used here.

where f_i is the occupation of orbital i. By equating the right-hand sides of the interacting (Eq. (4.19)) and the non-interacting (Eq. (5.4)) response equations, a Dyson-like equation can be obtained [94, Chapter 12],

$$\chi(\boldsymbol{r},\boldsymbol{r}',\omega) = \chi_s(\boldsymbol{r},\boldsymbol{r}',\omega) + \int \mathrm{d}^3 r_1 \int \mathrm{d}^3 r_2 \, \chi_s(\boldsymbol{r},\boldsymbol{r}_1,\omega)\left[\frac{1}{|\boldsymbol{r}_1-\boldsymbol{r}_2|} + f_{\mathrm{xc}}(\boldsymbol{r}_1,\boldsymbol{r}_2,\omega)\right]\chi(\boldsymbol{r}_2,\boldsymbol{r}',\omega), \tag{5.6}$$

where $f_{\mathrm{xc}}(\boldsymbol{r}_1,\boldsymbol{r}_2,\omega)$ is the exchange–correlation kernel, a functional of the ground state density. The dielectric function can thus be calculated by (1) making a ground-state DFT calculation, (2) evaluating the non-interacting response function (Eq. (5.5)), (3) solving Eq. (5.6) for χ, and (4) transforming χ to the dielectric function using Eq. (4.24). For periodic systems, the full calculation is done in reciprocal space. In Paper VIII we used the GPAW implementation [105] of this scheme to calculate the dielectric functions of binary alloys.

5.3 Empirical potentials

Even if DFT is a massive improvement over any attempt to solve the Schrödinger equation by brute force, it is still often too slow if the system size is larger than a few hundred atoms. Simplified methods based on empirical potentials and classical mechanics come to the rescue.

5.3.1 Justification of a classical approach

Why is a classical mechanics approach to an atomic scale problem valid? The physics and chemistry of a material are largely governed by its electronic structure, and electrons at room temperature have a de Broglie wavelength of more than 4 nm, which is much longer than the interelectronic distances, and thus much too long for a classical description to be valid. The resolution is the application of the Born–Oppenheimer approximation, which formalizes the consequences of the difference in mass between the atomic nuclei and the electrons[2]. In this approximation, the wave function is assumed to be separable in an electronic and an ionic part, and the electrons are assumed to instantaneously assume the ground state for given positions $\boldsymbol{r}$ of the ions. The result is that the Schrödinger equation for the full system can be simplified to a Schrödinger equation for the ionic wave function only, but with an effective potential $U(\boldsymbol{r})$ incorporating the energy of the electrons [106],

$$U(\boldsymbol{r}) = U_{ZZ}(\boldsymbol{r}) + \varepsilon_0(\boldsymbol{r}). \tag{5.7}$$

[2] In fact, the Born–Oppenheimer approximation underpins DFT and TDDFT as well, because without it the electronic wave functions would not have been separable from the ionic wave functions.

Here, $U_{ZZ}(\boldsymbol{r})$ is the potential energy from ion–ion interaction and $\varepsilon_0(\boldsymbol{r})$ the ground state energy of the electrons with ions fixed in positions $\boldsymbol{r}$. The de Broglie wavelength of an atomic nucleus in room temperature is always much smaller than the interatomic spacing, in particular for the heavier elements. A classical treatment of the ions is thus warranted, and since $U(\boldsymbol{r})$ is the effective potential for the ions, we can use it in the same way as we would use any classical potential. The quantum mechanics of the electrons is then implicitly taken into account in the functional form of $\varepsilon_0(\boldsymbol{r})$. It is worth noting that even though $U(\boldsymbol{r})$ is often referred to as the potential energy of the atoms, it contains also the kinetic energy of the electrons via $\varepsilon_0(\boldsymbol{r})$.

5.3.2 Embedded atom method

The possibility to use a classical potential to describe the energetics of a material is a blessing only if we can find a proper form for the interatomic potential $U(\boldsymbol{r})$. Whereas an exact expression is of course unattainable, many attempts have been made to find proper functional forms that can be fitted to experimental observations or theoretical results from quantum mechanics (usually obtained with DFT calculations). The simplest functional forms are pair potentials, which approximate the energy as a sum of pair interactions. Pair potentials have merit in their simplicity but fail to reproduce fundamental properties of most materials. A deficiency particularly damaging for metals is their built-in dependency of energy on the number of bonds. In a real metal, the energy scales approximately with the square root of the number of bonds; a bond formed in isolation is stronger than a bond formed in presence of other bonds [106, 107]. The expected scaling can be reproduced by functional forms with two terms,

$$U(\boldsymbol{r}) = \frac{1}{2} \sum_{\substack{i,j \\ i \neq j}} \phi_{ij}(r^{ij}) + \sum_i F_i[\rho^i]. \tag{5.8}$$

Here, r^{ij} is the distance between atom i and j, ϕ is a function that assigns an energy to each pair interaction, and F is a functional dependent on a yet unspecified function ρ. A number of potentials of this or similar forms were published in the 1980s and have come to be known as embedded atom method (EAM) [108], effective medium theory [109, 110], Finnis–Sinclair potentials [111], glue potentials [112] etc. The nomenclature is more diverse than the physics, and we will base the discussion on EAM, which is employed in Paper V and VI.

In EAM potentials, the functional F_i is referred to as the embedding term and depends on a linear superposition of the electron densities from the neighboring atoms [107],

$$\rho^i = \sum_{j \neq i} \rho_j^a(r^{ij}). \tag{5.9}$$

Here, ρ^a is a function that remains to be determined and just as before, r^{ij} is simply the distance between atom i and j, meaning that the electron density from each atom is approximated as spherically symmetric. Such a superposition of electron densities can be motivated by the Hohenberg–Kohn theorems [101], from which it is known that the energy can be written as a functional of the electron density. This concept was further elaborated by Stott and Zaremba [113] who showed that the energy of an impurity embedded in a host is a functional of the electron density of the unperturbed host. The impurity may in this case simply be the same kind of atom as the host. This shows that there is a fundamental reason for writing the energy as a functional of the electron density of the neighboring atoms, even though the exact form of this functional is unknown.

To construct an EAM potential for a specific material, one needs to determine ϕ, F and ρ^a. This is typically done by choosing certain physically reasonable functional forms with the desired number of free parameters and fitting those parameters to experimental and/or first-principles data for certain materials properties, which may include cohesive energy, lattice parameter, elastic constants, thermal expansion coefficients, defect formation and migration energies, phonon frequencies etc, all in one or more crystal structures. This task needs to be carried out with care and all potentials have a limited range of applicability, largely determined by the input data in the parameter fit.

As we have seen, EAM potentials assume a spherically symmetric electron density centered at each atom. Their accuracy is thus dependent on a high degree of non-directional bonding. The late transition metals are particularly well suited in this regard, because their filled d band (and s orbital in the case of the coinage metals) gives rise to a predominantly spherically symmetric electronic structure and thus low degree of directionality. For materials with a high degree of directionality, most notably covalently bonded solids such as diamond and silicon, other functional forms are needed and a viable approach is to include three-body terms, which is, however, beyond the scope of this thesis.

5.4 Alloy cluster expansions

In alloys, most of the thermodynamics often derive from the possibility to distribute the chemical species in different configurations on the lattice. Vibrations can play a role [114], but it is often a reasonable approximation that their contribution is independent of configuration and linear in composition, in which case they can be ignored for most purposes. While interatomic potential schemes (Sect. 5.3) can model vibrations, they are rarely flexible enough to accurately reproduce the energetics of different configurations. These considerations point to the possibility of developing models that are confined to a lattice but detailed enough to resolve small configurational differences. Alloy cluster expansions is an example of such models [115].

Consider a lattice decorated by two species of atoms. The decoration can be specified by a vector $\boldsymbol{\sigma}$, the n-th element of which is 0 if site n is occupied by species A and 1 if it

is occupied by B. In an alloy cluster expansion, the energy (or any other property) of the configuration $\boldsymbol{\sigma}$ is given by

$$E(\boldsymbol{\sigma}) = J_0 + \sum_{\alpha} J_\alpha m_\alpha \left\langle \Pi_{\alpha'}(\boldsymbol{\sigma}) \right\rangle_\alpha \tag{5.10}$$

where the summation is carried out over orbits α. Here, an orbit is a set of clusters that can be related to each other by the available symmetry operations of the underlying crystal structure. For example, the set of nearest neighbor pairs, the set of second-nearest neighbor pairs and the set of fifth-nearest neighbor pairs each form a distinct orbit. The parameters J_α are referred to as effective cluster interactions (ECIs) and quantify the energy contribution associated with each cluster, while m_α is the multiplicity of orbit α (i.e., the number of symmetry equivalent clusters that it contains). The factor $\left\langle \Pi_{\alpha'}(\boldsymbol{\sigma}) \right\rangle_\alpha$ is called a cluster correlation and quantifies how the orbit α is decorated, i.e., if α is the nearest neighbor pair, it measures how many of the nearest neighbor pairs are unlike (A–B) *vs* alike (A–A or B–B). It does so using so-called point functions $\Theta(\sigma_n)$, which in the binary case are $+1$ if $\sigma_n = 0$ (site n is occupied by A) and -1 if $\sigma_n = 1$ (site n is occupied by B). The correlation function for a cluster α' in the orbit α is

$$\Pi_{\alpha'}(\boldsymbol{\sigma}) = \prod_{n \in \alpha'} \Theta(\sigma_n), \tag{5.11}$$

which is then averaged over all symmetrically equivalent clusters $\alpha' \in \alpha$. The procedure is depicted in Fig. 5.1a. Note that the alloy cluster expansion is essentially a generalization of the Ising model described in Sect. 2.1.1.

It can be shown [115] that the correlation functions form a complete, orthogonal basis set, and thereby any function of the configuration σ can be expanded in the cluster space exactly. In practice, however, the infinite sum in Eq. (5.10) needs to be truncated. This is usually done by dropping clusters with many sites or long distances between sites. Although such a truncation can sometimes produce spurious interactions among the remaining clusters, especially if the volume of the system changes with composition [116], the nearsightedness of atomic interaction is often sufficient for the model to remain accurate. With a successful fitting, the accuracy of a cluster expansion often approaches that of DFT, while it is many orders of magnitude faster to compute. It can therefore be used for thermodynamic sampling, usually with the help of Monte Carlo (MC) methods (Sect. 5.6.3). A software for construction and sampling of cluster expansions was developed in Paper I and used in Paper II and III.

5.4.1 Determining the effective cluster interactions

With a truncated cluster space, the remaining task is to determine the ECIs J_α. This is a problem of solving a system of linear equations (see also Fig. 5.1b),

$$\boldsymbol{A}\boldsymbol{J} = \boldsymbol{E}. \tag{5.12}$$

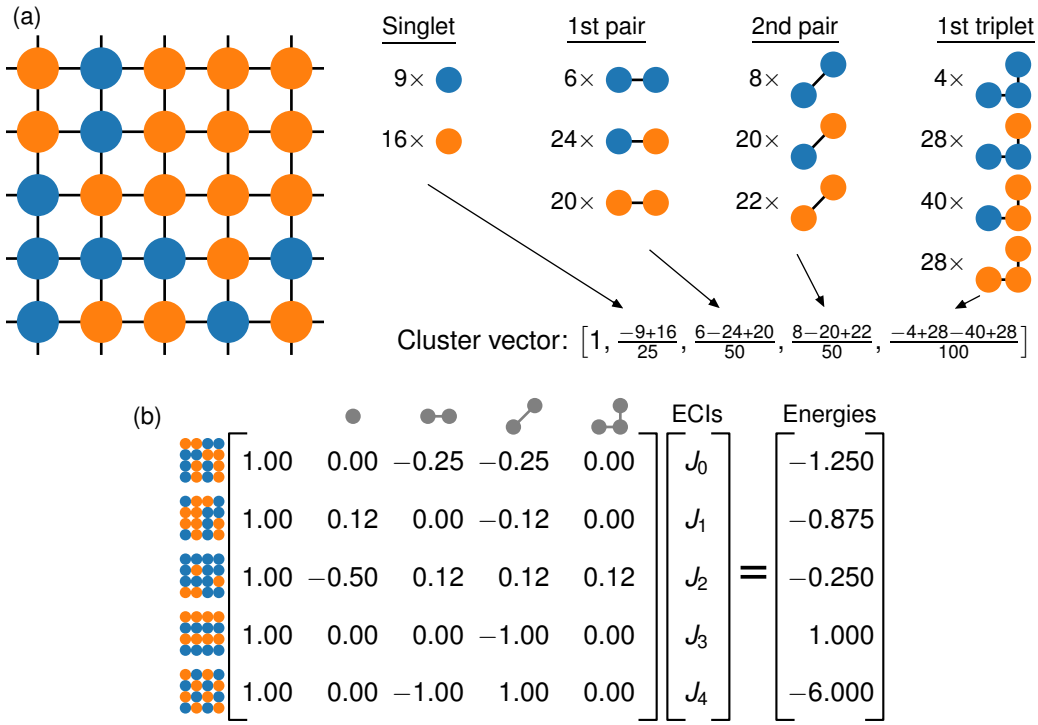

Figure 5.1: (a) The chemical order of an atomic structure can be quantified by its cluster vector, which is calculated by counting species, pairs, triplets and possibly higher-order clusters. For example, in the present case there are 50 nearest neighbor pairs in total. Among these, 6 are blue–blue, 24 blue–orange, and 20 orange–orange. By choosing $\Theta_{\text{orange}} = 1$ and $\Theta_{\text{blue}} = -1$, the cluster correlation for nearest neighbor pairs is $\langle \Pi_\alpha(\sigma) \rangle = [6 \times (-1 \times -1) + 24 \times (-1 \times +1) + 20 \times (+1 \times +1)] \big/ 50 = 0.04$. Here, the cluster expansion has been truncated already after the second nearest neighbor and after the first triplet. The first element of the cluster vector (the "zerolet") is always 1. (b) By calculating the cluster vectors of several structures with different chemical ordering, as well as their corresponding energies (using DFT or other methods), the matrix equation (5.12) can be set up. Each row of the matrix $\boldsymbol{A}$ corresponds to a unique configuration, and each column corresponds to a symmetrically distinct cluster. (Here, the multiplicities m_α have been included in the ECIs; sometimes they are instead included in the cluster vectors.) In this example, the number of parameters and target values are identical and the solution is unique. This is, however, usually undesirable, since it tends to lead to overfitting when the target values $\boldsymbol{E}$ contain noise. Instead, an under- or overdetermined system solved with linear regression techniques is often preferable (see Sect. 5.4.1).

Here, the vector $\boldsymbol{J}$ comprises the unknown coefficients J_α and $\boldsymbol{A}$ is a matrix, each row of which is called a cluster vector and corresponds to a certain configuration $\boldsymbol{\sigma}_i$, and each column corresponds to a different orbit α_j,

$$A_{ij} = m_{\alpha_j} \left\langle \Pi_{\alpha_j'}(\boldsymbol{\sigma}_i) \right\rangle_{\alpha_j}. \tag{5.13}$$

The vector $\boldsymbol{E}$ is often referred to as the training data and comprises the energies (or some other property) corresponding to a particular decoration, $E_i = E(\boldsymbol{\sigma}_i)$. Usually, it is an energy obtained with a DFT calculation of a structure having configuration $\boldsymbol{\sigma}_i$.

The most straight-forward approach for determining $\boldsymbol{J}$ is the well-known ordinary least squares (OLS) solution, $\hat{\boldsymbol{J}}_{\text{OLS}} = (\boldsymbol{A}^T\boldsymbol{A})^{-1}\boldsymbol{A}^T\boldsymbol{E}$. This estimate of $\boldsymbol{J}$ minimizes the sum of the squares of the errors[3],

$$\hat{\boldsymbol{J}}_{\text{OLS}} = \arg\min_{\boldsymbol{J}} \sum_i \left(E_i - A_{ij}J_j\right)^2. \tag{5.14}$$

Since the observed values E_i are not exact, this solution is prone to overfitting unless a very large number of observed values E_i can be included. Overfitting may lead to unphysical ECIs and a model that reproduces training data but not unseen data. Since $\boldsymbol{E}$ is typically a list of energies from DFT calculations, it is expensive to generate sufficient data to avoid overfitting.

A cheap approach to overcome overfitting is regularization. Specifically, the norm of the solution vector $\hat{\boldsymbol{J}}$ is suppressed by modifying Eq. (5.14),

$$\hat{\boldsymbol{J}}_{\text{reg}} = \arg\min_{\boldsymbol{J}} \sum_i \left[\left(E_i - A_{ij}J_j\right)^2 + \lambda J_i^n\right]. \tag{5.15}$$

Here, λ is a parameter that determines the extent of the regularization and n indicates that different norms can be used. With $n = 2$ (the L_2 norm), this is called ridge regression, and with $n = 1$ (the L_1 norm) least absolute shrinkage and selection operator (LASSO) [117, 118] is perhaps the most well-known approach to solve the problem. This approach to fit ECIs using a regularizing term has been used in many cluster expansion studies [119–122], including Paper I and Paper III.

Another approach to fit ECIs follows from Bayesian statistics [123]. We may view $\hat{\boldsymbol{J}}_{\text{reg}}$ as the parameter vector that, under certain conditions, yields the most probable model given the data. To understand this, we can rewrite Eq. (5.15) using logarithms,

$$\begin{aligned}\hat{\boldsymbol{J}}_{\text{reg}} &= \arg\max_{\boldsymbol{J}} \sum_i \ln\exp\left[-\left(E_i - A_{ij}J_j\right)^2 - \lambda J_i^n\right] \\ &= \arg\max_{\boldsymbol{J}} \ln\left\{\prod_i \exp\left[-\left(E_i - A_{ij}J_j\right)^2/2\sigma\right]\prod_i \exp\left[-\lambda' J_i^n\right]\right\},\end{aligned} \tag{5.16}$$

[3]Repeated indices are implicitly summed over.

where we also redefined λ in order to introduce a constant σ. If we assume that the error (or the noise) in the data follows a normal distribution with standard deviation σ, the first product represents exactly this distribution (up to a multiplicative factor). We may denote this distribution $P(\boldsymbol{E}|\boldsymbol{J})$, since it represents the probability of observing the data $\boldsymbol{E}$ given the model $\boldsymbol{J}$. To estimate the uncertainty in a model $\boldsymbol{J}$, however, we are rather interested in the opposite, the probability of $\boldsymbol{J}$ given the data $\boldsymbol{E}$, usually referred to as the posterior distribution $P(\boldsymbol{J}|\boldsymbol{E})$. The two are related according to Bayes' law [124],

$$P(\boldsymbol{J}|\boldsymbol{E}) = \frac{P(\boldsymbol{E}|\boldsymbol{J})P(\boldsymbol{J})}{P(\boldsymbol{E})}. \tag{5.17}$$

The denominator $P(\boldsymbol{E})$ is unimportant as it can be used for normalization, ensuring that the probabilities sum up to 1. The probability distribution $P(\boldsymbol{J})$ is called the prior distribution of $\boldsymbol{J}$, and we note that if we set it equal to the second product in Eq. (5.16), $P(\boldsymbol{J}) = \prod_i \exp[-\lambda' J_i^n]$, finding $\hat{\boldsymbol{J}}_{\text{reg}}$ is equivalent to finding the $\boldsymbol{J}$ that maximizes the posterior $P(\boldsymbol{J}|\boldsymbol{E})$. By modifying the prior, we adapt the problem to be solved. As physical intuition tells us that interactions should decay with distance and cluster order, we expect most ECIs to be small or zero. The Gaussian functions in Eq. (5.16) effectively reflect this intuition as they attribute a higher probability to parameter values close to zero. On the other hand, the OLS solution $\hat{\boldsymbol{J}}_{\text{OLS}}$ results if we use a flat prior, i.e., we consider all values of J_i to be *a priori* equally likely. The prior thus provides a means to facilitate the fitting by encoding physical intuition [125].

The parameter λ' can itself be part of the optimization. Automatic relevance determination regression (ARDR) [126], in particular, is a method for automatically solving Eq. (5.16) (with $n = 2$) while simultaneously optimizing λ', in this case using a separate λ' for each coefficient J_i. In Paper I we found that ARDR performed very well in a comparison with other regression techniques and it was therefore used also in Paper III (also see [127]).

Another advantage of the Bayesian approach is that the full posterior distribution can be produced with Markov chain-Monte Carlo simulations [128], and not only the parameters $\hat{\boldsymbol{J}}$ that maximizes it. Knowing the posterior distribution, a distribution of models can be constructed and uncertainties in quantities predicted by the model can thereby be estimated too. This approach was used in Paper II to quantify the uncertainty in the critical temperature of long-range order formation in Pd–Au–H as predicted by the cluster expansion.

5.4.2 Selection of training structures

Equation (5.12) generally becomes less vulnerable to both under- and overfitting with more training data, i.e., more rows in the matrix $\boldsymbol{A}$. Addition of a row is usually associated with DFT calculation of a structure with a unique configuration $\boldsymbol{\sigma}$, and the size of the training data set is thus limited by the computational expense of DFT. To avoid

an excessive number of DFT calculations, the set of configurations should be generated with care. This is often referred to as the problem of structure selection.

A simple approach to structure selection is random population of cells with a certain size and shape. This is unlikely to result in a useful training set, because it is almost guaranteed to yield mostly training structures that closely resemble the random solid solution. Multiple strategies for better structure selection have been proposed. Some focus on generating the structures that are the most important for the problem at hand, typically by an iterative process where cluster expansions are fitted, ground states or other important structures identified and added to the training set, and the process is repeated until, for example, a certain cross-validation score has been reached [129–131]. Other approaches attempt to reduce the variance of the predicted property (usually energy) as efficiently as possible [114, 132, 133]. Yet another strategy is to consider the properties of the matrix $\boldsymbol{A}$ and make its rows as orthogonal as possible [119]. For the cluster expansions in this work, we have mostly studied systems with small primitive cells, and we have been fortunate to have access to generous computational resources. It has therefore been possible to calculate several hundred structures, meaning that the problem Eq. (5.12) is considerably overdetermined. Under these circumstances, we have found the structure selection to have only a marginal impact on the performance of the cluster expansions, and we have mostly relied on so-called structure enumeration to provide the training data set.

5.4.3 Structure enumeration

For a given cell size, there exists a limited number of symmetrically distinct configurations $\boldsymbol{\sigma}$. By putting a limit on the cell size, it is thus possible to enumerate *all* symmetrically distinct configurations (see Fig. 5.2 for an example). Several algorithms for doing this efficiently have been proposed [134, 135], and we implemented the algorithm developed by Hart and Forcade [136, 137] within the scope of Paper I.

Enumeration of structures is not only a straight-forward and reproducible method for generating a certain number of structures, but it is also often used to build a pool of structures from which training structures can be drawn using a more elaborate scheme. In general, cells with few atoms can be expected to be a valuable addition to almost any training data set, because their cluster vectors are more likely to be "extreme" in the sense that they, for example, maximize the ratio of A–A and B–B to A–B nearest or next-nearest neighbor pairs (Fig. 5.3). It is for precisely this reason that ground states are generally expected to have small primitive cells [138], and structure enumeration can thus also be used to exhaustively search for ground states.

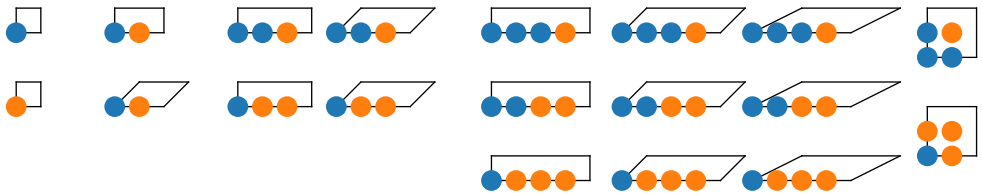

Figure 5.2: Structure enumeration of the two-dimensional square lattice with two species and up to four atoms in the cell. The structures are periodic and for each cell size, multiple cell shapes have to be included systematically. All structures are unique and the enumeration is exhaustive, i.e., any decoration of the square 2D lattice with four atoms or less is symmetrically equivalent to one of these structures. Note that the number of structures grows quickly when the cell size is increased.

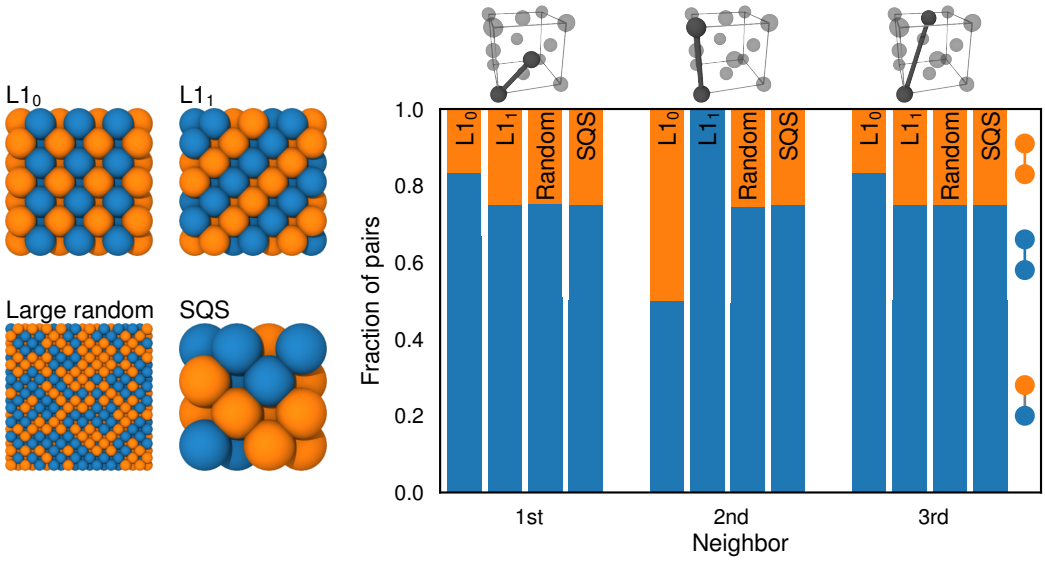

Figure 5.3: Pair cluster correlations in ordered, random, and quasi-random binary FCC alloys. Only two symmetrically distinct FCC alloys can be constructed with a primitive cell with two atoms, $L1_0$ and $L1_1$. In terms of cluster correlations, they are similar for first and third nearest neighbor pairs, but completely different for second nearest neighbor pairs; $L1_0$ has only A–A and B–B second nearest neighbor pairs, $L1_1$ has only A–B. If the ECI for second nearest neighbors is large, one of these structures is a good candidate for being the ground state (which one depends on the sign of the ECI). The random alloy is best represented with a large cell. When $c = 0.5$, it always has as many A–B pairs as it has A–A and B–B pairs, regardless of the distance between the sites. This character can be mimicked with the much smaller special quasirandom structure (SQS), which closely reproduces the cluster correlations of the fully random alloy.

5.5 Special quasirandom structures

As we saw in Chapter 2, (random) solid solutions are a common occurrence in transition metal alloys. It is therefore unfortunate that in principle an infinitely large cell is required to reproduce it exactly in atomistic simulations, unlike long-range ordered structures which typically require only a few atoms that are repeated by virtue of periodic boundary conditions. Of course, even a random alloy can be approximated by a sufficiently large cell. The cluster correlations introduced in the previous section provide a concept for systematically generating such quasirandom atomic structures [139]. Specifically, one recognizes that the most short-ranged pairs, and possibly a few triplets and higher-order clusters, are the most important for the properties of the alloy. A structure whose cluster correlations for these short-ranged clusters are similar to the cluster correlations of the truly random alloy should thus be a good representation of the random alloy (Fig. 5.3). To find such structures, the most common method is to define a cost function that quantifies the difference between the cluster correlations of a structure and the fully random alloy, and then minimize this cost function by MC and simulated annealing [140] (Sect. 5.7.3). The resulting atomic structure is called a special quasirandom structure (SQS) [139]. This was implemented within the scope of Paper I and used in Paper VIII to calculate the dielectric functions of random alloys using linear-response TDDFT.

5.6 Atomistic simulations

With a computationally efficient model such as an EAM potential or a cluster expansion, it is possible to sample a large number of states and thereby calculate a wealth of materials properties.

5.6.1 Molecular dynamics

One of the most obvious application of interatomic potentials is to temporally evolve a system of atoms in some geometry according to Newtonian mechanics[4]. This has been coined molecular dynamics (MD). Every atom i in a MD simulation is assigned an initial coordinate $\boldsymbol{r}_i$ and momentum $\boldsymbol{p}_i$ and the system is propagated in time with each atom acting on every other according to Newton's second law,

$$\boldsymbol{F}_i = -\nabla U(\boldsymbol{r}_i) = \dot{\boldsymbol{p}}_i. \tag{5.18}$$

The basic idea is simple but the actual implementation may be complicated with a wealth of considerations regarding, for example, discretization of time and space, boundary

[4]This is of course not possible with a lattice model such as a cluster expansion.

conditions, cutoffs in the interatomic potential and baro- or thermostats to mimic a desired physical situation.

5.6.2 Time and ensemble averages

Physical quantities are usually extracted from MD simulations by taking averages over time,

$$\bar{f} = \frac{1}{\tau}\int_{t_0}^{t_0+\tau} f(t)\,\mathrm{d}t. \tag{5.19}$$

Here, f is the sought-for physical quantity, t time, τ a certain time interval, and the data collection starts only after an initial time t_0 that allows the system to equilibrate. The spirit is the same as an experimental measurement, which does also always occur over some time, short or long.

It is often assumed that the time average equals the ensemble average,

$$\langle f \rangle = \frac{\int f(\boldsymbol{r},\boldsymbol{p}) e^{-\varepsilon(\boldsymbol{r},\boldsymbol{p})/k_\mathrm{B}T}\,\mathrm{d}r^N\,\mathrm{d}p^N}{\int e^{-\varepsilon(\boldsymbol{r},\boldsymbol{p})/k_\mathrm{B}T}\,\mathrm{d}r^N\,\mathrm{d}p^N}. \tag{5.20}$$

If the ergodic hypothesis holds for the system at hand, i.e., all microstates are equally probable over a sufficiently long time scale, we may indeed have $\bar{f} = \langle f \rangle$. In this context, it needs to be stressed that atomic motion occurs on the scale of picoseconds, which means that a typical MD simulation rarely exceeds microseconds and usually much less. The risk of having a system trapped between energy barriers in a certain part of phase space over the time scale of the simulation is thus significant, such that the time average will differ from the ensemble average even if the ergodic hypothesis holds for the system under consideration. A good example is a metallic alloy, for which atoms rarely exchange sites, hindering the use of MD for sampling configuration space. In such systems, other methods are called for.

5.6.3 Monte Carlo simulations

MC represents a wide class of computational methods that rely on sampling with a component of randomness to evaluate multidimensional integrals. Here, MC will be described in a limited scope as applied to configurational sampling of an alloy using the Metropolis algorithm. In such a simulation, the atoms are fixed and the system is described by the chemical identity of the atoms on each site. The simulation consists of changing the chemical identities on trial, and accepting or rejecting the change based on a carefully chosen criterion. Metropolis *et al.* [141] chose the criterion

$$P(\text{accept}) = \min\{1, \exp(-\Delta E/k_\mathrm{B}T)\}, \tag{5.21}$$

where ΔE is the change in potential energy caused by the trial. This choice ensures that an ensemble of systems subject to this criterion approaches the canonical ensemble [141], or in other words, a single simulation will sample a Boltzmann distribution. In the canonical ensemble, the concentration is always conserved, which means a trial change will always consist of a swap of chemical identity between two sites with unlike atoms. Such MC simulations may overcome the inability of MD to properly sample all of configuration space, because the simulation knows fewer energy barriers; all calculated quantities are ensemble averages and the algorithm is usually not designed to simulate a real trajectory.

5.6.4 The semi-grand canonical ensemble

The Metropolis criterion is readily generalized to ensembles other than the canonical one. The procedure is to simply replace ΔE in Eq. (5.21) with the change in the thermodynamic potential associated with the ensemble to be sampled (excluding the $-TS$ term). For alloys, a common choice is the semi-grand canonical (SGC) ensemble. This ensemble corresponds to a physical situation in which the difference in chemical potential between different species is fixed (in addition to temperature, volume and total number of atoms N). The SGC ensemble thus allows concentrations to fluctuate, such that a trial change can be taken as the change of chemical identity on a single site, i.e., no swap of two sites as in the canonical ensemble. A Legendre transformation [15, Chapter 5] reveals that the thermodynamic potential associated with the ensemble is

$$\Psi = E + Nc\Delta\mu - TS, \tag{5.22}$$

where N is the total number of atoms, $c = N_\mathrm{A}/N$ the concentration of species A, and $\Delta\mu = \mu_\mathrm{A} - \mu_\mathrm{B}$ the difference in chemical potential between species A and B. The modified Metropolis criterion is thus

$$P(\text{accept}) = \min\left\{1, \exp\left[-\left(\Delta E + N\Delta c\Delta\mu\right)/k_\mathrm{B}T\right]\right\}. \tag{5.23}$$

In MC simulations of alloys, the SGC ensemble has at least two advantages over the canonical ensemble. Firstly, the acceptance probability is sometimes better in the SGC ensemble for systems where moves that keep the energy low are rare. The probability of lowering the energy when swapping two randomly picked sites, as is done in the canonical ensemble, is essentially the square of the already low probability of finding a favorable flip. Secondly, the allowance to vary concentration makes it simple to continuously carry the system from one composition to another and integrate the free energy along the path. The theoretical foundation for this integration can be derived by

coarse-graining the SGC partition function in energy and concentration,

$$\begin{aligned}\mathcal{Z}_{\mathrm{SGC}} &= \sum_{s} \exp\left[(-(\epsilon_s + Nc\Delta\mu)/k_{\mathrm{B}}T\right] \\ &= \sum_{c,E} \Omega(c,E) \exp\left[-(E(c) + Nc\Delta\mu)/k_{\mathrm{B}}T\right] \\ &= \sum_{c,E} \exp\left[-(E - TS(E,V,N,c) + Nc\Delta\mu)/k_{\mathrm{B}}T\right] \\ &\approx \sum_{c} \exp\left[-(F(T,V,N,c) + Nc\Delta\mu)/k_{\mathrm{B}}T\right].\end{aligned} \tag{5.24}$$

where we introduced $\Omega(c,E)$ as the number of microstates with concentration c and energy E, and used the fact that the entropy at fixed c and E is the logarithm of this quantity (times k_{B}). The last step introduced the canonical free energy $F(T,V,N,c)$. For every value of T, V, N and $\Delta\mu$, and for a sufficiently large system, the term with the largest exponent will completely dominate the sum. Assuming the exponent is differentiable in c, we have

$$\frac{\partial}{\partial c}\left(F(T,V,N,c) + Nc\Delta\mu\right) = 0 \tag{5.25}$$

so that

$$\frac{\partial F}{\partial c} = -N\Delta\mu. \tag{5.26}$$

In practice, the canonical free energy energy can thus be recovered from a MC simulation in the SGC ensemble by continuously varying $\Delta\mu$ and recording the average concentration. When faced with multi-phase regions, however, this integration fails, because $\Delta\mu$ maps to multiple values of the concentration there. A MC simulation in the SGC ensemble will not be able to stabilize in such a region, but will discontinuously jump between the phase boundaries (Fig. 5.4). While such jumps contain information that may be exploited to, for example, construct phase diagrams [142], they prevent extraction of information from within the multi-phase region.

5.6.5 The variance-constrained semi-grand canonical ensemble

To overcome the limitations of the SGC ensemble in multi-phase regions, Sadigh *et al.* [143, 144] developed the variance-constrained semi-grand canonical (VCSGC) ensemble, which takes inspiration from the SGC ensemble but introduces a parameter $\bar{\kappa}$ that constrains the fluctuations (variance) of the concentration. Its thermodynamic potential can be written

$$\Psi_V = E + \bar{\kappa}Nk_{\mathrm{B}}T\left(c + \bar{\phi}/2\right)^2 - TS \tag{5.27}$$

where $\bar{\phi}$ replaces $\Delta\mu$ as the parameter that drives the concentration. For a sufficiently large value of $\bar{\kappa}$, the mapping between $\bar{\phi}$ and c becomes single-valued so that a simulation can stabilize concentrations also inside multi-phase regions (Fig. 5.4). It is thus

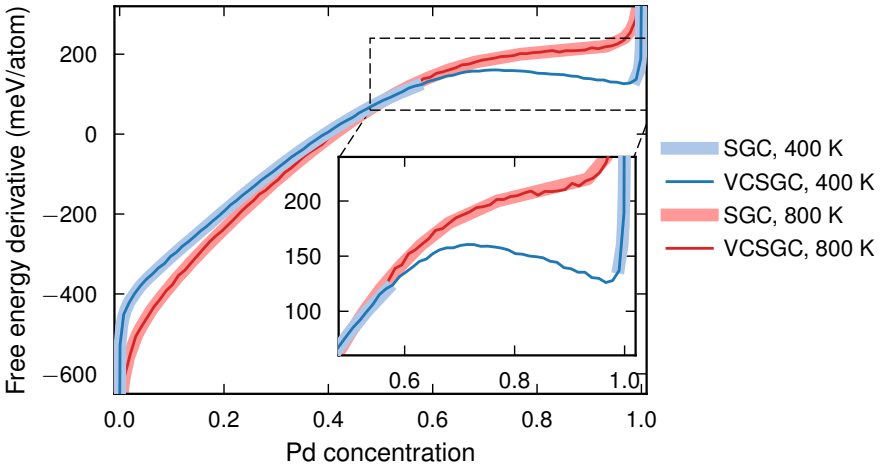

Figure 5.4: Free energy derivative as a function of Pd concentration in the Ag–Pd alloy calculated with MC simulations in the SGC (thick lines) and the VCSGC (thin lines) ensembles (Paper I). The two ensembles yield identical results everywhere except in the two-phase region (magnified in the inset), where the SGC simulation jumps between the phase boundaries whereas the VCSGC simulation stabilizes also between the phase boundaries. The VCSGC data can thus, unlike the SGC data, be integrated across the two-phase region.

possible to extract thermodynamic data also inside multi-phase regions, a feature that was extensively utilized in Papers III, V, and VI. In particular, it can be derived in a fashion equivalent to Eq. (5.24) that the derivative of the canonical free energy can be expressed in terms of observables of the VCSGC ensemble [143],

$$\frac{\partial F}{\partial c} = -2\bar{\kappa}Nk_{\mathrm{B}}T\left(c + \bar{\phi}/2\right). \tag{5.28}$$

It is thus possible to integrate the free energy across multi-phase regions by sweeping $\bar{\phi}$ and recording the average concentration along the path. This can greatly simplify phase diagram construction from MC simulations, and the VCSGC ensemble was employed for this purpose in Papers I–III.

5.6.6 Hybrid MD–MC simulations

When discussing the energetics of alloys, it is often convenient to split the partition function in a configurational and a vibrational part,

$$Z = \sum_{\boldsymbol{\sigma}} \int_{\Omega_{\boldsymbol{\sigma}}} e^{-E/k_{\mathrm{B}}T}\, \mathrm{d}r^N\, \mathrm{d}p^N. \tag{5.29}$$

Here, the configurational part is represented by a sum over all possible decorations $\boldsymbol{\sigma}$ of the lattice, whereas the vibrational part is represented by a multidimensional integral

over the part of phase space Ω_σ consistent with each decoration. It is often advantageous to evaluate the different parts with different methods; because MD is particularly well suited for sampling the vibrational part and MC the configurational part, we may combine the two. In practice, this means that we run a MD simulation but interrupt it at regular intervals to carry out a series of MC trial steps. A quantity of interest is then calculated by time averages over the vibrational part combined with ensemble averages over the configurational part. This technique was employed in Paper VI.

5.7 Energy minimization techniques

MD and MC simulations are often used to study materials at a specific temperature. A well-behaved system will approach equilibrium, and equilibrium properties can be extracted by calculating averages and analyzing trajectories. As a special case, one is often interested in the equilibrium at zero temperature, i.e., the ground state. The ground state is characterized by a minimum in potential energy and is as such, if nothing else, attractively well-defined and of fundamental interest. For many systems it also often provides a reasonable approximation to the equilibrium state at room temperature, provided that the melting temperature is much higher. Unfortunately, it is not straightforward to extract the ground state from MD or MC simulations, because sampling can become prohibitively inefficient at low temperatures.

5.7.1 Spatial and configurational global optimization

The separation of the partition function in a configurational and a spatial part (as in Eq. (5.29)) is fruitful when facing the task of finding ground states in metallic systems. For monometallic particles, the configurational part disappears and the problem is essentially to position a given number of atoms in space such that their interaction yields the lowest energy. Given that every atom has three coordinates, this problem is extraordinarily difficult already for clusters with less than a few tens of atoms. The problem has received considerable attention and become the target of many novel optimization schemes [145]. A wide array of techniques exist [146, 147], many of which are based on either genetic algorithms [148, 149] or basin hopping [150–152].

The problem of optimizing the configuration, i.e., assigning an optimal ordering of chemical identities, is quite different, because in this case the possible states are discrete. For a binary system with N atoms of which N_A are of type A and N_B of type B, the number of possible configurations n is exactly

$$n = \frac{N!}{N_\mathrm{A}!N_\mathrm{B}!}. \tag{5.30}$$

Usually, many of these are equivalent by symmetry, but the number is still extremely large for a few tens of atoms and non-dilute concentrations. This problem is even more

well-studied than monoelemental optimization, but the gallery of useful optimization techniques turns out almost the same [146, 147, 153, 154], even though the possibility of lattice-based energy models for alloys opens an avenue to more specialized methods [155]. It should be stressed that the configurational and spatial parts are dependent; the optimal configuration may change as the positions of the atoms are changed. Global optimization of a nanoalloy is thus significantly more difficult than global optimization of a monoelemental particle.

5.7.2 Local optimization

The complexity of the global optimization problem has necessitated restricted searches for local minima. A particularly common approach has been to restrict the positions of the atoms to the vicinity of a structural motif and then optimize the chemical configuration subject to that structure, possibly allowing local relaxation [88, 156, 157]. The structures have usually been chosen from the high-symmetry motifs described in Chapter 3. Both global minimization studies and experimental observations have repeatedly pointed to the relevance of these structures, and even if a particular configuration in the chosen structure is not a global minimum, experimentally a nanoparticle may very well be kinetically trapped in that structure. This is the philosophy of Paper V and VI.

5.7.3 Simulated annealing

Another widespread approach to optimization is simulated annealing (Fig. 5.5). It is inspired by the protocol an experimentalist might follow to quench a real system into its ground state. A MD or MC simulation is started at high temperature, where chances are good that energy barriers can be overcome, and the temperature is gradually lowered. The system is then expected to approach its ground state (or a local minimum if the setup constrains the system to a certain part of phase space). There is a risk that the system is quenched into a funnel of the potential energy surface whose bottom is not the ground state. Still, simulated annealing does in practice often identify the global ground state, in particular if the process is repeated multiple times. Simulated annealing with hybrid MD–MC was employed in both Paper V and VI.

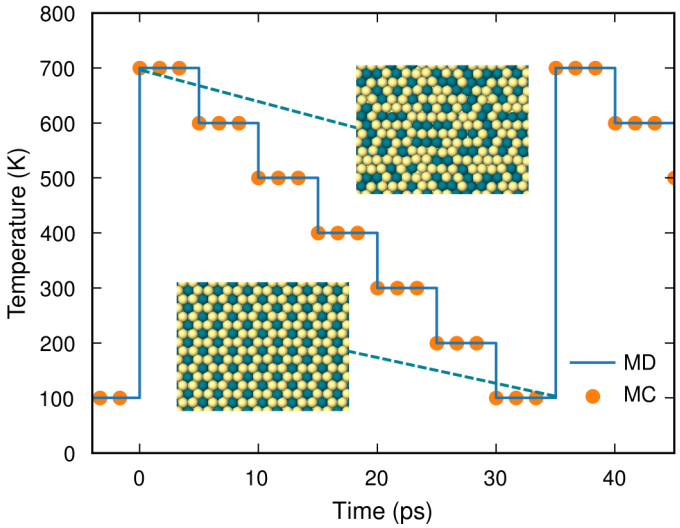

Figure 5.5: Schematic of simulated annealing in a hybrid MD–MC simulation of a Au–Pd {111} surface alloy. Orange dots indicate that the MD propagation is interrupted for MC trial steps. At high temperatures, the surface is disordered but as low temperatures are reached, the surface assumes an ordered ground state, in this case a honeycomb pattern.

6

Summary of papers

Paper I

ICET – A Python library for constructing and sampling alloy cluster expansions

This paper introduces ICET, an open-source software package for constructing and sampling alloy cluster expansions. Being largely written in Python and integrated with the Atomic Simulation Environment [158], ICET aims to simplify and accelerate the construction of cluster expansions, while still lending sufficient flexibility to allow for custom solutions. The package includes a submodule that allows sampling via MC simulations. Various supplemental tools have been implemented, including structure enumeration [136, 137], generation of SQS [139], convex hull construction [58], exact ground state search using mixed integer programming [155] and Wang-Landau sampling [159]. We illustrate the usage of ICET with two examples: phase diagram construction for Ag–Pd and chemical ordering in the inorganic clathrate $Ba_8Al_xSi_{46-x}$.

The documentation of ICET is available at `https://icet.materialsmodeling.org`. A web application for the generation of special quasirandom structures in the browser, using ICET on the server-side, has been developed and is available at `https://sharc.materialsmodeling.org/sqs`.

Paper II

A tale of two phase diagrams: Interplay of ordering and hydrogen uptake in Pd–Au–H

As discussed in Chapter 2, Pd alloyed with Au behaves differently compared to pure Pd when it comes to the response to a hydrogen-rich environment. Most notably, the

phase transition from a hydrogen-poor to a hydrogen-rich phase is suppressed by a relatively small content of Au, and the relationship between hydrogen uptake and hydrogen pressure becomes more linear. While these properties are favorable for many applications, the alloy is also more complex than pure Pd in the sense that different chemical orderings on the Pd–Au lattice can influence the properties of the material. For example, it has been shown experimentally that annealing of a Pd–Au alloy with 19% Au in a hydrogen-rich environment, causes long-range order formation and thereby a significantly higher hydrogen uptake [22].

In this paper, we carry out a thorough investigation of how the chemical ordering of Pd–Au influences its hydrogen uptake, and, conversely, how uptake of hydrogen influences the chemical ordering. To this end, we used ICET to construct alloy cluster expansion models and we sampled these models using MC simulations.

The Pd–Au–H system can be described as two interpenetrating FCC sublattices, one with Pd and Au, and one with H and vacancies. In this paper, we exploited the possibility of sampling these two sublattices with different ensembles. This is not only practical from a computational standpoint, but is also grounded in the fact that in most experiments, the composition is conserved on the Pd–Au sublattice (a closed thermodynamic system) while it varies on the H–vacancy sublattice (an open thermodynamic system), being controlled by the partial pressure of H_2 in the environment. With this approach, we can also fix the Pd–Au sublattice and sample only the H–vacancy sublattice, and thereby mimic a para-equilibrium situation (discussed in Sect. 2.2.4). In this paper, we distinguish two extremes, *para-equilibrium* in which the Pd–Au sublattice has been equilibrated at 300 K, and *random equilibrium* in which the Pd–Au sublattice is completely random ("equilibrated at infinite temperature"). The difference is that there is some degree of short-range order in the former case. The results indicate that the short-range order in para-equilibrium has only minor consequences for the uptake of hydrogen. It is only at fairly high Au concentrations ($\gtrsim$ 15%) that the hydrogen uptake is somewhat higher in random equilibrium than para-equilibrium at a fixed hydrogen pressure. The phase diagram (Fig. 6.1a) is virtually indistinguishable in these two cases.

In *full equilibrium*, in which equilibrium forms on both sublattices simultaneously, the situation is more complex. The major difference compared to para-equilibrium is that at sufficiently high H_2 pressures and not too high temperatures, a long-range ordered $L1_2$ phase forms. This phase opens a multiphase region in the phase diagram, i.e., phase separation between this ordered phase and other phases are expected in full equilibrium (Fig. 6.1b). Just as observed experimentally [22], this ordered phase enables a significantly higher hydrogen uptake at low hydrogen pressures. It might thus be possible to boost the sensitivity of Pd–Au-based hydrogen sensors by synthesizing sensors with this ordered phase using annealing at high H_2 pressures. To guide experimentalists in this regard, we provide a prediction of which temperatures and hydrogen pressures are required to form this phase. While the pressures required are high, they are by no means inaccessible.

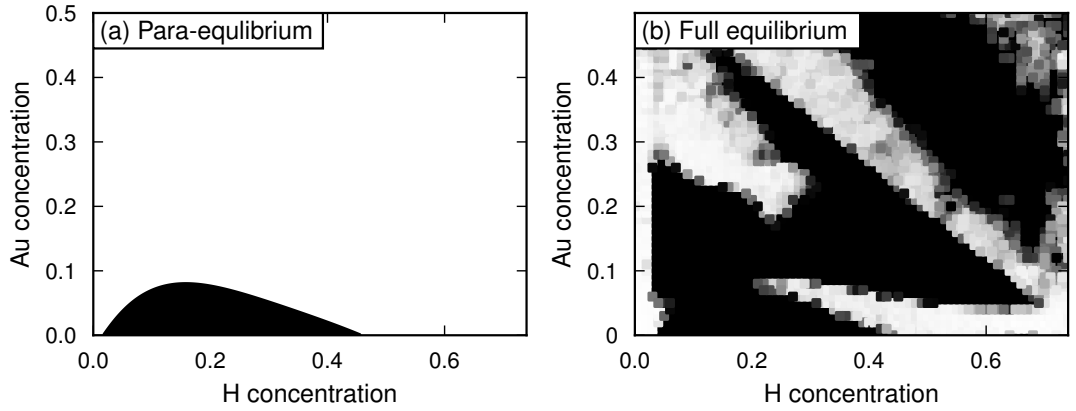

Figure 6.1: Phase diagrams for Au–Pd–H at 300 K in (a) para-equilibrium and (b) full equilibrium. White indicates single-phase regions, black multi-phase regions. In para-equilbrium, there is a two-phase ($\alpha + \beta$) region that closes upon addition of a sufficient amount of Au. The phase diagram in full equilibrium contains approximately the same two-phase region, but also a much larger multi-phase region that is largely caused by the stable $L1_2$ phase phase at approximately 25% Au and 10–25% H.

Paper III

Quantitative predictions of thermodynamic hysteresis:
Temperature-dependent character of the phase transition in Pd–H

An assumption implicitly underlying much of the analysis of Paper II was that the interface between phases remains incoherent, such that the constituent phases are not strained. As discussed in Sect. 2.3, this is typically not the case during hydration of Pd nanoparticles smaller than approximately 300 nm in diameter [45, 46]. In this paper, we develop a methodology to study this phase transition under the assumption that it is coherent. We do so by constructing a cluster expansion using the constituent strain formalism first developed by Laks *et al.* [160]. Unlike a regular cluster expansion, such a cluster expansion is able to recognize coherently strained phases by the use of a structure factor calculation, and it assigns the proper strain energy to such configurations based on systematically pre-calculated DFT data. We then sample this cluster expansion with the VCSGC ensemble and show how the MC data inside the two-phase region reveal the nature of the phase transition in both the incoherent and the coherent case.

With this approach, we find a critical temperature for the phase transition at $T_c = 540$ K, which is within 20 K of the experimental value [50] (Fig. 6.2). Further, we find that the system exhibits a coherent critical temperature at $T_c^{coh} \approx 400$ K. In the temperature range between T_c^{coh} and T_c coherent phase coexistence is not possible, and if no defects are formed, the system must transition from α to β without coexistence between the two

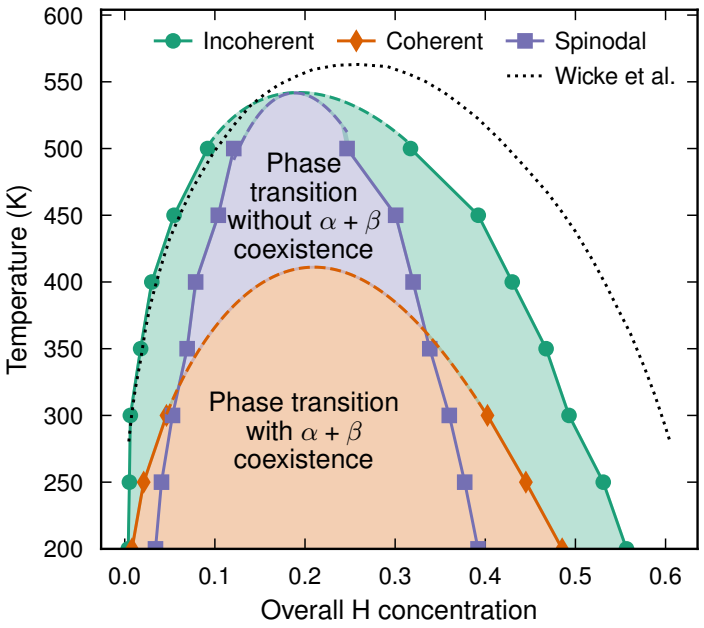

Figure 6.2: Phase diagram for Pd–H with incoherent (green) and coherent (orange) phase boundaries, as well as spinodals (purple). The coherent phase boundary closes at the coherent critical temperature at approximately 400 K, whereas the critical temperature for the phase transition is $T_c = 540$ K (within 20 K of the experimentally estimated critical temperature [50]). If the system stays fully coherent, phase transition with $\alpha + \beta$ coexistence will only occur below the coherent critical temperature. Between the coherent critical temperature and T_c, the phase transition will proceed with a spatially homogeneous hydrogen distribution. The spinodals mark the limits where this phase transition becomes spontaneous.

phases, i.e., the system maintains a spatially homogeneous concentration throughout the full phase transition.

Finally, we show that temperature-dependent interface free energies can be calculated using extrapolation of the free energies of simulation cells with decreasing length. The results show that among {100}, {110} and {111} interfaces, {100} has the highest interface energy and {111} the lowest. This energetic ordering is opposite to the one obtained for the strain energy, which is the lowest for {100} interfaces. Interface energy and strain energy thus favor different orientations for phase separation, but since the coherent interface energies are very small, they will for most systems play only a minor role.

Paper IV

WulffPack: A Python package for Wulff constructions

Even though the Wulff construction is conceptually simple, there have been no readily available and versatile Python implementations, which is unfortunate given the prevalence and increasing popularity of Python in scientific computing to date. This paper presents WULFFPACK, a Python package that fills this gap. The core of WULFFPACK creates a Wulff construction based on the algorithm described in Sect. 3.2.1, given input in the form of surface energies and the symmetry elements of the relevant point group. These symmetry elements are deduced using SPGLIB [161] from the crystal structure provided by the user. WULFFPACK also creates icosahedra, decahedra and Winterbottom constructions, which are internally created in the same way as standard Wulff constructions, with the only difference being a reduction of the symmetry. Visualization of the Wulff shapes is handled by MATPLOTLIB [162]. The shapes can be analyzed with regard to, for example, the area fraction of each facet (see Fig. 6.5 for an example). Using the Atomic Simulation Environment [158], WULFFPACK also supports creation of atomistic representations.

WULFFPACK is open source and its documentation, including a user manual, is available at `https://wulffpack.materialsmodeling.org`. A web application that interactively creates Wulff constructions for the case of cubic symmetry has been developed and is available at `https://sharc.materialsmodeling.org/wulff_construction`.

Paper V

Beyond magic numbers: Atomic scale equilibrium nanoparticle shapes for any size

This paper introduces an algorithm for predicting atomistic nanoparticle structures in a wide size range. At its core, it is a straight-forward application of MC simulations to the binary metal–vacancy system. As mentioned in Sect. 2.1.3, this system is immiscible, and the SGC ensemble fails to stabilize any composition but pure vacuum and bulk. It thus provides an attractive use case for the VCSGC ensemble (Sect. 5.6.5). The algorithm is based on simulated annealing coupled to a sequential sweep of the concentration driving parameter $\bar{\phi}$ of the VCSGC ensemble. MC trial steps changing atoms to vacancies or vice versa are regularly interrupted for atomic relaxation and the lowest energy structure for each number of atoms is recorded. The algorithm relies on an *a priori* definition of a structural "lattice", in this case single-crystalline, decahedral, or icosahedral. Atoms are only allowed to relax locally from this lattice, such that the energy minimum search remains close to the *a priori* defined structural motifs.

Our algorithm successfully identifies previously reported high-symmetry nanopar-

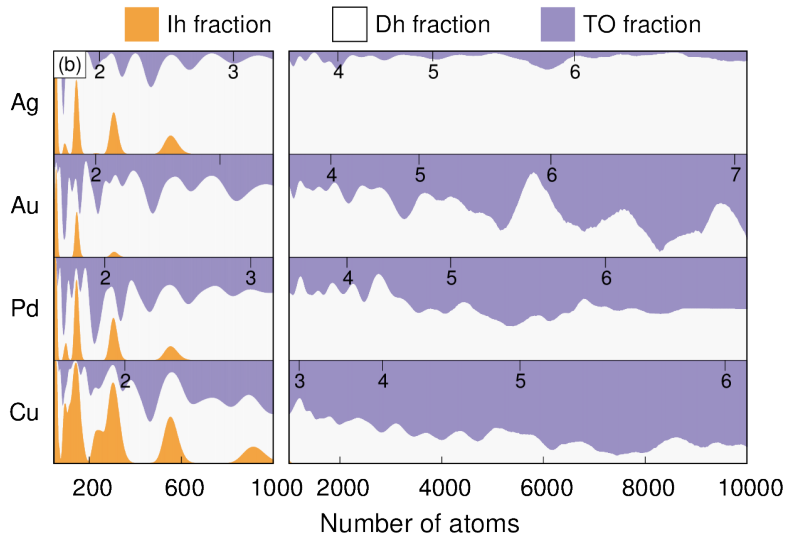

Figure 6.3: Distribution of structural motifs in thermodynamic equilibrium at 300 K, assuming at each atom count N a standard distribution of particle sizes of $0.05N$. Icosahedral particles (orange) dominate around their magic numbers, but only at small sizes. For larger particles, decahedral (white) and truncated octahedral (purple) particles prevail. Note, however, that there is more than one shape at almost any size. Approximate nanoparticle diameters are indicated at the top of each subpanel.

ticles of all three structural motifs, indicating that the algorithm is stable and capable of identifying ground state structures. Interestingly, for single crystalline and decahedral particles our algorithm finds particles with energy on par with the energy of the magic number particles for *any* number of atoms. The primary reason is that both of these motifs provide ample opportunity for slight modifications of facet areas, shapes and asymmetries, which all have a very small impact on the total energy. For icosahedral particles, however, this is not the case. Non-magic icosahedral particles are almost always stepped yielding an energy often substantially higher than the magic number particle energy.

The map of nanoparticle size to energy anywhere in the range from 100 to 10,000 atoms is a first of its kind, and the paper concludes with a quantification of the consequences for Ag, Au, Pd and Cu as calculated with EAM potentials. Further analysis reveals that thermodynamic equilibrium ensembles almost always include more than one structural motif (Fig. 6.3). The primary reason is that the different particle sizes in a polydisperse ensemble will usually not all have the same ground state structural motif, since the rapid variations in ground state energy with particle size imply multiple crossovers in energy between the three motifs considered.

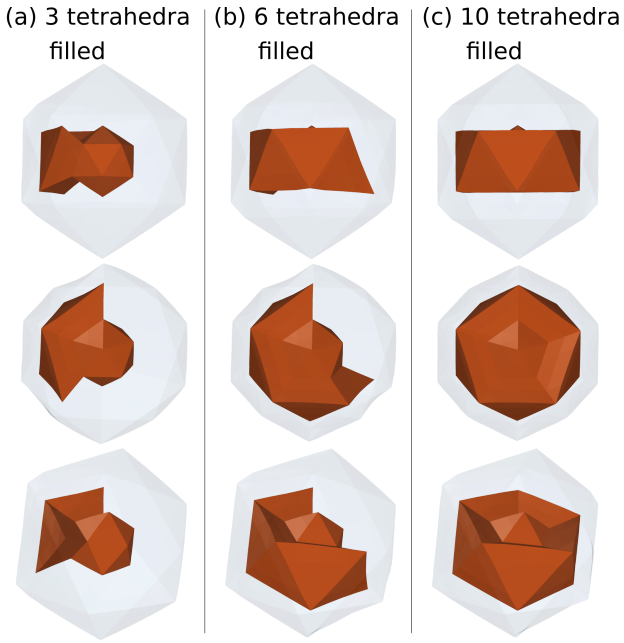

Figure 6.4: Filling of Cu in an icosahedral Ag–Cu particle with 561 atoms. The simulations were performed on the atomic scale, but only the surface of the particle (transparent grey) and the "surface" of the Cu segregate (red) are shown here (the figures were created with the OVITO software [163]). The tetrahedra that build up the icosahedron are filled sequentially (a–b) until a complete Cu ring of ten tetrahedra has been formed (c). Each column show the same particle from different angles.

Paper VI

Understanding chemical ordering in bimetallic nanoparticles from atomic-scale simulations: The competition between bulk, surface, and strain

In this paper, the attention is turned to nanoalloys. Specifically, the paper contrasts the chemical ordering in Au–Pd and Ag–Cu particles. The computational method is hybrid MD–MC simulations with energies calculated with EAM potentials. The paper focuses on results from simulated annealing, but simulations run at room temperature yield practically identical results.

We invoke bulk-like interactions, surfaces and strain to explain differences in chemical ordering. Au–Pd mixes in all proportions in the bulk, whereas Ag–Cu has a wide miscibility gap. Our results indicate, as do the great majority of previous theoretical studies in the nanoalloy field, that this general mixing behavior is preserved at the nanoscale. The presence of a surface, however, causes interesting phenomena. For Au–Pd, where the surface energies of the pure constituents differ substantially, there is a pronounced

surface segregation. The favorable Au–Pd bond, however, causes an excess of Pd in the subsurface layer. In the Ag–Cu system in which bonds between like atoms are favorable, there is no such enrichment in the subsurface layer. Although this observation may appear obvious, it is important to keep in mind for an experimentalist who measures surface composition with a technique that probes more than just the topmost surface layer.

Furthermore, the Au–Pd and Ag–Cu systems respond differently to strain. The increase in strain when going from a single crystalline particle to an icosahedron via a decahedron, provides a playground to test this effect. Au–Pd has a small size mismatch and the difference in chemical ordering between the three motifs is consequently small. For Ag–Cu, however, which has a large size mismatch, there is a pronounced difference between the motifs. The arguably most intriguing consequence is the sequential filling of the tetrahedra in an icosahedron, which gives rise to a previously not reported sandwich-like structure at intermediate compositions (Fig. 6.4).

Paper VII

Computational assessment of the efficacy of halides as shape-directing agents in nanoparticle growth

Paper V and VI considered the energetics of nanoparticles in vacuum. A more realistic situation is that the nanoparticles are in contact with either a gas or a liquid. This is of particular importance in the case of colloidal synthesis, in which nanoparticles are grown in a complex aqueous environment, the nature of which determines the outcome of the nanoparticle growth. In this field, halide ions, such as Br^-, are widely used as so-called shape-directing agents due to their ability to direct the nanoparticle growth to certain shapes. These ions bind to metal surfaces, but the strength of the bond depends on the faceting of the metal, and the equilibrium shape of the nanoparticle—the Wulff construction—is thereby altered.

In this paper, a model to accurately describe the energetics of halide absorption on metal surfaces in aqueous environments is formulated. The water is here treated implicitly, as explicit inclusion of water molecules would render the computations much too expensive. The model is applied to binding of F^-, Cl^- and Br^- to different Au and Pd facets. Based on this data, we use WULFFPACK (Paper IV) to create Wulff constructions (regular and decahedral) as a function of concentration of halides in the solution.

The results show that qualitative changes in nanoparticle shape occur as the halide concentration in the solution is varied. For example, the calculations predict that Au nanoparticles in low concentrations of Br^- show a large proportion of {311} facets, but when the concentration increases, the {311} facets gradually give way for other facets, most notably {100} (Fig. 6.5). These results underscore the need for careful modeling of nanoparticle shapes in aqueous environments.

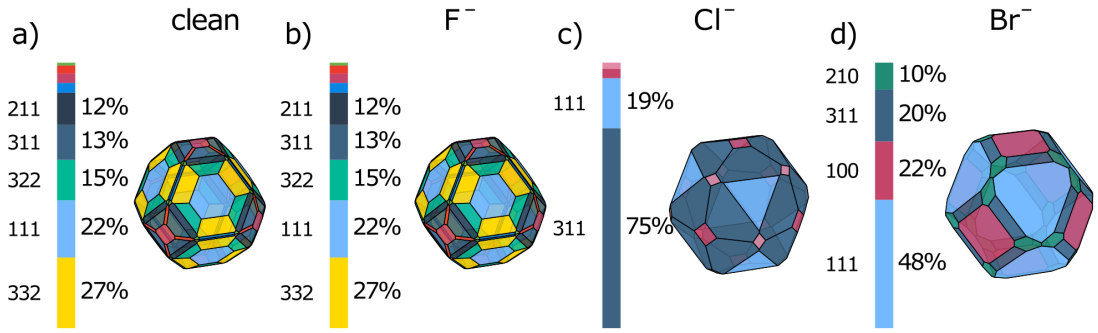

Figure 6.5: Equilibrium shapes of Au nanoparticles immersed in (a) pure aqueous solution and (b–d) aqueous solution with 0.1 M halides. (b) F^- adsorption on Au is endothermic and does therefore not induce a shape change. (c) Cl^- and (d) Br^-, on the other hand, have a large impact on the nanoparticles by promotion of {311}, {111}, and {100} facets.

Furthermore, bromides in particular are commonly used in nanoparticle synthesis to promote growth into cubes and rods. Our results indicate that these shapes do not appear as thermodynamic ground states even in presence of Br^-. Instead, we argue that their emergence in experiment is the result of an interplay with kinetics, possibly due to blocking of certain facets by high coverage of adsorbates.

Paper VIII

A library of late transition metal alloy dielectric functions for nanophotonic applications

The optical response of nanoparticles and systems of nanoparticles can often be modeled with good accuracy using the finite-difference time-domain method to numerically solve Maxwell's equation for specific geometries. A crucial ingredient in these calculations are dielectric functions. For noble metals, the dielectric functions are often taken from experimental measurements performed in the 1970s. While gold is every bit as much gold as it was in the 70s, by comparing different experimental measurements (as is done in the supplementary material of this paper) one observes a wide spread in the experimental data. This spread may be caused by differences in microstructure, surface structure, and purity of the measured samples, as well as systematic errors in the measurements [164]. Furthermore, different experimental techniques cover different photon-energy ranges, and to obtain dielectric functions covering a wide spectrum, data from different experiments need to be patched together. These aspects are particularly unfortunate when comparing materials using electrodynamic modeling, because it may be unclear if perceived differences are caused by the actual properties of the materials or if they are the consequence of differences in the experiments that assessed

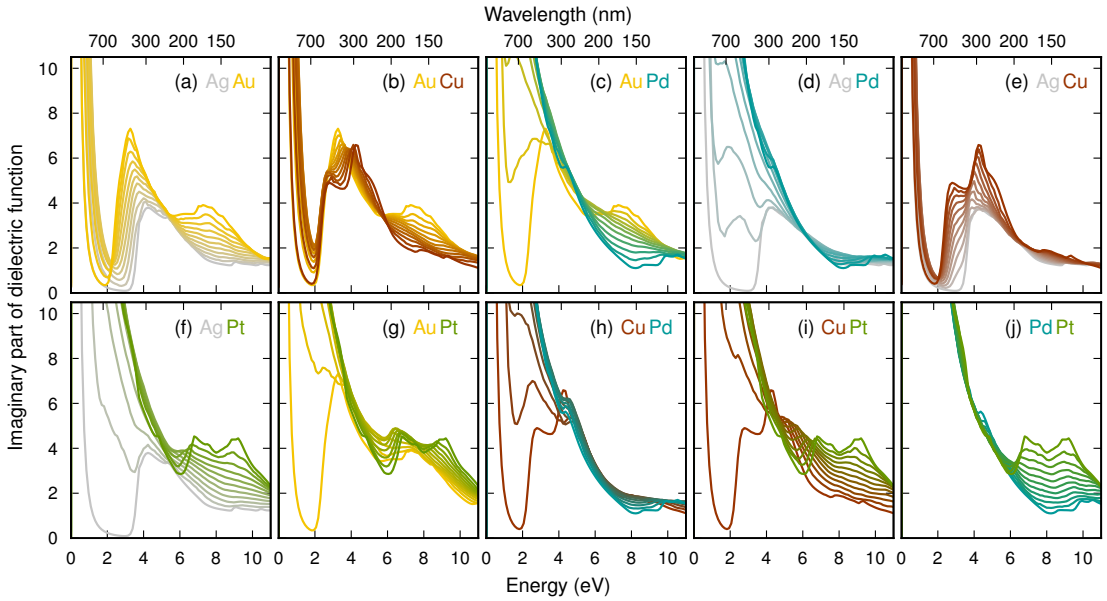

Figure 6.6: Imaginary part of the dielectric functions of ten alloys as calculated with linear-response TDDFT.

them. Furthermore, the dielectric functions of alloys, which are becoming increasingly widespread in nanoscience, have only been partially explored [96, 165–167].

To provide the community with a self-consistent set of dielectric functions of experimentally relevant alloys, we used linear-response TDDFT to calculate the dielectric functions of the ten binary alloys formed by combinations of Ag, Au, Cu, Pd, and Pt (Fig. 6.6). In this set of data, we highlight the position of the d band with respect to the Fermi level as one of the most important descriptors of the optical response, and we find that the shift of the d band upon alloying is largely linear for isovalent alloys (such as Ag–Au) but strikingly non-linear for non-isovalent alloys (such as Au–Pd). We benchmark our results by electrodynamic simulation and experimental measurement of the optical extinction spectra of nanoalloys of four of these alloys. Our hope is that this library of data will be a complement to experimental measurements of the same quantities [165, 166], and be useful to scientists who seek to understand or optimize nanoplasmonic systems, or other optical systems with alloys.

For simpler access and exploration of this fairly large data set, we developed a web application in which the dielectric function of these alloys at any composition can be obtained and compared in multiple ways (`https://sharc.materialsmodeling.org/alloy__dielectric__functions`).

7 Outlook

The purpose of this thesis has been to develop and apply computational tools to better understand materials, in particular those related to plasmonic sensing of hydrogen with palladium-based nanoalloys. As with most scientific investigations, it is not the end of the road. This chapter will briefly suggest future extensions of the present work, in particular with regard to its methodologies.

Some of the methods employed here should be fairly easy to combine. For example, the algorithm developed for the study of nanoparticle shapes in Paper V can be used together with an alloy cluster expansion in which one of the species is vacancies. There are examples of such cluster expansions in the literature [125, 168] and some steps have already been taken in this direction with ICET. In such calculations, it is important to define *a priori* what the targets of the simulations are. Based on experience accumulated during the work in this thesis, it is fair to say that size-dependent trends of the polynomial kind discussed in Sect. 3.1 are usually very easy to capture with cluster expansions or indeed any physically reasonable model. The finer details, such as the small differences in energy between nanoparticles with the same number of atoms but different structure, are much more challenging to describe accurately. The cluster expansion approach is typically also unable to capture strain, which, as we have seen, is often substantial in nanoparticles, especially small ones. The constituent strain approach taken in Paper III is not easily applicable to the metal–vacancy system, because vacuum is not elastic. Some version of concentration-dependent ECIs might be a path forward [116, 169, 170], but one needs to be careful not to equate the concentration of metal in the metal–vacancy system with nanoparticle size, because they are only equivalent if the cell size is kept fixed.

The calculation of dielectric functions using SQS and linear-response TDDFT is easily generalizable to other materials. The stage is thus set for calculation of dielectric functions for Pd–Au–H and if combined with the thermodynamics elucidated in this thesis,

this would give us an almost complete model for the optical response of Pd–Au hydrogen sensors. This model would in fact be first-principles in the sense that no experimental input is required for its construction. Such a model would, for example, give an atomic-scale understanding of how the sensitivity of Pd–Au sensors varies with composition.

A limitation in Paper V and Paper VI is that the nanoparticles were in contact with nothing but vacuum. In Paper VII, on the other hand, we studied monoelemental nanoparticles in aqueous environments with halides. The approach in this case was Wulff constructions, and it is non-trivial to transfer the methodology to atomistic models. To do so, models that incorporate the interaction with the environment would be required. While interatomic potentials such as EAM might be used, it is an arduous task to make models for many different materials and adsorbates, and high-throughput calculations would most likely be out of the question. Here, machine learning might come to the rescue [171, 172]. An alternative approach can be alloy cluster expansions, since they are in general more straight-forward to construct than off-lattice models. There are two different approaches to fit an alloy cluster expansion that incorporates adsorbate effects: include the adsorbates explicitly as another chemical species, or exclude the adsorbates from the cluster expansion but include their effect implicitly by training the cluster expansion with energies from calculations where they were included. There are examples of both approaches in the literature [125, 131, 173–175]. A challenge in either case is that it is rarely clear *a priori* which sites are energetically the most favorable for a given adsorbate and a given facet. This aspect makes it difficult to automatize the calculations to a sufficient extent, although machine learning approaches can simplify the problem somewhat [176].

Machine learning and artificial intelligence might also be useful in conjunction with the library of dielectric functions from Paper VIII. Currently, computational optimization of nanoplasmonic systems would typically require a trial-and-error approach, in which material (i.e., dielectric function) and geometry are chosen and an electrodynamic simulations are performed, and these steps are iterated until the desired optical response is obtained. It might be possible, for example, to train a neural network to take shortcuts between the choice of material/geometry and the optical response, and perhaps even automatically optimize material and geometry for a particular desired optical output.

For the hydrogen sensors specifically, there are multiple real-world challenges that have not been addressed in this thesis. For example, grain boundaries tend to mediate diffusion and thereby provide faster kinetics for hydrogen absorption. Together with variations in nanoparticle size and shape, this makes every nanoparticle unique in terms of its hydrogen absorption characteristics [12]. Another important aspect is that the sensors need to operate over long periods of time in the very challenging environment we know as air. The sensors will be exposed to, for example, moisture and reactive molecules such as CO that easily bind to the surface and block hydrogen uptake and release. Oxidation is a similar issue. Some of these challenges can be tackled by

embedding the nanoparticles in plastic using 3D printing techniques [177, 178] while CO poisoning can be mitigated by alloying with Cu [7]. Long-term operation can, however, be particularly challenging for multi-component alloys, since, for example, surface segregation can occur over time, changing the response of the material to both hydrogen exposure and light. Detailed atomic-scale understanding of the Pd–Au–Cu–H system is thus desirable, preferably in terms of both its thermodynamics [131] and its optical properties at the nanoscale and in bulk. This is by no means an easy task, but hopefully the work presented in this thesis can lead the way. The alloy at the end of the rainbow is within reach.

Acknowledgments

This thesis was meant to be written in the creative environment that is a university, in Sweden as well as abroad, but the COVID-19 pandemic upended all such plans. The fact that research can be performed almost equally well from a corner of my apartment is testament to the tremendous accomplishments in theoretical physics, computational methods, hardware, software and the Internet over the last centuries and decades. The feeling that it almost seems a little silly to point this out only goes to show the incredible speed at which this development has happened. Standing on the shoulders of giants has never been easier. But my giants are not only Newton, Lovelace, and Einstein. Regardless of whether I have been in the office, at home, or somewhere else, I have always had the best of support.

I want to express my deepest gratitude to my supervisor Paul Erhart for providing a perfect mix between supervision, independence, enjoyable and interesting conversations about everything from magpies to Dolly Parton, and Oxford commas. Your importance for this thesis cannot be overstated. My examiner Göran Wahnström has also been incredibly important and made sure that my work has been not only possible but also pleasant. I also want to thank my assistant supervisors Anders Hellman, Christoph Langhammer, and Kasper Moth-Poulsen for providing a backup plan that I wish I could have tried in parallel.

All current and former members of the Condensed Matter and Materials Theory division made these five years great, and for that I am forever grateful. I hope we can all meet off-Zoom again very soon. A special shout-out to Joakim who without complaints provided DFT energies for even the most obscure atomic structures, to Tuomas who patiently guided me through everything related to electrons, and to Mattias, William, Erik and the other developers of ICET who made sure that the calculations ran smoothly in spite of the sometimes picky user base.

My work was funded by the Swedish Foundation for Strategic Research (grant number RMA15-0052). I want to thank all members of the Plastic Plasmonics project, who widened my perspectives and showed that nanoparticles exist outside of my computer. I also want to thank the members of the Chemical Physics division, especially Christopher, Ferry, and Sara who co-authored Paper VIII, showing that not all of my calculations are nonsense.

While some may still be under the impression that my research is somehow related to the gold inside computers (which I suppose is in some sense true), I could not have done this without the support from my friends. You are all great! I especially want to thank Jonatan for listening with seemingly genuine interest to everything from order-disorder transitions via shin splints to subspecies of crow, and Björn for being a reliable and obviously Spanish-speaking friend. I also want to thank Johanna for being *min kompis* and a worthy contender in both tennis and Alfapet, and for showing exceptional interest in my thesis (at least this page). Finally, thank you for the amazing show and you look beautiful tonight and 12 points go to Alexander, Louise and Astrid for taking me through life in general and the pandemic in particular.

Till sist, världens största kram till mamma, pappa, Sofia, Niklas, Ellie, Vilma, Anna, Daniel, Siri och Alice. Ni är bäst!

Bibliography

[1] S. Chu, Y. Cui, and N. Liu, *The path towards sustainable energy,* Nature Materials **16**, 16 (2017). doi:10.1038/nmat4834.

[2] J. H. Montoya, L. C. Seitz, P. Chakthranont, A. Vojvodic, T. F. Jaramillo, and J. K. Nørskov, *Materials for solar fuels and chemicals,* Nature Materials **16**, 70 (2017). doi:10.1038/nmat4778.

[3] G. Glenk and S. Reichelstein, *Economics of converting renewable power to hydrogen,* Nature Energy **4**, 216 (2019).

[4] W.-T. Koo, H.-J. Cho, D.-H. Kim, Y. H. Kim, H. Shin, R. M. Penner, and I.-D. Kim, *Chemiresistive Hydrogen Sensors: Fundamentals, Recent Advances, and Challenges,* ACS Nano **14**, 14284 (2020). doi:10.1021/acsnano.0c05307.

[5] C. Wadell, F. A. A. Nugroho, E. Lidström, B. Iandolo, J. B. Wagner, and C. Langhammer, *Hysteresis-Free Nanoplasmonic Pd–Au Alloy Hydrogen Sensors,* Nano Letters **15**, 3563 (2015). doi:10.1021/acs.nanolett.5b01053.

[6] N. Isaac, P. Ngene, R. Westerwaal, J. Gaury, B. Dam, A. Schmidt-Ott, and G. Biskos, *Optical hydrogen sensing with nanoparticulate Pd–Au films produced by spark ablation,* Sensors and Actuators B: Chemical **221**, 290 (2015). doi:10.1016/j.snb.2015.05.095.

[7] I. Darmadi, F. A. A. Nugroho, S. Kadkhodazadeh, J. B. Wagner, and C. Langhammer, *Rationally Designed PdAuCu Ternary Alloy Nanoparticles for Intrinsically Deactivation-Resistant Ultrafast Plasmonic Hydrogen Sensing,* ACS Sensors **4**, 1424 (2019). doi:10.1021/acssensors.9b00610.

[8] K. J. Palm, J. B. Murray, J. P. McClure, M. S. Leite, and J. N. Munday, *In Situ Optical and Stress Characterization of Alloyed Pd_xAu_{1-x} Hydrides,* ACS Applied Materials & Interfaces **11**, 45057 (2019). doi:10.1021/acsami.9b14244.

[9] F. A. A. Nugroho, I. Darmadi, V. P. Zhdanov, and C. Langhammer, *Universal Scaling and Design Rules of Hydrogen-Induced Optical Properties in Pd and Pd-Alloy Nanoparticles,* ACS Nano **12**, 9903 (2018). doi:10.1021/acsnano.8b02835.

[10] C. Wadell, S. Syrenova, and C. Langhammer, *Plasmonic Hydrogen Sensing with Nanostructured Metal Hydrides,* ACS Nano **8**, 11925 (2014). doi:10.1021/nn505804f.

[11] I. Darmadi, F. A. A. Nugroho, and C. Langhammer, *High-Performance Nanostructured Palladium-Based Hydrogen Sensors: Current Limitations and Strategies for Their Mitigation,* ACS Sensors **5**, 3306 (2020). doi:10.1021/acssensors.0c02019.

[12] S. Alekseeva, A. B. da Silva Fanta, B. Iandolo, T. J. Antosiewicz, F. A. A. Nugroho, J. B. Wagner, A. Burrows, V. P. Zhdanov, and C. Langhammer, *Grain boundary mediated hydriding phase transformations in individual polycrystalline metal nanoparticles,* Nature Communications **8**, 1 (2017). doi:10.1038/s41467-017-00879-9.

[13] F. A. Nugroho, I. Darmadi, L. Cusinato, A. Susarrey-Arce, H. Schreuders, L. J. Bannenberg, A. B. da Silva Fanta, S. Kadkhodazadeh, J. B. Wagner, T. J. Antosiewicz, A. Hellman, V. P. Zhdanov, B. Dam, and C. Langhammer, *Metal–polymer hybrid nanomaterials for plasmonic ultrafast hydrogen detection,* Nature Materials **18**, 489 (2019). doi:10.1038/s41563-019-0325-4.

[14] A. Johanson and W. Hasselbring, *Software Engineering for Computational Science: Past, Present, Future,* Computing in Science Engineering **20**, 90 (2018). doi:10.1109/MCSE.2018.021651343.

[15] H. B. Callen, *Thermodynamics and an Introduction to Thermostatistics* (New York: Wiley, 1985).

[16] P. Subramanian and J. Perepezko, *The Ag-Cu (silver-copper) system,* Journal of Phase Equilibria **14**, 62 (1993). doi:10.1007/BF02652162.

[17] H. Okamoto and T. Massalski, *The Au–Pd (Gold-Palladium) system,* Bulletin of Alloy Phase Diagrams **6**, 229 (1985). doi:10.1007/BF02880404.

[18] C. Bale, E. Bélisle, P. Chartrand, S. Decterov, G. Eriksson, A. Gheribi, K. Hack, I.-H. Jung, Y.-B. Kang, J. Melançon, A. Pelton, S. Petersen, C. Robelin, J. Sangster, P. Spencer, and M.-A. Van Ende, *FactSage thermochemical software and databases, 2010–2016,* Calphad **54**, 35 (2016). www.factsage.com. doi:10.1016/j.calphad.2016.05.002.

[19] H. Okamoto, D. Chakrabarti, D. Laughlin, and T. Massalski, *The Au–Cu (Gold-Copper) system,* Journal of Phase Equilibria **8**, 454 (1987). doi:10.1007/BF02893155.

[20] Y. Matsuo, A. Nagasawa, and J. Kakinoki, *Ordered Alloys of the Gold-Palladium System. II. Electron Diffraction Study on Evaporated $AuPd_3$ Films,* Journal of the Physical Society of Japan **21**, 2633 (1966). doi:10.1143/JPSJ.21.2633.

[21] Y. Kawasaki, S. Ino, and S. Ogawa, *Electron Diffraction Study on the Superlattice Formation in the Gold-Palladium Alloy System,* Journal of the Physical Society of Japan **30**, 1758 (1971). doi:10.1143/JPSJ.30.1758.

[22] S.-M. Lee, H. Noh, T. B. Flanagan, and S. Luo, *Hydrogen-induced lattice rearrangement of a $Pd_{0.81}Au_{0.19}$ alloy,* Journal of Physics: Condensed Matter **19**, 326222 (2007). doi:10.1088/0953-8984/19/32/326222.

[23] W. Hume-Rothery, *Researches on the nature, properties, and conditions of formation of intermetallic compounds, with special reference to certain compounds of tin*. PhD thesis, University of London, 1926.

[24] N. W. Ashcroft and N. D. Mermin, *Solid State Physics* (Philadelphia: Saunders, 1976).

[25] A. Allred, *Electronegativity values from thermochemical data,* Journal of Inorganic and Nuclear Chemistry **17**, 215 (1961). doi:10.1016/0022-1902(61)80142-5.

[26] H. Okamoto, M. Schlesinger, and E. Mueller, *Alloy Phase Diagrams* (Materials Park, Ohio: ASM International, 2016). doi:10.31399/asm.hb.v03.9781627081634.

[27] T. Korhonen, M. J. Puska, and R. M. Nieminen, *Vacancy-formation energies for fcc and bcc transition metals,* Phys. Rev. B **51**, 9526 (1995). doi:10.1103/PhysRevB.51.9526.

[28] L. Schlapbach and A. Züttel, *Hydrogen-storage materials for mobile applications,* Nature **414**, 353 (2001). doi:10.1038/35104634.

[29] A. Schneemann, J. L. White, S. Kang, S. Jeong, L. F. Wan, E. S. Cho, T. W. Heo, D. Prendergast, J. J. Urban, B. C. Wood, M. D. Allendorf, and V. Stavila, *Nanostructured Metal Hydrides for Hydrogen Storage,* Chemical Reviews **118**, 10775 (2018). doi:10.1021/acs.chemrev.8b00313.

[30] A. Sieverts, *Absorption of gases by metals,* Zeitschrift für Metallkunde **21**, 37 (1929).

[31] Y. Fukai, *The Metal-Hydrogen System: Basic Bulk Properties* (Berlin Heidelberg: Springer, 2006).

[32] E. Fromm and G. Hörz, *Hydrogen, nitrogen, oxygen, and carbon in metals,* International Metals Reviews **25**, 269 (1980). doi:10.1179/imtr.1980.25.1.269.

[33] C. Boelsma, L. Bannenberg, M. Van Setten, N.-J. Steinke, A. Van Well, and B. Dam, *Hafnium—an optical hydrogen sensor spanning six orders in pressure,* Nature Communications **8**, 1 (2017). doi:10.1038/ncomms15718.

[34] R. Griessen and T. Riesterer, *Heat of formation models*. In L. Schlapbach, ed., *Hydrogen in Intermetallic Compounds I: Electronic, Thermodynamic, and Crystallographic Properties, Preparation* (Berlin Heidelberg: Springer, 1988). doi:10.1007/3540183337_13.

[35] A. Maeland and T. B. Flanagan, *X-Ray and Thermodynamic Studies of the Absorption of Hydrogen by Gold-Palladium Alloys,* The Journal of Physical Chemistry **69**, 3575 (1965). doi:10.1021/j100894a054.

[36] S. Luo, D. Wang, and T. B. Flanagan, *Thermodynamics of Hydrogen in fcc Pd-Au Alloys,* The Journal of Physical Chemistry B **114**, 6117 (2010). doi:10.1021/jp100858r.

[37] Y. Sakamoto, S. Hirata, and H. Nishikawa, *Diffusivity and solubility of hydrogen in Pd-Ag and Pd-Au alloys,* Journal of the Less Common Metals **88**, 387 (1982). doi:10.1016/0022-5088(82)90247-8.

[38] A. Hultgren, *Isothermal transformation of austenite,* Transactions of the American Society for Metals **39**, 915 (1947).

[39] M. Hillert and J. Ågren, *On the definitions of paraequilibrium and orthoequilibrium,* Scripta Materialia **50**, 697 (2004). doi:10.1016/j.scriptamat.2003.11.020.

[40] T. B. Flanagan, A. Craft, T. Kuji, K. Baba, and Y. Sakamoto, *Hydrogen induced disorder-order transition in Pd_3Mn,* Scripta Metallurgica **20**, 1745 (1986). doi:10.1016/0036-9748(86)90281-4.

[41] J. W. Cahn, *Coherent fluctuations and nucleation in isotropic solids,* Acta Metallurgica **10**, 907 (1962). doi:10.1016/0001-6160(62)90140-2.

[42] R. Williams, *Long-period superlattices in the copper-gold system as two-phase mixtures,* Metallurgical Transactions A **11**, 247 (1980). doi:10.1007/BF02660629.

[43] R. Williams, *The calculation of coherent phase equilibria,* Calphad **8**, 1 (1984). doi:10.1016/0364-5916(84)90024-5.

[44] J. Cahn and F. Larché, *A simple model for coherent equilibrium,* Acta Metallurgica **32**, 1915 (1984). doi:10.1016/0001-6160(84)90173-1.

[45] R. Griessen, N. Strohfeldt, and H. Giessen, *Thermodynamics of the hybrid interaction of hydrogen with palladium nanoparticles,* Nature Materials **15**, 311 (2016). doi:10.1038/nmat4480.

[46] A. Ulvestad, M. Welland, W. Cha, Y. Liu, J. Kim, R. Harder, E. Maxey, J. Clark, M. Highland, H. You, P. Zapol, S. Hruszkewycz, and G. Stephenson, *Three-dimensional imaging of dislocation dynamics during the hydriding phase transformation,* Nature Materials **16**, 565 (2017). doi:10.1038/nmat4842.

[47] T. C. Narayan, F. Hayee, A. Baldi, A. L. Koh, R. Sinclair, and J. A. Dionne, *Direct visualization of hydrogen absorption dynamics in individual palladium nanoparticles,* Nature Communications **8**, 1 (2017). doi:10.1038/ncomms14020.

[48] R. B. Schwarz and A. G. Khachaturyan, *Thermodynamics of Open Two-Phase Systems with Coherent Interfaces,* Physical Review Letters **74**, 2523 (1995). doi:10.1103/PhysRevLett.74.2523.

[49] R. Schwarz and A. Khachaturyan, *Thermodynamics of open two-phase systems with coherent interfaces: Application to metal–hydrogen systems,* Acta Materialia **54**, 313 (2006). doi:10.1016/j.actamat.2005.08.044.

[50] E. Wicke and J. Blaurock, *New experiments on and interpretations of hysteresis effects of Pd-D_2 and Pd-H_2,* Journal of the Less Common Metals **130**, 351 (1987). doi:10.1016/0022-5088(87)90129-9.

[51] E. Ho, H. A. Goldberg, G. C. Weatherly, and F. D. Manchester, *An in situ electron microscope study of precipitation in palladium-hydrogen alloys,* Acta Metallurgica **27**, 841 (1979). doi:10.1016/0001-6160(79)90119-6.

[52] K. Sytwu, F. Hayee, T. C. Narayan, A. L. Koh, R. Sinclair, and J. A. Dionne, *Visualizing Facet-Dependent Hydrogenation Dynamics in Individual Palladium Nanoparticles,* Nano Letters **18**, 5357 (2018). doi:10.1021/acs.nanolett.8b00736.

[53] G. Wulff, *Zur Frage der Geschwindigkeit des Wachstums und der Auflösung der Krystallflächen,* Zeitschrift für Kristallographie **34**, 449 (1901). doi:10.1524/zkri.1901.34.1.449.

[54] L. Marks and L. Peng, *Nanoparticle shape, thermodynamics and kinetics,* Journal of Physics: Condensed Matter **28**, 053001 (2016). doi:10.1088/0953-8984/28/5/053001.

[55] J. Löfgren, *Modeling Collodial Nanoparticles: From Growth to Deposition*. PhD Thesis, Chalmers University of Technology, 2019.

[56] A. R. Roosen, R. P. McCormack, and W. Carter, *Wulffman: A tool for the calculation and display of crystal shapes,* Computational Materials Science **11**, 16 (1998). doi:10.1016/S0927-0256(97)00167-5.

[57] H. M. Cundy and A. P. Rollett, *Mathematical Models* (Oxford: Oxford University Press, 1961).

[58] C. B. Barber, D. P. Dobkin, and H. Huhdanpaa, *The Quickhull Algorithm for Convex Hulls,* ACM Transactions on Mathematical Software **22**, 469–483 (1996). doi:10.1145/235815.235821.

[59] P. Virtanen, R. Gommers, T. E. Oliphant, M. Haberland, T. Reddy, D. Cournapeau, E. Burovski, P. Peterson, W. Weckesser, J. Bright, S. J. van der Walt, M. Brett, J. Wilson, K. J. Millman, N. Mayorov, A. R. J. Nelson, E. Jones, R. Kern, E. Larson, C. J. Carey, İ. Polat, Y. Feng, E. W. Moore, J. VanderPlas, D. Laxalde, J. Perktold, R. Cimrman, I. Henriksen, E. A. Quintero, C. R. Harris, A. M. Archibald, A. H. Ribeiro, F. Pedregosa, P. van Mulbregt, and SciPy 1.0 Contributors, *SciPy 1.0: Fundamental Algorithms for Scientific Computing in Python,* Nature Methods **17**, 261 (2020). doi:10.1038/s41592-019-0686-2.

[60] W. L. Winterbottom, *Equilibrium shape of a small particle in contact with a foreign substrate,* Acta Metallurgica **15**, 303 (1967). doi:10.1016/0001-6160(67)90206-4.

[61] L. D. Marks, *Modified Wulff constructions for twinned particles,* Journal of Crystal Growth **61**, 556 (1983). doi:10.1016/0022-0248(83)90184-7.

[62] S. Zhou, M. Zhao, T.-H. Yang, and Y. Xia, *Decahedral nanocrystals of noble metals: Synthesis, characterization, and applications,* Materials Today **22**, 108 (2019). doi:10.1016/j.mattod.2018.04.003.

[63] S. Ino, *Epitaxial Growth of Metals on Rocksalt Faces Cleaved in Vacuum. II. Orientation and Structure of Gold Particles Formed in Ultrahigh Vacuum,* Journal of the Physical Society of Japan **21**, 346 (1966). doi:10.1143/JPSJ.21.346.

[64] S. Ino and S. Ogawa, *Multiply Twinned Particles at Earlier Stages of Gold Film Formation on Alkalihalide Crystals,* Journal of the Physical Society of Japan **22**, 1365 (1967). doi:10.1143/JPSJ.22.1365.

[65] L. D. Marks, *Surface structure and energetics of multiply twinned particles,* Philosophical Magazine A **49**, 81 (1984). doi:10.1080/01418618408233431.

[66] D. J. Smith and L. Marks, *High resolution studies of small particles of gold and silver: II. Single crystals, lamellar twins and polyparticles,* Journal of Crystal Growth **54**, 433 (1981). doi:10.1016/0022-0248(81)90495-4.

[67] G. Rossi, A. Rapallo, C. Mottet, A. Fortunelli, F. Baletto, and R. Ferrando, *Magic Polyicosahedral Core-Shell Clusters,* Physical Review Letters **93**, 105503 (2004). doi:10.1103/PhysRevLett.93.105503.

[68] K. Kimoto and I. Nishida, *An electron microscope and electron diffraction study of fine smoke particles prepared by evaporation in argon gas at low pressures (II),* Japanese Journal of Applied Physics **6**, 1047 (1967). doi:10.1143/JJAP.6.1047.

[69] M. Grzelczak, J. Pérez-Juste, P. Mulvaney, and L. M. Liz-Marzán, *Shape control in gold nanoparticle synthesis,* Chemical Society Reviews **37**, 1783 (2008). doi:10.1039/B711490G.

[70] Y. Sun and Y. Xia, *Shape-Controlled Synthesis of Gold and Silver Nanoparticles,* Science **298**, 2176 (2002). doi:10.1126/science.1077229.

[71] T. K. Sau and C. J. Murphy, *Room Temperature, High-Yield Synthesis of Multiple Shapes of Gold Nanoparticles in Aqueous Solution,* Journal of the American Chemical Society **126**, 8648 (2004). doi:10.1021/ja047846d.

[72] N. R. Jana, L. Gearheart, and C. J. Murphy, *Seed-Mediated Growth Approach for Shape-Controlled Synthesis of Spheroidal and Rod-like Gold Nanoparticles Using a Surfactant Template,* Advanced Materials **13**, 1389 (2001). doi:10.1002/1521-4095(200109)13:18<1389::AID-ADMA1389>3.0.CO;2-F.

[73] S. E. Skrabalak, J. Chen, Y. Sun, X. Lu, L. Au, C. M. Cobley, and Y. Xia, *Gold Nanocages: Synthesis, Properties, and Applications,* Accounts of Chemical Research **41**, 1587 (2008). doi:10.1021/ar800018v.

[74] F. Baletto, R. Ferrando, A. Fortunelli, F. Montalenti, and C. Mottet, *Crossover among structural motifs in transition and noble-metal clusters,* The Journal of Chemical Physics **116**, 3856 (2002). doi:10.1063/1.1448484.

[75] K. P. McKenna, *Gold nanoparticles under gas pressure,* Physical Chemistry Chemical Physics **11**, 4145 (2009). doi:10.1039/B821408P.

[76] A. S. Barnard, N. P. Young, A. I. Kirkland, M. A. van Huis, and H. Xu, *Nanogold: A Quantitative Phase Map,* ACS Nano **3**, 1431 (2009). doi:10.1021/nn900220k.

[77] H. Li, L. Li, A. Pedersen, Y. Gao, N. Khetrapal, H. Jónsson, and X. C. Zeng, *Magic-number gold nanoclusters with diameters from 1 to 3.5 nm: Relative stability and catalytic activity for CO oxidation,* Nano Letters **15**, 682 (2015). doi:10.1021/nl504192u.

[78] S. Plimpton, *Fast Parallel Algorithms for Short-Range Molecular Dynamics,* Journal of Computational Physics **117**, 1 (1995). doi:10.1006/jcph.1995.1039.

[79] Y. Mishin, M. J. Mehl, D. A. Papaconstantopoulos, A. F. Voter, and J. D. Kress, *Structural stability and lattice defects in copper: Ab initio, tight-binding, and embedded-atom calculations,* Physical Review B **63**, 224106 (2001). doi:10.1103/PhysRevB.63.224106.

[80] E. Ringe, R. P. Van Duyne, and L. D. Marks, *Wulff Construction for Alloy Nanoparticles,* Nano Letters **11**, 3399 (2011). doi:10.1021/nl2018146.

[81] J. Pohl, C. Stahl, and K. Albe, *Size-dependent phase diagrams of metallic alloys: A Monte Carlo simulation study on order-disorder transitions in Pt-Rh nanoparticles,* Beilstein Jorunal of Nanotechnology **3**, 1 (2012). doi:10.3762/bjnano.3.1.

[82] G. Guisbiers, R. Mendoza-Cruz, L. Bazán-Díaz, J. J. Velázquez-Salazar, R. Mendoza-Perez, J. A. Robledo-Torres, J. L. Rodriguez-Lopez, J. M. Montejano-Carrizales, R. L. Whetten, and M. José-Yacamán, *Electrum, the gold-silver alloy, from the bulk scale to the nanoscale: Synthesis, properties, and segregation rules,* ACS Nano **10**, 188 (2016). doi:10.1021/acsnano.5b05755.

[83] M. Chu, Y. Qin, T. Xiao, W. Shen, T. Su, C. Hu, and C. Tang, *Thermodynamic reassessment of the Ag–Cu phase diagram at nano-scale,* Calphad **72**, 102233 (2021). doi:10.1016/j.calphad.2020.102233.

[84] G. Guisbiers, S. Mejia-Rosales, S. Khanal, F. Ruiz-Zepeda, R. L. Whetten, and M. José-Yacaman, *Gold–Copper Nano-Alloy, "Tumbaga", in the Era of Nano: Phase Diagram and Segregation,* Nano Letters **14**, 6718 (2014). doi:10.1021/nl503584q.

[85] G. Guisbiers, R. Mendoza-Pérez, L. Bazán-Díaz, R. Mendoza-Cruz, J. J. Velázquez-Salazar, and M. José-Yacamán, *Size and Shape Effects on the Phase Diagrams of Nickel-Based Bimetallic Nanoalloys,* The Journal of Physical Chemistry C **121**, 6930 (2017). doi:10.1021/acs.jpcc.6b09115.

[86] Y. Yang, C.-c. Chen, M. C. Scott, C. Ophus, R. Xu, A. P. Jr, L. Wu, F. Sun, W. Theis, J. Zhou, M. Eisenbach, P. R. C. Kent, R. F. Sabirianov, H. Zeng, P. Ercius, and J. Miao, *Deciphering chemical order/disorder and material properties at the single-atom level,* Nature **542**, 75 (2017). doi:10.1038/nature21042.

[87] R. Ferrando, J. Jellinek, and R. L. Johnston, *Nanoalloys: From Theory to Applications of Alloy Clusters and Nanoparticles,* Chemical Reviews **108**, 845 (2008). doi:10.1021/cr040090g.

[88] R. Ferrando, *Symmetry breaking and morphological instabilities in core-shell metallic nanoparticles,* Journal of Physics: Condensed Matter **27**, 013003 (2014). doi:10.1088/0953-8984/27/1/013003.

[89] F. Baletto, *Modelling Janus Nanoparticles*. In M. M. Mariscal, O. A. Oviedo, and E. P. M. Leiva, eds., *Metal Clusters and Nanoalloys: From Modeling to Applications* (New York: Springer, 2013). doi:10.1007/978-1-4614-3643-0_8.

[90] F. Negreiros, L. Sementa, G. Barcaro, I. Fechete, L. Piccolo, and A. Fortunelli, *Reactivity and Catalysis by Nanoalloys*. In F. Calvo, ed., *Nanoalloys: From Fundamentals to Emergent Applications* (Oxford: Elsevier, 2020). doi:10.1016/B978-0-12-819847-6.00014-0.

[91] D. J. Griffiths, *Introduction to Electrodynamics* (New Jersey: Prentice Hall, 2005).

[92] C. F. Bohren and D. R. Huffman, *Absorption and Scattering of Light by Small Particles* (New York: John Wiley & Sons, 2008).

[93] T. Rossi, *Computational modeling of quantum aspects in plasmonic nanostructures*. PhD thesis, Aalto University, 2017. http://urn.fi/URN:ISBN:978-952-60-7586-0.

[94] C. A. Ullrich, *Time-Dependent Density-Functional Theory: Concepts and Applications* (New York: Oxford University Press, 2012).

[95] E. A. Stern, *Rigid-Band Model of Alloys,* Physical Review **157**, 544 (1967). doi:10.1103/PhysRev.157.544.

[96] T. Gong, P. Lyu, K. J. Palm, S. Memarzadeh, J. N. Munday, and M. S. Leite, *Emergent Opportunities with Metallic Alloys: From Material Design to Optical Devices,* Advanced Optical Materials **8**, 2001082 (2020). doi:10.1002/adom.202001082.

[97] C. Kittel, *Introduction to Solid State Physics* (New York: Wiley, 2005).

[98] V. Popescu and A. Zunger, *Extracting E versus **k** effective band structure from supercell calculations on alloys and impurities,* Physical Review B **85**, 085201 (2012). doi:10.1103/PhysRevB.85.085201.

[99] J. J. Mortensen, L. B. Hansen, and K. W. Jacobsen, *Real-space grid implementation of the projector augmented wave method,* Physical Review B **71**, 035109 (2005). doi:10.1103/PhysRevB.71.035109.

[100] J. Enkovaara, C. Rostgaard, J. J. Mortensen, J. Chen, M. Dułak, L. Ferrighi, J. Gavnholt, C. Glinsvad, V. Haikola, H. A. Hansen, H. H. Kristoffersen, M. Kuisma, A. H. Larsen, L. Lehtovaara, M. Ljungberg, O. Lopez-Acevedo, P. G. Moses, J. Ojanen, T. Olsen, V. Petzold, N. A. Romero, J. Stausholm-Møller, M. Strange, G. A. Tritsaris, M. Vanin, M. Walter, B. Hammer, H. Häkkinen, G. K. H. Madsen, R. M. Nieminen, J. K. Nørskov, M. Puska, T. T. Rantala, J. Schiøtz, K. S. Thygesen, and K. W. Jacobsen, *Electronic structure calculations with GPAW: a real-space implementation of the projector augmented-wave method,* Journal of Physics: Condensed Matter **22**, 253202 (2010). doi:10.1088/0953-8984/22/25/253202.

[101] P. Hohenberg and W. Kohn, *Inhomogeneous Electron Gas,* Physical Review **136**, B864 (1964). doi:10.1103/PhysRev.136.B864.

[102] W. Kohn and L. J. Sham, *Self-Consistent Equations Including Exchange and Correlation Effects,* Physical Review **140**, A1133 (1965). doi:10.1103/PhysRev.140.A1133.

[103] E. Runge and E. K. U. Gross, *Density-Functional Theory for Time-Dependent Systems,* Physical Review Letters **52**, 997 (1984). doi:10.1103/PhysRevLett.52.997.

[104] D. A. Strubbe, L. Lehtovaara, A. Rubio, M. A. L. Marques, and S. G. Louie, *Response Functions in TDDFT: Concepts and Implementation*. In M. A. Marques, N. T. Maitra, F. M.

Nogueira, E. Gross, and A. Rubio, eds., *Fundamentals of Time-Dependent Density Functional Theory* (Berlin Heidelberg: Springer, 2012). doi:10.1007/978-3-642-23518-4_7.

[105] J. Yan, J. J. Mortensen, K. W. Jacobsen, and K. S. Thygesen, *Linear density response function in the projector augmented wave method: Applications to solids, surfaces, and interfaces,* Physical Review B **83**, 245122 (2011). doi:10.1103/PhysRevB.83.245122.

[106] E. B. Tadmor and R. E. Miller, *Modeling Materials: Continuum, Atomistic and Multiscale Techniques* (Cambridge, England: Cambridge University Press, 2011).

[107] M. S. Daw, S. M. Foiles, and M. I. Baskes, *The embedded-atom method: a review of theory and applications,* Materials Science Reports **9**, 251 (1993). doi:10.1016/0920-2307(93)90001-U.

[108] M. S. Daw and M. I. Baskes, *Embedded-atom method: Derivation and application to impurities, surfaces, and other defects in metals,* Physical Review B **29**, 6443 (1984). doi:10.1103/PhysRevB.29.6443.

[109] J. K. Nørskov and N. D. Lang, *Effective-medium theory of chemical binding: Application to chemisorption,* Physical Review B **21**, 2131 (1980). doi:10.1103/PhysRevB.21.2131.

[110] K. W. Jacobsen, J. K. Nørskov, and M. J. Puska, *Interatomic interactions in the effective-medium theory,* Physical Review B **35**, 7423 (1987). doi:10.1103/PhysRevB.35.7423.

[111] M. W. Finnis and J. E. Sinclair, *A simple empirical N-body potential for transition metals,* Philosophical Magazine A **50**, 45 (1984). doi:10.1080/01418618408244210.

[112] F. Ercolessi, E. Tosatti, and M. Parrinello, *Au (100) Surface Reconstruction,* Physical Review Letters **57**, 719 (1986). doi:10.1103/PhysRevLett.57.719.

[113] M. J. Stott and E. Zaremba, *Quasiatoms: An approach to atoms in nonuniform electronic systems,* Physical Review B **22**, 1564 (1980). doi:10.1103/PhysRevB.22.1564.

[114] A. van de Walle and G. Ceder, *The effect of lattice vibrations on substitutional alloy thermodynamics,* Reviews of Modern Physics **74**, 11 (2002). doi:10.1103/RevModPhys.74.11.

[115] J. Sanchez, F. Ducastelle, and D. Gratias, *Generalized cluster description of multicomponent systems,* Physica A: Statistical Mechanics and its Applications **128**, 334 (1984). doi:10.1016/0378-4371(84)90096-7.

[116] J. M. Sanchez, *Cluster expansion and the configurational theory of alloys,* Physical Review B **81**, 224202 (2010). doi:10.1103/PhysRevB.81.224202.

[117] F. Santosa and W. W. Symes, *Linear Inversion of Band-Limited Reflection Seismograms,* SIAM Journal on Scientific and Statistical Computing **7**, 1307 (1986). doi:10.1137/0907087.

[118] R. Tibshirani, *Regression Shrinkage and Selection Via the Lasso,* Journal of the Royal Statistical Society: Series B (Methodological) **58**, 267 (1996). doi:10.1111/j.2517-6161.1996.tb02080.x.

[119] L. J. Nelson, V. Ozoliņš, C. S. Reese, F. Zhou, and G. L. W. Hart, *Cluster expansion made easy with Bayesian compressive sensing,* Physical Review B **88**, 155105 (2013). doi:10.1103/PhysRevB.88.155105.

[120] M. Ångqvist and P. Erhart, *Understanding Chemical Ordering in Intermetallic Clathrates from Atomic Scale Simulations,* Chemistry of Materials **29**, 7554 (2017). doi:10.1021/acs.chemmater.7b02686.

[121] M. Ångqvist, J. M. Rahm, L. Gharaee, and P. Erhart, *Structurally driven asymmetric miscibility in the phase diagram of W-Ti,* Physical Review Materials **3**, 073605 (2019). doi:10.1103/PhysRevMaterials.3.073605.

[122] J. H. Chang, D. Kleiven, M. Melander, J. Akola, J. M. Garcia-Lastra, and T. Vegge, *CLEASE: a versatile and user-friendly implementation of cluster expansion method,* Journal of Physics: Condensed Matter **31**, 325901 (2019). doi:10.1088/1361-648X/ab1bbc.

[123] T. Mueller and G. Ceder, *Bayesian approach to cluster expansions,* Phys. Rev. B **80**, 024103 (2009). doi:10.1103/PhysRevB.80.024103.

[124] J. A. Rice, *Mathematical Statistics and Data Analysis* (Belmont, California: Brooks/Cole, 2007).

[125] L. Cao, C. Li, and T. Mueller, *The Use of Cluster Expansions To Predict the Structures and Properties of Surfaces and Nanostructured Materials,* Journal of Chemical Information and Modeling **58**, 2401 (2018). doi:10.1021/acs.jcim.8b00413.

[126] D. J. C. MacKay, *Bayesian Non-Linear Modeling for the Prediction Competition*. In G. R. Heidbreder, ed., *Maximum Entropy and Bayesian Methods* (Dordrecht: Springer Netherlands, 1996). doi:10.1007/978-94-015-8729-7_18.

[127] E. Fransson, F. Eriksson, and P. Erhart, *Efficient construction of linear models in materials modeling and applications to force constant expansions,* npj Computational Materials **6**, 135 (2020). doi:10.1038/s41524-020-00404-5.

[128] J. Goodman and J. Weare, *Ensemble samplers with affine invariance,* Communications in Applied Mathematics and Computational Science **5**, 65 (2010). doi:10.2140/camcos.2010.5.65.

[129] S. V. Barabash, V. Blum, S. Müller, and A. Zunger, *Prediction of unusual stable ordered structures of Au-Pd alloys via a first-principles cluster expansion,* Physical Review B **74**, 035108 (2006). doi:10.1103/PhysRevB.74.035108.

[130] W. Huang, A. Urban, Z. Rong, Z. Ding, C. Luo, and G. Ceder, *Construction of ground-state preserving sparse lattice models for predictive materials simulations,* npj Computational Materials **3**, 1 (2017). doi:10.1038/s41524-017-0032-0.

[131] P. Ekborg-Tanner and P. Erhart, *Hydrogen-driven Surface Segregation in Pd-alloys: Revealing the Layer-by-layer Composition of AuPd, CuPd and AuCuPd by Atomic Scale Simulations,* (unpublished).

[132] T. Mueller and G. Ceder, *Exact expressions for structure selection in cluster expansions,* Physical Review B **82**, 184107 (2010). doi:10.1103/PhysRevB.82.184107.

[133] D. Kleiven, J. Akola, A. Peterson, T. Vegge, and J. H. Chang, *Generating training set based on uncertainty estimations for cluster expansion method,* Journal of Physics: Energy (in press). doi:10.1088/2515-7655/abf9ef.

[134] K. Shinohara, A. Seko, T. Horiyama, M. Ishihata, J. Honda, and I. Tanaka, *Enumeration of nonequivalent substitutional structures using advanced data structure of binary decision diagram,* The Journal of Chemical Physics **153**, 104109 (2020). doi:10.1063/5.0021663.

[135] S. Mustapha, P. D'Arco, M. D. L. Pierre, Y. Noël, M. Ferrabone, and R. Dovesi, *On the use of symmetry in configurational analysis for the simulation of disordered solids,* Journal of Physics: Condensed Matter **25**, 105401 (2013). doi:10.1088/0953-8984/25/10/105401.

[136] G. L. W. Hart and R. W. Forcade, *Algorithm for generating derivative structures,* Physical Review B **77**, 224115 (2008). doi:10.1103/PhysRevB.77.224115.

[137] G. L. W. Hart and R. W. Forcade, *Generating derivative structures from multilattices: Algorithm and application to hcp alloys,* Physical Review B **80**, 014120 (2009). doi:10.1103/PhysRevB.80.014120.

[138] G. L. W. Hart, *Where are nature's missing structures?,* Nature Materials **6**, 941 (2007). doi:10.1038/nmat2057.

[139] A. Zunger, S.-H. Wei, L. G. Ferreira, and J. E. Bernard, *Special quasirandom structures,* Physical Review Letters **65**, 353 (1990). doi:10.1103/PhysRevLett.65.353.

[140] A. van de Walle, P. Tiwary, M. De Jong, D. L. Olmsted, M. Asta, A. Dick, D. Shin, Y. Wang, L. Q. Chen, and Z. K. Liu, *Efficient stochastic generation of special quasirandom structures,* CALPHAD **42**, 13 (2013). doi:10.1016/j.calphad.2013.06.006.

[141] N. Metropolis, A. W. Rosenbluth, M. N. Rosenbluth, A. H. Teller, and E. Teller, *Equation of State Calculations by Fast Computing Machines,* The Journal of Chemical Physics **21**, 1087 (1953). doi:10.1063/1.1699114.

[142] A. van de Walle and M. Asta, *Self-driven lattice-model Monte Carlo simulations of alloy thermodynamic properties and phase diagrams,* Modelling and Simulation in Materials Science and Engineering **10**, 521 (2002). doi:10.1088/0965-0393/10/5/304.

[143] B. Sadigh and P. Erhart, *Calculation of excess free energies of precipitates via direct thermodynamic integration across phase boundaries,* Physical Review B **86**, 134204 (2012). doi:10.1103/PhysRevB.86.134204.

[144] B. Sadigh, P. Erhart, A. Stukowski, A. Caro, E. Martinez, and L. Zepeda-Ruiz, *Scalable parallel Monte Carlo algorithm for atomistic simulations of precipitation in alloys,* Physical Review B **85**, 184203 (2012). doi:10.1103/PhysRevB.85.184203.

[145] S. M. Woodley and R. Catlow, *Crystal structure prediction from first principles,* Nature Materials **7**, 937 (2008). doi:10.1038/nmat2321.

[146] S. Heiles and R. L. Johnston, *Global optimization of clusters using electronic structure methods,* International Journal of Quantum Chemistry **113**, 2091 (2013). doi:10.1002/qua.24462.

[147] M. Jäger, R. Schäfer, and R. L. Johnston, *First principles global optimization of metal clusters and nanoalloys,* Advances in Physics: X **3**, 1516514 (2018). doi:10.1080/23746149.2018.1516514.

[148] I. L. Garzón, K. Michaelian, M. R. Beltrán, A. Posada-Amarillas, P. Ordejón, E. Artacho, D. Sánchez-Portal, and J. M. Soler, *Lowest Energy Structures of Gold Nanoclusters,* Physical Review Letters **81**, 1600 (1998). doi:10.1103/PhysRevLett.81.1600.

[149] R. L. Johnston, *Evolving better nanoparticles: Genetic algorithms for optimising cluster geometries,* Dalton Transactions **22**, 4193 (2003). doi:10.1039/B305686D.

[150] D. J. Wales and J. P. Doye, *Global optimization by basin-hopping and the lowest energy structures of Lennard-Jones clusters containing up to 110 atoms,* The Journal of Physical Chemistry A **101**, 5111 (1997). doi:10.1021/jp970984n.

[151] E. Aprà, R. Ferrando, and A. Fortunelli, *Density-functional global optimization of gold nanoclusters,* Physical Review B **73**, 205414 (2006). doi:10.1103/PhysRevB.73.205414.

[152] X. Chen, Y.-F. Zhao, L.-S. Wang, and J. Li, *Recent progresses of global minimum searches of nanoclusters with a constrained Basin-Hopping algorithm in the TGMin program,* Computational and Theoretical Chemistry **1107**, 57 (2017). doi:10.1016/j.comptc.2016.12.028.

[153] S. Darby, T. V. Mortimer-Jones, R. L. Johnston, and C. Roberts, *Theoretical study of Cu–Au nanoalloy clusters using a genetic algorithm,* The Journal of Chemical Physics **116**, 1536 (2002). doi:10.1063/1.1429658.

[154] R. Ferrando, *Determining the equilibrium structures of nanoalloys by computational methods,* Journal of Nanoparticle Research **20**, 1 (2018). doi:10.1007/s11051-018-4267-6.

[155] P. M. Larsen, K. W. Jacobsen, and J. Schiøtz, *Rich Ground-State Chemical Ordering in Nanoparticles: Exact Solution of a Model for Ag-Au Clusters,* Physical Review Letters **120**, 256101 (2018). doi:10.1103/PhysRevLett.120.256101.

[156] K. Laasonen, E. Panizon, D. Bochicchio, and R. Ferrando, *Competition between Icosahedral Motifs in AgCu, AgNi, and AgCo Nanoalloys: A Combined Atomistic–DFT Study,* The Journal of Physical Chemistry C **117**, 26405 (2013). doi:10.1021/jp410379u.

[157] G. Kovács, S. M. Kozlov, and K. M. Neyman, *Versatile Optimization of Chemical Ordering in Bimetallic Nanoparticles,* The Journal of Physical Chemistry C **121**, 10803 (2017). doi:10.1021/acs.jpcc.6b11923.

[158] A. H. Larsen, J. J. Mortensen, J. Blomqvist, I. E. Castelli, R. Christensen, M. Dułak, J. Friis, M. N. Groves, B. Hammer, C. Hargus, E. D. Hermes, P. C. Jennings, P. B. Jensen, J. Kermode, J. R. Kitchin, E. L. Kolsbjerg, J. Kubal, K. Kaasbjerg, S. Lysgaard, J. B. Maronsson, T. Maxson, T. Olsen, L. Pastewka, A. Peterson, C. Rostgaard, J. Schiøtz, O. Schütt, M. Strange, K. S. Thygesen, T. Vegge, L. Vilhelmsen, M. Walter, Z. Zeng, and K. W. Jacobsen, *The atomic simulation environment–a Python library for working with atoms,* Journal of Physics: Condensed Matter **29**, 273002 (2017). doi:10.1088/1361-648X/aa680e.

[159] F. Wang and D. Landau, *Efficient, Multiple-Range Random Walk Algorithm to Calculate the Density of States,* Physical Review Letters **86**, 2050 (2001). doi:10.1103/PhysRevLett.86.2050.

[160] D. B. Laks, L. G. Ferreira, S. Froyen, and A. Zunger, *Efficient cluster expansion for substitutional systems,* Physical Review B **46**, 12587 (1992). doi:10.1103/PhysRevB.46.12587.

[161] A. Togo and I. Tanaka, *Spglib: a software library for crystal symmetry search,* 2018. https://arxiv.org/abs/1808.01590.

[162] J. D. Hunter, *Matplotlib: A 2D graphics environment,* Computing in Science & Engineering **9**, 90 (2007). doi:10.1109/MCSE.2007.55.

[163] A. Stukowski, *Visualization and analysis of atomistic simulation data with OVITO–the Open Visualization Tool,* Modelling and Simulation in Materials Science and Engineering **18**, 015012 (2009). doi:10.1088/0965-0393/18/1/015012.

[164] R. L. Olmon, B. Slovick, T. W. Johnson, D. Shelton, S.-H. Oh, G. D. Boreman, and M. B. Raschke, *Optical dielectric function of gold,* Physical Review B **86**, 235147 (2012). doi:10.1103/PhysRevB.86.235147.

[165] C. L. Foiles, *Optical constants of binary alloys*. In K.-H. Hellwege and J. L. Olsen, eds., *Landolt-Börnstein – Group III Condensed Matter 15B (Electrical Resistivity, Thermoelectrical Power and Optical Properties)* (Berlin Heidelberg: Springer, 1985). doi:10.1007/10201705_46.

[166] C. Gong and M. S. Leite, *Noble Metal Alloys for Plasmonics,* ACS Photonics **3**, 507 (2016). doi:10.1021/acsphotonics.5b00586.

[167] C. Gong, A. Kaplan, Z. A. Benson, D. R. Baker, J. P. McClure, A. R. Rocha, and M. S. Leite, *Band Structure Engineering by Alloying for Photonics,* Advanced Optical Materials **6**, 1800218 (2018). doi:10.1002/adom.201800218.

[168] T. Mueller and G. Ceder, *Effect of Particle Size on Hydrogen Release from Sodium Alanate Nanoparticles,* ACS Nano **4**, 5647 (2010). doi:10.1021/nn101224j.

[169] B. Alling, A. V. Ruban, A. Karimi, L. Hultman, and I. A. Abrikosov, *Unified cluster expansion method applied to the configurational thermodynamics of cubic $Ti_{1-x}Al_xN$,* Physical Review B **83**, 104203 (2011). doi:10.1103/PhysRevB.83.104203.

[170] T. Mueller, *Ab initio determination of structure-property relationships in alloy nanoparticles,* Physical Review B **86**, 144201 (2012). doi:10.1103/PhysRevB.86.144201.

[171] V. L. Deringer, M. A. Caro, and G. Csányi, *Machine Learning Interatomic Potentials as Emerging Tools for Materials Science,* Advanced Materials **31**, 1902765 (2019). doi:10.1002/adma.201902765.

[172] Y. Zuo, C. Chen, X. Li, Z. Deng, Y. Chen, J. Behler, G. Csányi, A. V. Shapeev, A. P. Thompson, M. A. Wood, and S. P. Ong, *Performance and Cost Assessment of Machine Learning Interatomic Potentials,* The Journal of Physical Chemistry A **124**, 731 (2020). doi:10.1021/acs.jpca.9b08723.

[173] B. C. Han, A. Van der Ven, G. Ceder, and B.-J. Hwang, *Surface segregation and ordering of alloy surfaces in the presence of adsorbates,* Physical Review B **72**, 205409 (2005). doi:10.1103/PhysRevB.72.205409.

[174] L.-L. Wang, T. L. Tan, and D. D. Johnson, *Configurational Thermodynamics of Alloyed Nanoparticles with Adsorbates,* Nano Letters **14**, 7077 (2014). doi:10.1021/nl503519m.

[175] C. Li, D. Raciti, T. Pu, L. Cao, C. He, C. Wang, and T. Mueller, *Improved Prediction of Nanoalloy Structures by the Explicit Inclusion of Adsorbates in Cluster Expansions,* The Journal of Physical Chemistry C **122**, 18040 (2018). doi:10.1021/acs.jpcc.8b03868.

[176] M. Todorović, M. U. Gutmann, J. Corander, and P. Rinke, *Bayesian inference of atomistic structure in functional materials,* npj Computational Materials **5**, 1 (2019). doi:10.1038/s41524-019-0175-2.

[177] I. Darmadi, A. Stolaś, I. Östergren, B. Berke, F. A. A. Nugroho, M. Minelli, S. Lerch, I. Tanyeli, A. Lund, O. Andersson, V. P. Zhdanov, M. Liebi, K. Moth-Poulsen, C. Müller, and C. Langhammer, *Bulk-Processed Pd Nanocube–Poly(methyl methacrylate) Nanocomposites as Plasmonic Plastics for Hydrogen Sensing,* ACS Applied Nano Materials **3**, 8438 (2020). doi:10.1021/acsanm.0c01907.

[178] I. Östergren, A. M. Pourrahimi, I. Darmadi, R. da Silva, A. Stolaś, S. Lerch, B. Berke, M. Guizar-Sicairos, M. Liebi, G. Foli, V. Palermo, M. Minelli, K. Moth-Poulsen, C. Langhammer, and C. Müller, *Highly Permeable Fluorinated Polymer Nanocomposites for Plasmonic Hydrogen Sensing,* ACS Applied Materials & Interfaces (in press). doi:10.1021/acsami.1c01968.